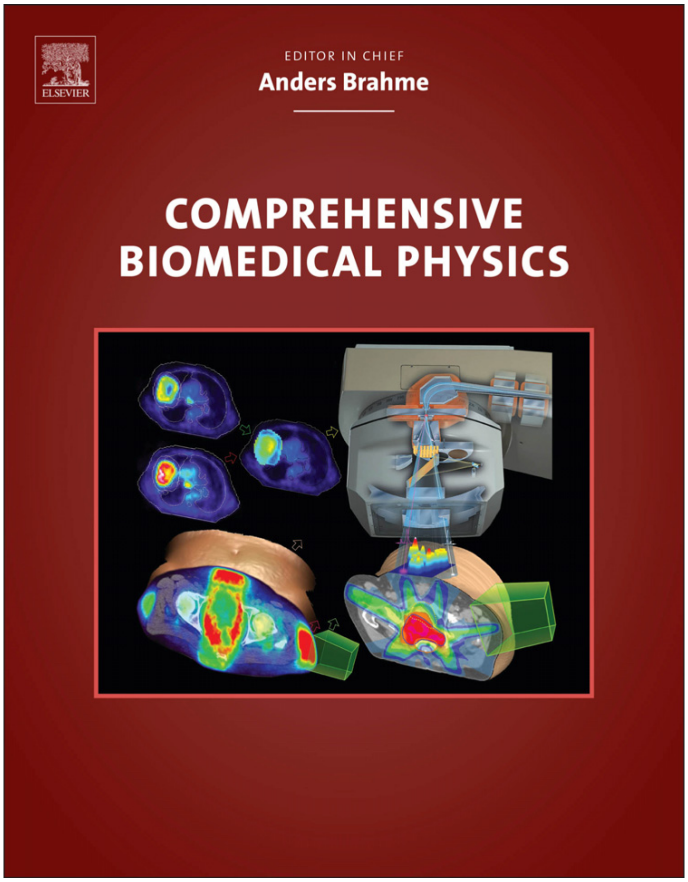

Sauli F. (2014) Gas Electron Multiplier (GEM) Detectors: Principles of Operation and Applications.
In: Brahme A. (Editor in Chief.) Comprehensive Biomedical Physics, vol. 8, pp. 367-408.
Amsterdam: Elsevier.

8.22 Gas Electron Multiplier (GEM) Detectors: Principles of Operation and Applications

F Sauli, TERA Foundation, Novara, Italy; CERN, Geneva, Switzerland

Glossary

Avalanche multiplication Increase of the signal charge produced by ionizing electron–molecule collisions in a gas at high electric fields.
Breakdown Discharge between electrodes in a gaseous counter.
CERN The European Organization for Nuclear Research, Geneva (Switzerland).
Colliders Accelerators used in high-energy physics to knock particles head-on.
Dark matter Hypothetical constituent of the universe accounting for the observed velocities of stars in galaxies.
Dual-phase Detectors in which the liquid and gaseous phases, usually of a rare gas, coexist.
Honeycomb Light structure, reminder of bees' hive, used as mechanical support in the detector construction.
LHC The large hadron collider complex at CERN.
Luminosity Intensity of the secondary particles yields from a collider.
Minimum ionizing particles (MIPs) High-energy charged particles releasing a minimum and energy-independent amount of ionization.
TERA Fondazione per Adroterapia Oncologica (Oncological Hadrontherapy Foundation), Novara (Italy).

Abbreviations

CERN	European organization for nuclear research
GEM	Gas electron multiplier
LEM	Large electron multiplier
LHC	Large hadron collider
MHSP	Micro-hole and strip plate
MIP	Minimum ionizing particle
MPGD	Micro-pattern gas detectors
MSAC	Multi-step avalanche chamber
MSGC	Micro-strip gas counter
MWPC	Multi-wire proportional chambers
RICH	Ring imaging cherenkov counter
SGEM, DGEM, TGEM	Single-, double- and triple-GEM
THGEM	Thick GEM
TPC	Time projection chamber
UV	Ultra-violet

 http://dx.doi.org/10.1016/B978-0-444-53632-7.00625-0
Comprehensive Biomedical Physics, (2014), vol. 8, pp. 367-408

8.22.1 Gaseous Detectors: Historical Background

The history of gaseous counters goes back to last century's early years, when Ernst Rutherford and Hans Geiger conceived an instrument capable to detect the tiny ionization trails released in a gas by natural radiation (Rutherford and Geiger, 1908). Consisting of a thin wire centered on a cylindrical tube, on application of a positive potential to the wire (the anode) and exploiting the avalanche multiplication process in the gas, the detector provides an amplified and detectable signal proportional to the original ionization, hence the name proportional counter. Further developments by Geiger and Walter Müller led to a device capable of detecting single electrons released in the gas; simple, reliable and cheap, Geiger–Müller counters are still widely used for radiation monitoring.

Single-wire gas counters have been used for decades, with a design and response matching the experimental needs. The concurrent study of the mechanisms of collisions between electrons and molecules under the effect of electric fields (the so-called gaseous electronics) provided a theoretical background for the understanding of the complex processes encountered within the detectors, and of their efficiency, timing, and energy resolution properties (see, e.g., Loeb, 1961).

Although examples exist of arrays of proportional counters, the use of the devices remained confined to detectors of limited geometrical coverage. In the fast expanding field of particle physics experiments, the need to instrument large detection areas with localization capability led to the development of other tools exploiting the avalanche charge multiplication in gases, such as spark and streamer chambers, where a high-voltage pulse applied between electrodes synchronously with the presence of charged tracks causes a detectable breakdown along the ionization trails. Originally recorded with optical means, the position of sparks could be sensed electronically with the development of various methods of localization, replacing the continuous electrodes with wire structures (for a survey of these technologies, see Rice-Evans, 1974).

Although very powerful at the time, detectors based on the growth of a spark have modest rate capability, due to the time needed to remove the large amount of charge generated by a spark and avoid refiring; in optimal conditions, event rates could not exceed a few per second, a rather drastic limitation for experiments.

The multiwire proportional chamber (MWPC), introduced in 1968 by Georges Charpak, revolutionized the field of fast position-sensitive detectors (Charpak et al., 1968). Continuously active, efficient at particle fluxes up to several MHz per cm^2 and with sub-mm position accuracy, the device met the most stringent experimental requirements of the time. The development of large-area MWPC manufacturing technologies, and the emerging availability of high-density electronics led soon to a new generation of detectors. Exploitation of the electrons' drift time and of the cathode-induced signals originated a variety of other devices fulfilling the needs of high-energy physics experimentation (see, e.g., Charpak and Sauli, 1984).

The commissioning of high luminosity colliders, and the quest for rare events embedded in a large flux of combinatorial background, revealed several weaknesses of detectors based on wire structures. The discrete spacing of wires implies a limited accuracy and multitrack separation; the long time taken by the ions produced in the avalanches to clear the region of multiplication results in a field-distorting space charge accumulation, with a consequent fast drop of gain at high fluxes. More seriously, a permanent damage of the structures due to the formation of solid deposits on electrodes (the so-called aging) permanently affects the detectors after long-term exposure to radiation. After decades of research on the subject, aside from a generic set of do and do not rules, a general solution to the aging problem in wire chambers has yet not been found (Capeáns, 2003).

An innovative detector named micro-strip gas counter (MSGC), introduced in 1988 (Oed, 1988), seemed to fulfill the more demanding requirements: a substantial improvement in position resolution, and an increase by several orders of magnitude of rate capability, as compared to MWPCs. Consisting of alternating anode and cathode strips engraved on an insulating support, although limited in size, MSGCs could be manufactured industrially with photolithographic processes. Several experiments were designed to make use of large arrays of MSGCs (Sauli, 1998). Disappointingly, and despite a large effort in optimizing structures and operating conditions (Bouclier et al., 1995), the devices appeared prone to fast degradation and discharges, with devastating effects on the fragile electrodes, and have been virtually discontinued.

The problems encountered with the MSGCs spawned the development of alternative structures, collectively named micro-pattern gas detectors (MPGDs), promising comparable performances but more resilient to radiation and spark damages: microgap, microwire, microdot, field gradient lattice, Compteur à Trous, and others; for an overview of these devices and related references, see Sauli and Sharma (1999). In most cases, however, the new structures appeared to be difficult to manufacture in reasonable sizes and quantities. Noticeable exceptions are the micro-mesh gaseous structure (MICROMEGAS) (Giomataris et al., 1996) and the gas electron multiplier (GEM) developed by Sauli (1997).

Already in use in many experimental setups worldwide, the new devices are still the subject of extensive development work aimed at improving performances and manufacturing methods in the framework of the RD51 international collaboration (Duarte Pinto, 2009). A review of the progress with MPGDs can be found in Titov (2007).

8.22.2 Early Observations with the GEM

Most of the problems encountered with the MPGD designs mentioned above derive from the fragile nature of the structure, thin anode strips, wires, or pins. A damaging discharge can be induced by several causes: manufacturing defects, spontaneous field emission from cathodes, and large ionizations produced by unwanted background events. Often, the outcome of a discharge is an irreversible damage to the detector or readout electronics, the more severe the larger the detector area and hence the stored energy. Various methods for reducing the energy of a discharge have been devised, with high-value protection resistors or resistive coatings on electrodes, generally, however, resulting in a spread of the signals, a degradation of the time resolution, and a reduction of rate capability. Confronted with such problems during the development of MSGC-based detectors for an experiment at CERN (Barr et al., 1998), it occurred to the author that a solution to the problem would be to separate the multiplying element, prone to sparking, from the signal collecting electrode and its delicate electronics. Such a device existed: developed several years before, the multistep avalanche chamber (MSAC; Charpak and Sauli, 1978) permitted achieving high gains and stable operation in a multiwire structure filled with a photosensitive vapor, where photon-induced feedback limits the achievable gain. The MSAC has a first region of high field between two metallic grids, where charge is preamplified and partly transferred to the main element of multiplication, a standard MWPC; the combined gain of the cascaded structures, each operated below the critical value for discharge, was large enough to detect single photoelectrons. Large-area detectors of this design were successfully used in one of the first operational Cherenkov ring imaging (RICH) devices (McCarty et al., 1986).

Knowledgeable of the surprisingly good proportional amplification properties obtained with simple holes drilled on a printed circuit board (the so-called 'Compteur à Trous' (Bartol et al., 1996)), the author had the idea to realize a microstructure where a pattern of closely spaced holes through a metal-coated insulating foil would act as a preamplification element, much as the double mesh electrodes did in the MSAC, but with a much finer structure, better matching the granularity required by the new generation of MPGDs.

The expertise acquired with flexible printed circuits manufacturing at the CERN workshop (led at the time by Angelo Gandi, and later by Rui De Oliveira) permitted to realize the first GEM electrodes, with an active area of $25 \times 25\ \mathrm{mm}^2$ on a 50-μm-thick, copper-coated polymer foil (**Figure 1**) and test them almost overnight (Sauli, 1997). Due to the manufacturing procedure, to be discussed below, the holes have a double-conical cross section, with the diameter at the metal surfaces wider than at the center of the polymer.

Computed with the widely used program GARFIELD (Veenhof, 1998), **Figure 2** shows the electric field in a cross section perpendicular to the electrode near the holes, on application of a difference of potential between the two metal sides and in presence of external fields, named respectively drift (top) and collection (bottom) (Bachmann et al., 1999). (Most field-solving programs compute the equipotential surfaces only. The lines shown in the figure are actually electron drift trajectories; their density represents the electric field only by careful adjustment.) Ionization electrons released in the upper gas gap drift into the holes and undergo avalanche charge multiplication in the high local dipole field; a fraction of the electrons on the avalanche's front transfers to the lower gap and proceeds toward a collecting electrode or a second element of multiplication. **Figure 3** is the first observation of pulse height distributions recorded exposing a combined GEM-MWPC detector to an ^{55}Fe 5.9 keV x-ray source (Sauli, 1997). The lower amplitude pulses correspond to conversions in the gas between GEM and MWPC, while the higher amplitudes are due to conversions above the GEM foil; the observed pre-amplification factor is around eight, and, as it can be seen, it preserves the energy resolution of the counter. Since part of the electrons in the avalanche is collected by the lower GEM electrode, the observed transferred charge corresponds to the effective gain, the real gain being larger by a fraction that depends on the geometry and external fields, as discussed in the next section (Sauli, 1997; Bellazzini et al., 1998).

8.22.3 GEM Manufacturing and Performance Optimization

The first GEM electrodes, and most of those produced since, have been manufactured with a photolithographic process developed at CERN by de Oliveira and collaborators (Bachmann et al., 1999). A copper-clad polyimide foil is laminated on one side with a photosensitive coating (usually named photo resist) and exposed to UV light through a mask with the desired holes' pattern; the process is repeated on the other side. After curing, the coating is chemically removed in the exposed areas, and the underlying metal etched with a standard printed circuit technology. The foil is then immersed in a polymer solvent to open the channels in the regions not protected by the metal; due to the wet-etching process, the holes in the polymer tend to have

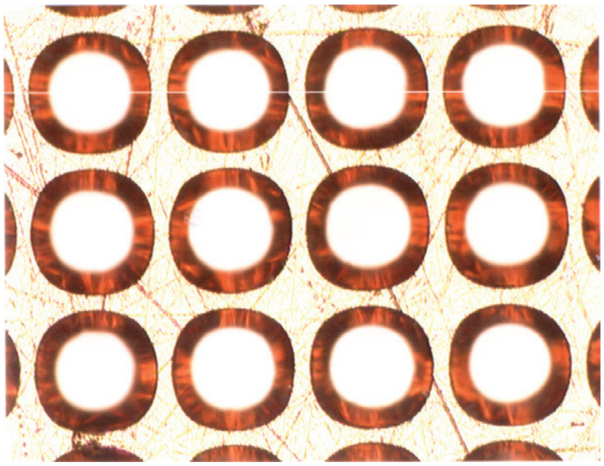

Figure 1 Close view of the first GEM foil, with holes 140 μm apart.

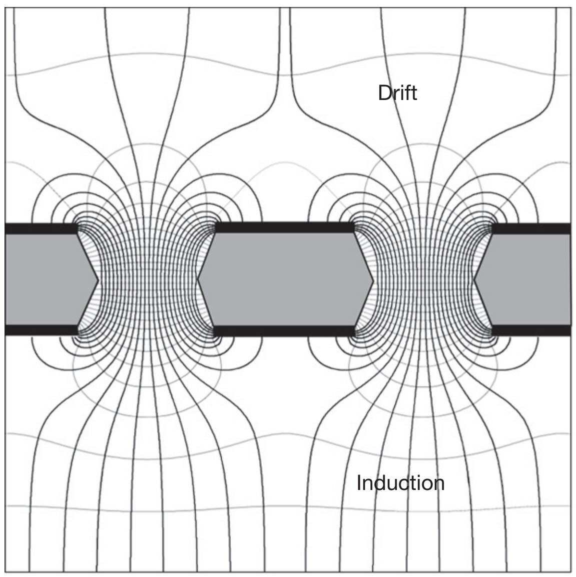

Figure 2 Field lines and equipotentials in the region of the holes of a GEM foil.

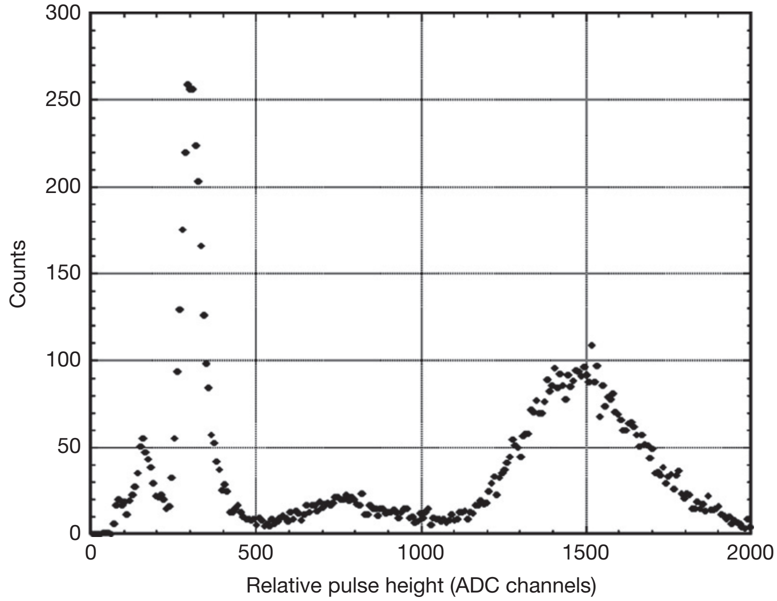

Figure 3 Pulse height spectra recorded for an ^{55}Fe x-ray source with a GEM-MWPC detector at a moderate GEM gain.

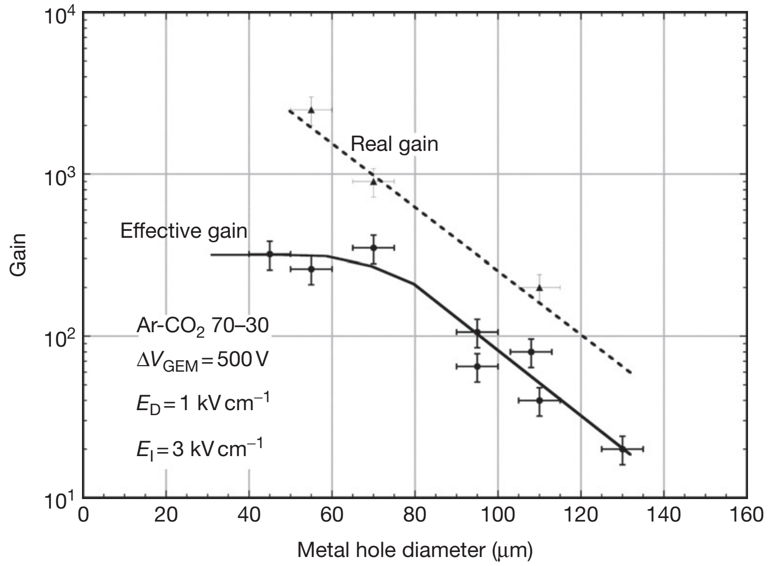

Figure 4 Real and effective gain of GEM foils as a function of metal holes diameter, at fixed operating conditions.

a double-conical shape, with the minimum diameter in the center. A more detailed description of the process can be found in Walz (2010).

For a given foil thickness and voltage difference between the electrodes, the largest avalanche gains are obtained with narrower holes; however, losses on the insulating walls reduce the transferred fraction of electrons, or effective gain, as seen in **Figure 4** (Bachmann et al., 1999). The best results are obtained with an aspect ratio (hole diameter over foil thickness) close to unity, an observation confirmed in a wide range of geometries.

To prevent gain shifts due to the insulator charging-up during operation (see **Figure 19**), the best geometry would be an almost-cylindrical hole; however, this tends to reduce the maximum operating voltage, due to the shorter path between electrodes along the insulator surface; prolonged immersion in the solvent can also cause under-etching and detachment of the metal layer. A pronounced double-conical shape permits reaching higher gains, but is prone to larger gain shifts due to charges accumulating on the insulator surface. The choice is a compromise between the two effects; in early works, preference was given to a geometry permitting to attain high gains. **Figure 5** shows an example of gain measured in argon–carbon dioxide mixtures, with a small-size foil optimized for high gains; full efficiency for minimum ionizing particles (MIPs) could be obtained with a single GEM coupled to a printed circuit for the signal readout (Benlloch et al., 1998b). Further work, to be discussed below, favors multi-GEM structures for increased reliability and immunity to discharges.

The manufacturing process relies on fine-tuning of the etching parameters to yield a foil that can be used as a

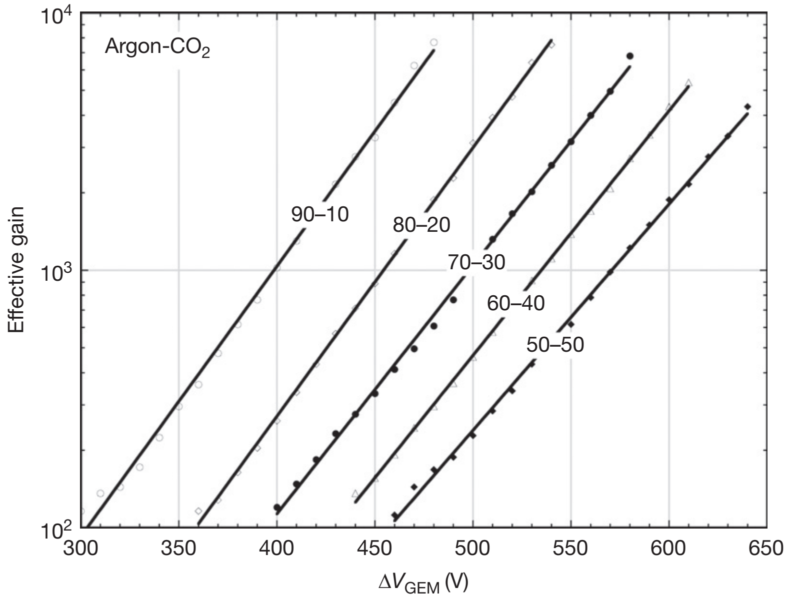

Figure 5 Effective gain measured as a function of voltage in argon–CO_2 mixtures with a GEM optimized for high gains.

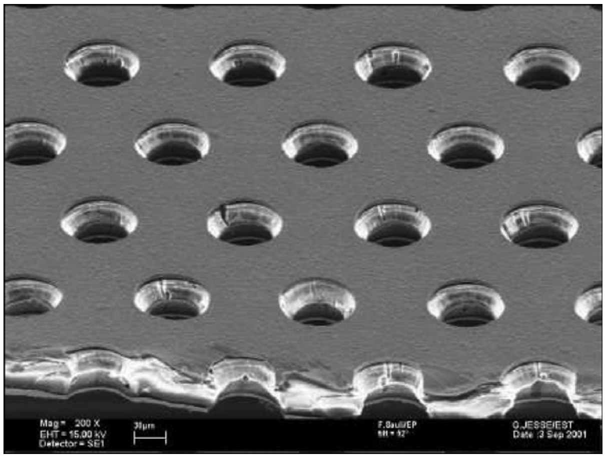

Figure 6 Electron microscope picture of a 'standard' GEM foil, with 70 μm holes at 140 μm pitch in a triangular pattern.

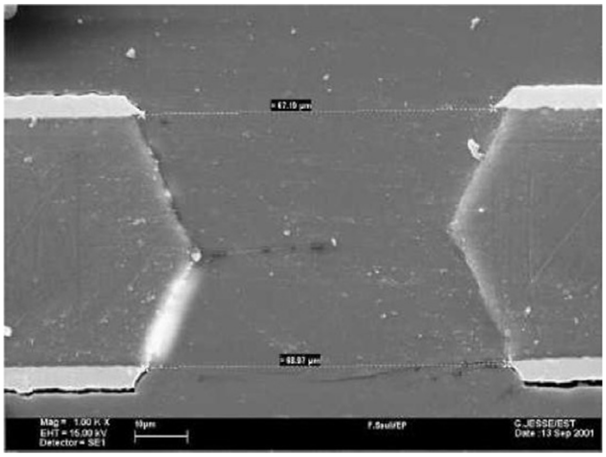

Figure 7 A section through a hole with double-conical shape. The hole diameter at the metal surface is 70 μm and the opening in the center of the polymer 50 μm.

GEM electrode. Paramount factors are the quality of the copper-coated polymer, the alignment of the masks used to imprint the holes' pattern on the two sides, and the absence of defects or contaminants. A thorough control of the polymer etching time is needed to guarantee a defect-free uniform engraving of the pattern; this is the most delicate step in manufacturing.

Figure 6 is a close view of a widely used geometry, often-referred to as 'standard GEM,' manufactured at CERN: 70 μm diameter holes at 140 μm pitch, arranged in a triangular pattern; Figure 7 is an electron microscopy image of a cross section through a hole, showing the characteristic double-conical shape with an inner diameter in the center of the polymer of 50 μm (Altunbas et al., 2002). To reduce possible sources of discharge, the sharp metal edges can be smoothed by a second etching, a process used also to diminish the thickness of the metal coating and reduce its contribution to multiple scattering for charged particles in spectrometers (Bondar et al., 2006a; Krämer et al., 2008).

Figure 8 shows a medium-size GEM foil, $10 \times 10\ cm^2$ active, produced by the CERN workshops in large quantities and a workhorse for many detector developments. In Figure 9, Gandi and de Oliveira show one of the GEM electrodes produced for the MSGC-GEM upgrade of the HERA-B forward tracker; in Figure 10, the author holds a medium-size GEM foil ($30 \times 30\ cm^2$ active). Several hundred foils of this design have been produced at CERN for the construction of the triple-GEM (TGEM) trackers used in COMPASS (Altunbas et al., 2002), the LHCb muon trigger (Bencivenni et al., 2002a), the STAR Hadron Blind (Anderson et al., 2011), and numerous other experiments.

Industrially produced electrodes were successful in delivering similar performances (Simon et al., 2009; Surrow et al., 2007).

Figure 8 A 'standard' 10×10 cm^2 unframed GEM foil, produced at CERN in large quantities (picture by the author at CERN).

Figure 10 The author holding a 30×30 cm^2 GEM electrode, with the individually powered sectors visible on one side of the foil (picture CERN).

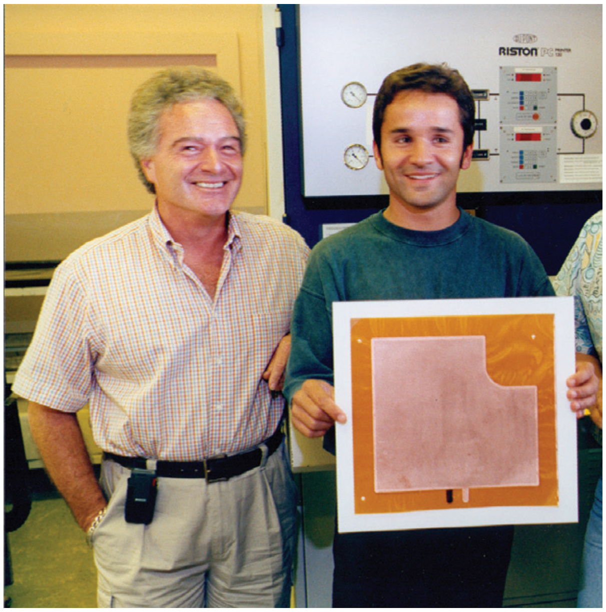

Figure 9 Angelo Gandi (left) and Rui de Oliveira with a large GEM foil produced for the MSGC-GEM HERA-B tracker (picture CERN).

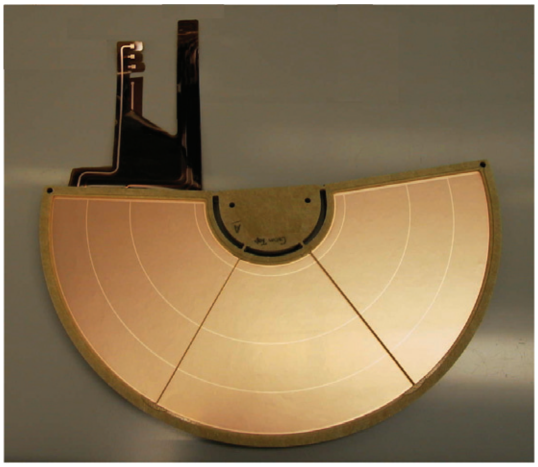

Figure 11 A framed semicircular GEM foil, 30 cm in diameter, used for the TOTEM T2 telescope (picture CERN).

A distinctive advantage of the GEM technology is that detectors can be easily built other than with rectangular geometry, better matching the experimental requirements. Figure 11 shows the half-moon foils used for the TOTEM GEM tracker at CERN, designed to allow insertion of the final detector in an existing cylindrical neutron shield with the beam tube in the center (Lami et al., 2006).

Alternative production methods making use of laser drilling and plasma etching have been developed, resulting in more stable structures with cylindrical holes (Inuzuka et al., 2004; Tamagawa et al., 2006, 2009); they are, however, limited in use and size by the high manufacturing costs.

The gain of the structure depends on the holes' diameter; a strict tolerance on this parameter is, therefore, required. Experience with the COMPASS GEM detectors' construction and operation indicate that, for the standard geometry, a 5-μm tolerance in diameter is required to achieve a maximum gain variation over the sensitive area of 30% (Altunbas et al., 2002). The control of quality and uniformity can be done with simple optical inspection, as described in the quoted reference, by mapping the scintillation light emitted by the foils with a solid-state camera (Fraga et al., 2000) or using more sophisticated computer-controlled scanning and image analysis (Kalliokoski et al., 2012; Simon et al., 2007).

With the described manufacturing process, misalignments between the two masks exceeding a few microns result in incomplete or slant holes, with ensuing local gain and stability variations. With an alternative single-mask processing, the metal holes etched on one side of the foil are used as self-mask for the polymer removal into the holes down to the second copper layer; a successive etching tuned to remove half of the metal reduces correspondingly the copper thickness, and, acting from both sides, opens narrower holes on the second layer. The resulting foils, appropriately named conical GEMs, have operating characteristics that depend on the orientation of the foil in respect to the drifting electrons: higher gains from large to

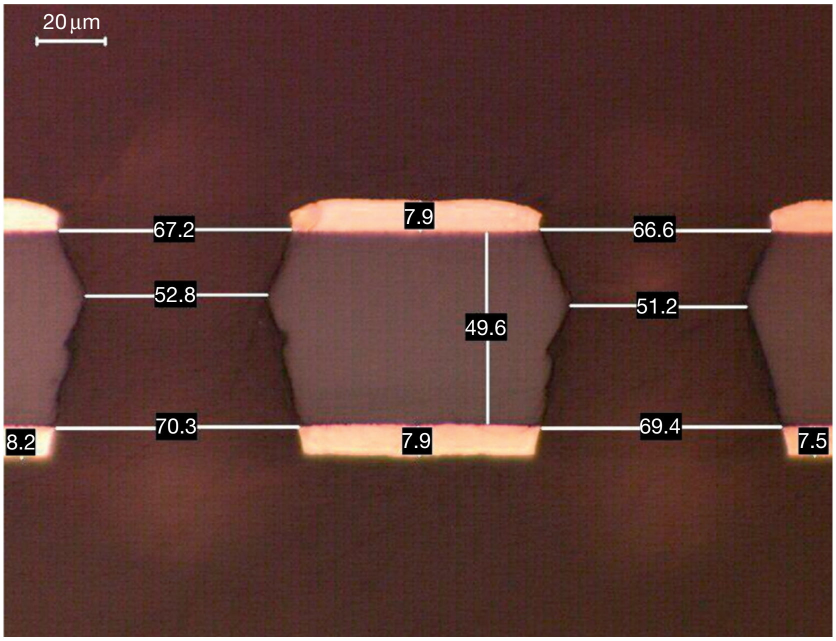

Figure 12 Cross section of an almost-cylindrical hole in a GEM manufactured with optimized single-mask process.

narrow holes and lower charging-up in the opposite direction (Bachmann et al., 1999; Bouianov et al., 2001).

The single-mask process has been successfully optimized in view of the realization of large-area detectors (Alfonsi et al., 2010; Villa et al., 2011); thorough control of the wet-etching parameters results in almost-cylindrical holes, the optimal choice for gain stability. **Figure 12**, from the previous references, is a cross-sectional view of the holes' shape obtained with this technology. To overcome the limitations imposed by the maximum width of the copper-coated polymer used for manufacturing (60 cm), a splicing technology has been developed to join together two foils with a minimum efficiency loss (Duarte Pinto et al., 2008). **Figure 13** shows a prototype TGEM, about 1 m high, under development at CERN for the CMS muon trigger upgrade (Sharma, 2012) using a single mask process.

Scaled-up versions of the multiplier, named optimized GEM (Periale et al., 2002; Ostling et al., 2003) or thick GEM (THGEM, Chechik et al., 2004), have been developed, making use of thick printed circuit boards mechanically drilled with wider holes (for a review see Breskin et al., 2009) **Figure14** shows a large-size THGEM electrode developed for the COMPASS RICH upgrade (Alexeev et al., 2008). A similar structure, named large electron multiplier (LEM), is used for the development of dual-phase detectors (Badertsher et al., 2010). Thanks to its mechanical stiffness and ease of manipulation, the THGEM is attractive for applications requiring large detection areas and gains, as for Cherenkov ring imaging (Alexeev et al., 2011; Chechik et al., 2005). Combining mechanical drilling with tuned copper etching, the distance from the metal electrode and the holes' edge (the rim) can be controlled; the picture in **Figure 15** shows an example of THGEM cross section having a 50-μm rim (Alexeev et al., 2008). The effect of the rim size in determining the maximum gain and the charging-up process will be discussed below.

Various models of GEM structures with resistive electrodes have been developed, aiming at protecting the detectors and the readout electronics from damages due to discharges (Di Mauro et al., 2007); albeit with reduced rate capability, due to the potential drop at high load currents, resistive standard or THGEMs allow one to reach high gains and appear to be suitable for detection of single photoelectrons for RICH applications (Agócs et al., 2008; Martinengo et al., 2009; Peskov et al., 2012a).

Figure 13 A large TGEM prototype, under development for the CMS muon upgrade.

Several variants to the basic GEM geometry have been introduced to reduce the positive ion backflow, a limiting factor for time projection chambers (TPCs) and visible photon detectors; Figure 16 shows some of these structures, obtained engraving on one side of the GEM foil thin additional strips with a potential optimized to efficiently collect part of the positive ions backflow before it reaches the upper part of the detector: the microhole and strip plate (MHSP; Maia et al., 2003) and the COBRA devices (Lyashenko et al., 2009; Veloso et al., 2011).

Charge collection and multiplication properties have been extensively studied as a function of GEM geometry and applied fields, both experimentally and by simulation (Bachmann et al., 1999; Barbeau et al., 2004; Bencivenni et al., 2002b; Bonivento et al., 2002; Bouianov et al., 2000; Guedes et al., 2002; Richter et al., 2000, 2002; Sharma, 2000; Tikhonov and Veenhof, 2002). Figures 17 and 18 are examples of measurements from the first reference. A simple structure consisting of a GEM foil between two electrodes is exposed to a soft x-ray flux, and currents on all electrodes are measured as a function of the applied potentials (see the inset in Figure 17 for definitions). At low values of the drift field ionization, electrons are partly lost on the upper GEM electrode; full drift into the holes is reached at higher fields, and the region of transparency is wider the higher the GEM voltage. As seen in Figure 18, the currents on the drift and upper GEM electrodes, due to ions, are positive, while they are negative on the others. With the increase of the induction field, the fraction of electrons reaching the lower electrode increases, at the expense of the charge collected by the bottom GEM; the ion currents on the top GEM and drift electrodes remain almost constant.

Figure 14 A large thick-GEM electrode developed by INFN-Trieste for the COMPASS RICH upgrade.

The fraction of ions receding to the drift electrode, often referred to as ion feedback or backflow, is in this case close to 50%. Without consequences for thin-gap tracking devices, a high fractional ion feedback can be a problem for other applications, and various methods have been devised to reduce it to a few percent or less when using GEMs for TPC or photon detection (Breskin et al., 2002b; Sauli et al., 2006). This topic is covered in detail in Section 8.22.7.3.

At fields above 15 kV cm^{-1}, parallel-plate charge amplification starts in the induction gap; although in principle exploitable to obtain higher gains, operation in this mode favors the propagation of discharges through the structure, and should be avoided.

As observed in the early works, during avalanche multiplication charges deposit on the insulator and dynamically modify the gain, an effect that appears to be more relevant for narrower hole (Bouclier et al., 1997). In general, the gain

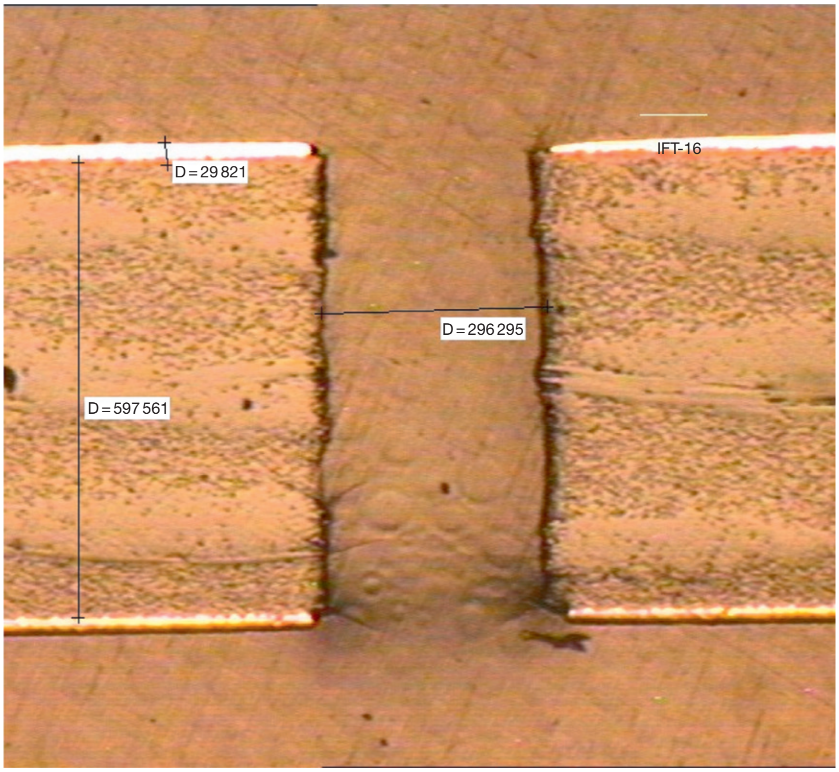

Figure 15 Cross-sectional view of a Thick GEM; a retreat of the metal (the rim) is clearly visible in this sample.

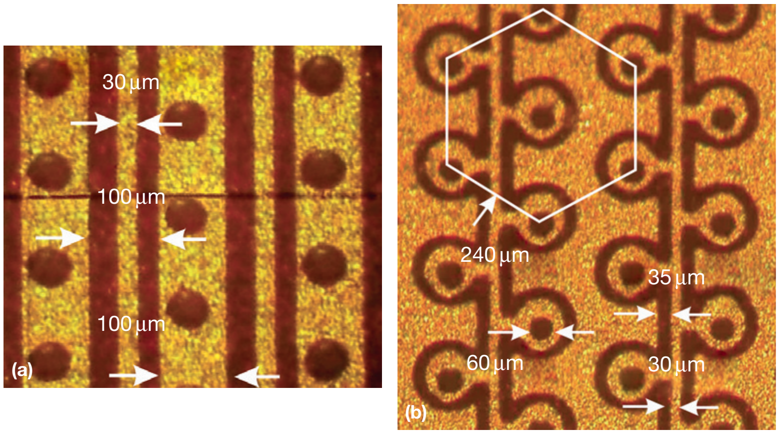

Figure 16 Patterning of a GEM electrode, aimed at reducing the positive-ion feedback: the microhole and strip plate (MHSP) (a) and the COBRA pattern (b).

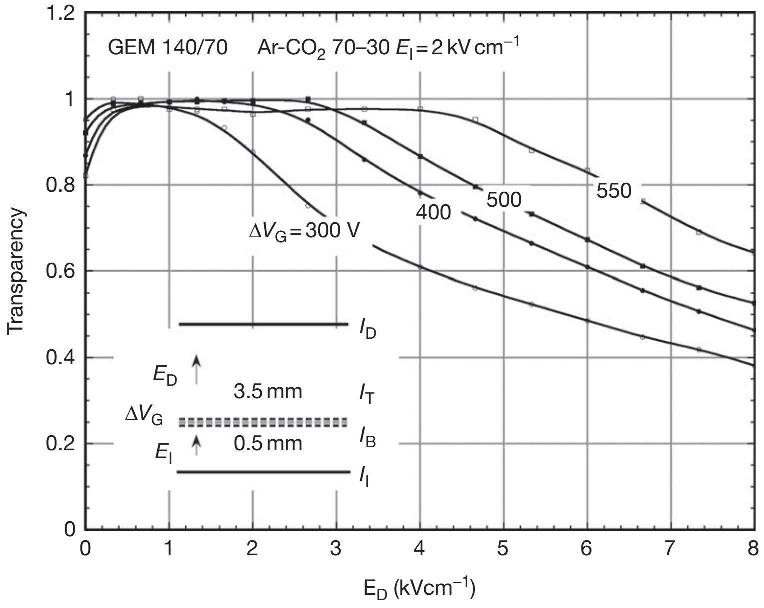

Figure 17 Normalized electron collection efficiency as a function of the drift field for several values of the GEM multiplying potential, at constant induction field.

increases with time and exposure to radiation, an observation that can qualitatively be understood due to the increase of the electric field in the hole induced by accumulating charges on the walls, opposing additional depositions on the surface. Figure 19 provides examples of time-dependent gain modification under irradiation of three GEM geometries: conical with the electrons entering from the large hole side, standard biconical, and cylindrical (Benlloch et al., 1998b). The legends indicate the geometrical parameters: pitch/upper/lower hole diameter for the conical and cylindrical and pitch/hole/central hole diameter for the double conical.

As mentioned, while the best choice would be a cylindrical shape, this is difficult to obtain with the standard wet-etching method, and may result in a decrease in electrical rigidity; most of the operational detectors have been realized so far with standard biconical GEMs, despite the inconvenience of an initial moderate gain shift (typically below 30%).

The addition of a small percentage of water in the gas mixture almost completely eliminates the charging-up process, presumably making the polymer surface slightly conductive (Bouclier et al., 1997). Further observations indicated, however, that the discharge probability on heavily ionizing tracks is seriously increased for a water content exceeding a few tens of ppm, ruling out this simple solution to the gain shift problem (Altunbas et al., 2002). The sensitivity to moisture can, however, explain discrepancies in the gain and charging-up performances of apparently identical detectors. Some attempts have also been made to reduce the foil resistivity with carbon coating (Beirle et al., 1999); although promising, they seem not to have been pursued.

For not well-understood reasons, GEM foils industrially produced with equivalent materials and technology often exhibit a larger gain increase at start-up (Surrow et al., 2007). Acceptable for tracking devices, this is a nuisance in the use of the detectors as proportional counters.

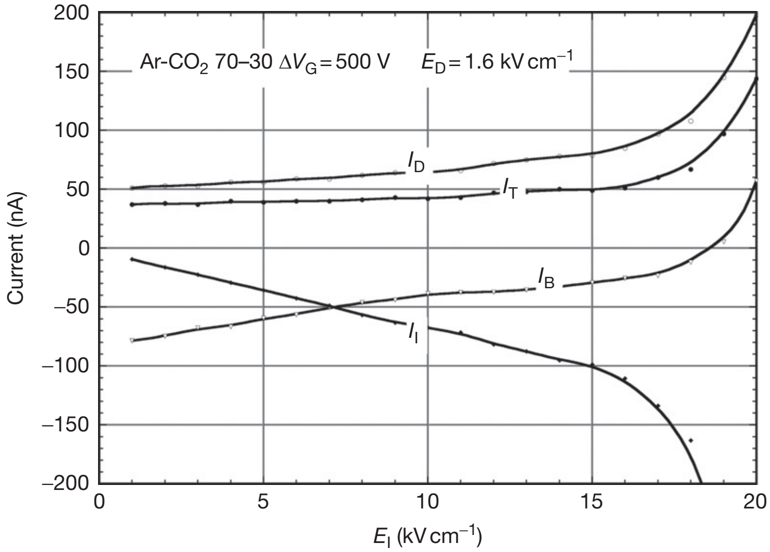

Figure 18 Currents on all electrodes of a single-GEM detector irradiated with a constant x-ray flux, as a function of the induction field. GEM and drift voltages are constant.

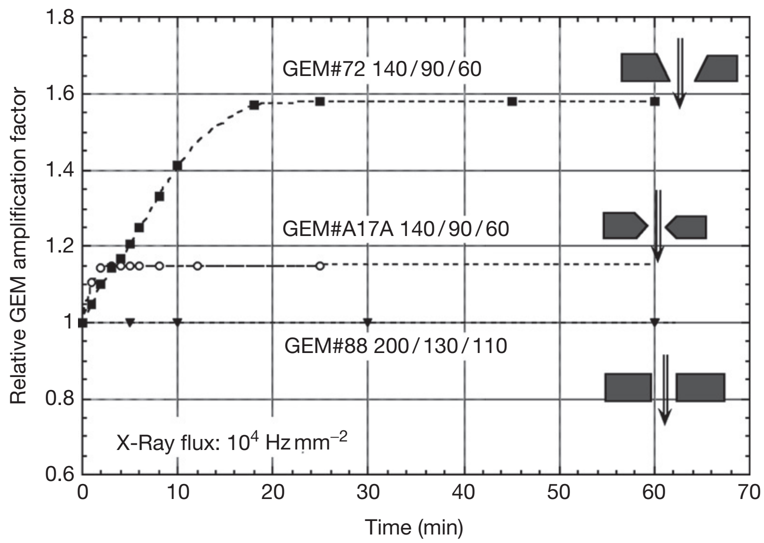

Figure 19 Initial gain increase after power on, under irradiation, of three GEM models: conical, standard double-conical and almost-cylindrical.

As mentioned, the longer discharge path between the metal electrodes obtained with a pronounced double-conical shape allows reaching higher gains, at the expense of an increased initial gain modification due to charging-up of the insulators. This has been confirmed by recent observations with THGEM electrodes; while mechanically drilled holes are cylindrical, the metal around their edges can be partly removed by chemical etching. A large value of the rim (the width of the circular metal-free region at the surface) allows reaching high gains but results in a considerable gain shift at power on, as seen in Figure 20 (Alexeev et al., 2010a). The width of the rim affects also the drift field dependence of the energy resolution, worsening for wide rims (Alexeev et al., 2011). The choice of geometry then depends on the user, requiring a more thorough control of operating conditions to exploit the higher gain devices.

The charging-up process has been extensively studied within the RD51 collaboration with the help of electric field solvers and avalanche simulation programs. Starting with a calculation of the static electric field, the simulation generates avalanches and dynamically follows the field modifications induced by ions and electrons collected on the dielectric surfaces (Alfonsi et al., 2012). Figure 21 shows, for example, the computed fraction of electrons collected on the different parts of a GEM foil as a function of time; a comparison of the electron drift lines computed before and after charging-up of the polymer surfaces clearly shows an increase of the field with time in the center of the holes.

8.22.4 Multi-GEM Structures

The GEM foils were originally developed to solve discharge problems met with MSGCs, and have been indeed successfully added to existing detectors for this purpose (Bagaturia et al., 2002; Zeuner, 2000). It was soon realized, however, that they could

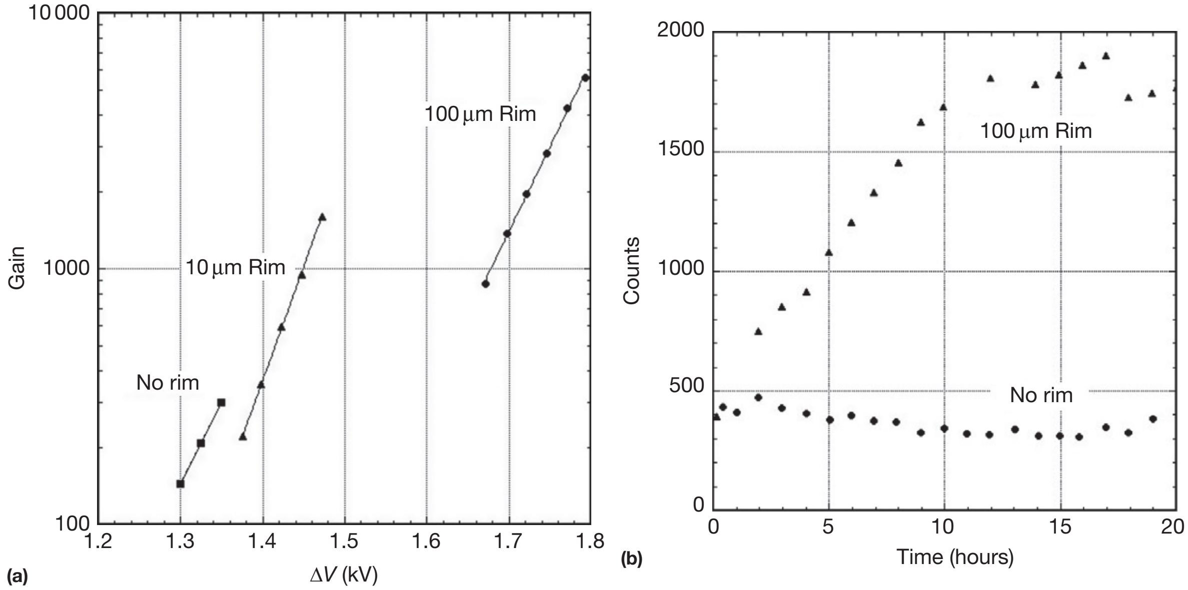

Figure 20 Gain versus voltage (a) and gain shift (b) as a function of time measured in TGEM detectors with different rims.

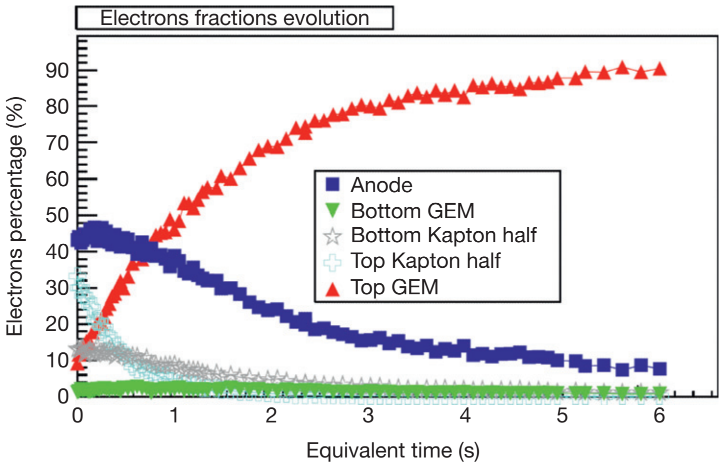

Figure 21 Computed time evolution of the fraction of electrons in the avalanches collected by different layers in a GEM structure.

attain gains sufficiently high to allow direct detection of radiation on simple collecting electrodes (Büttner et al., 1998); this requires, however, to power the devices at voltages close to the breakdown point, needing stringent quality requirements in manufacturing. Cascading two GEMs relaxes the mechanical requirements and reliably provides proportional gains well above 10^4 ensuring wide efficiency plateaux for MIP, as demonstrated in extensive beam tests with double devices (Bressan et al., 1999a).

Further work indicated that a TGEM structure was even better suited to guarantee the reliability and breakdown control needed in large experimental setups (Ketzer et al., 2004; Ziegler et al., 2000), particularly in the presence of heavily ionizing particles background, and has been adopted for many experiments operating in harsh conditions.

Figure 22 shows schematically a TGEM detector, with the resistor divider chain used to apply the appropriate voltage to each electrode; systems of stacked floating power supplies have also been developed, giving more flexibility in the adjustment of individual potentials (Corradi et al., 2007). Electrons released by ionization in the drift gap move into the first GEM and experience a first step of avalanche multiplication; a fraction of the amplified charge transfers to the second foil, and the process repeats. At each step, the effective charge gain is a convolution of the collection efficiency and the electrons transfer fraction, both functions of the applied fields; extensive measurements and simulations have been performed in order to understand the charge collection processes and optimize performances (Bondar et al., 2003; Tikhonov and Veenhof, 2002).

The overall gain of a multiple structure is the product of the effective gains of the components; in a TGEM device, the gain needed is attained with each foil operated at a voltage well below its natural discharge point, leaving a considerable margin to tolerances in manufacture and presence of local defects. At the highest gains, single photoelectron detection can be achieved, opening the way to the development of fast RICH devices (Meinschad et al., 2004).

At the gains needed to obtain full efficiency for detection of few tens of electron–ion pairs released in gaseous counters, larger energy loss events occasionally induced by neutron conversions, nuclear fragments, or electromagnetic showers can result in exceeding the so-called Raether discharge limit ($\sim 10^7$ ion–electron pairs in the avalanche). Thorough investigations demonstrate the superior performance of multi-GEM devices in reducing, and virtually eliminating discharge problems (Alfonsi et al., 2004; Bachmann et al., 2002; Bagaturia et al., 2002).

In a laboratory setup, a test detector is exposed to a low-rate soft x-ray source (5.9 keV from ^{55}Fe) to determine the proportional amplification factor as a function of GEM voltage. The detector is then exposed to a heavily ionizing source, in the form of ~ 5 MeV alpha particles from the decay of a gaseous radioactive isotope, ^{220}Rn, produced by a natural thorium oxide cartridge in the gas flow, and releasing on average 500 keV ($\sim 10^4$ electron–ion pairs) in the 3-mm drift gap. The discharge rate is measured as a function of voltage and compared with the gain curves for various structures and gas fillings. The results of measurements are summarized in Figure 23 for argon–CO_2 70–30; the horizontal scale is the voltage applied to each GEM foil (Ketzer et al., 2002). For the single GEM, the discharge probability increases exponentially approaching the Raether limit at a gain of 10^3; for multiple structures, increasingly large gains are reached at lower voltages, and discharges induced by the α tracks set in at values of gain comfortably higher than those needed for efficient detection of minimum ionizing tracks ($\sim 10^4$). An asymmetry in the potentials applied to the GEM electrodes, with the first imparting a larger gain, reduces the discharge probability even further (Figure 24; Altunbas et al., 2002).

The apparent violation of the Rather limit in multi-GEM structures is probably due to the increase in the avalanche space extension because of diffusion in the transfer gaps

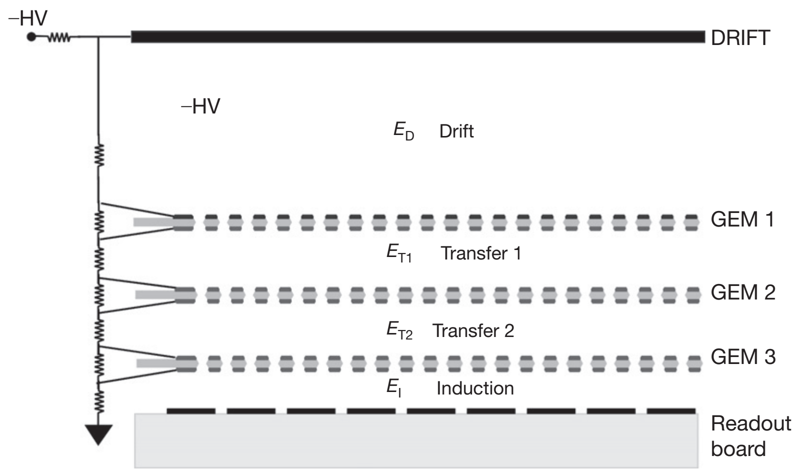

Figure 22 Schematics of a triple-GEM detector with the resistor chain used to distribute the potentials to the electrodes form a common HV power supply.

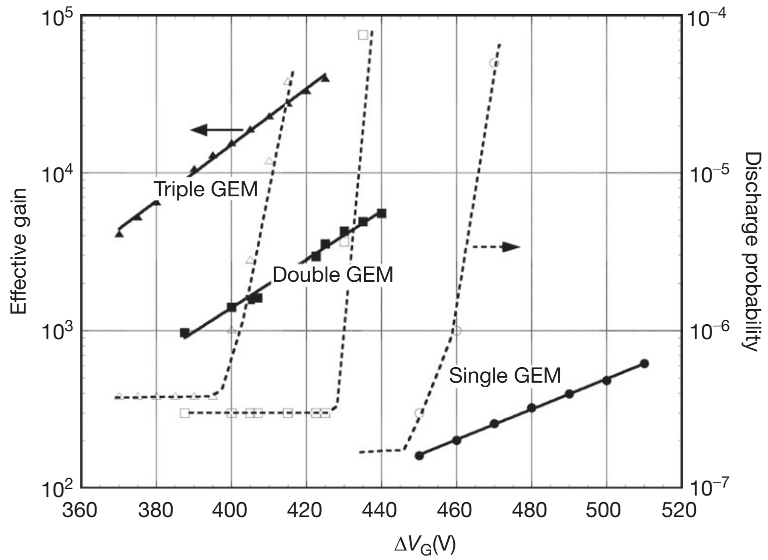

Figure 23 Effective gain (full lines) and discharge probability on alpha particles (dashed lines) of single-, double-, and triple-GEM detectors.

between multiplying foils, and the consequent spread of the charge into several independently multiplying holes.

Problem-free operation in hostile environments has been demonstrated with exposures to high-intensity hadron beams (Bachmann et al., 2001) and confirmed by long-term use in experiments. Similar results have been obtained, both experimentally and with numerical simulations, in combined micromegas-GEM detectors (Procureur et al., 2011).

GEM detectors have been operated with a variety of gas fillings. As for other gaseous counters, the choice is dictated by often conflicting requirements. Examples of gains measured with a TGEM device in several mixtures as a function of voltage applied to each multiplier are given in **Figure 25** (Breskin et al., 2002a) and **Figure 26** (Kobayashi et al., 2011). High gains can be reached in pure carbon tetrafluoride, albeit at very high operating voltages. The upper gain limit is determined by the onset of discharges, and may be dominated by the production quality and the presence of a single defect over the whole area.

As most of the multiplication occurs within the holes, in a process appropriately named avalanche confinement, high gains are obtained also in pure noble gases, where the copious emission of photons in the avalanches induces gain-limiting secondary processes in conventional counters (Buzulutskov

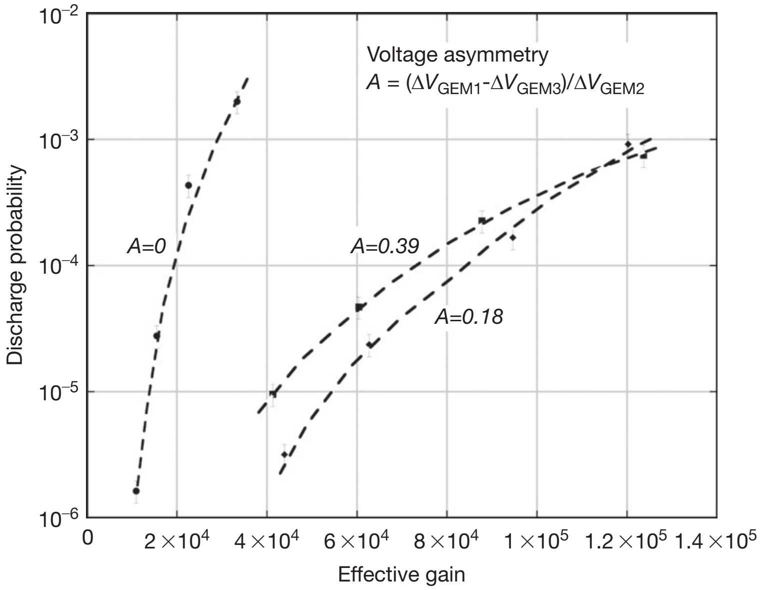

Figure 24 α-Particle-induced discharge probability as a function of effective gain for symmetric ($A=0$) and two asymmetric voltage choices to the first and last electrodes in a triple-GEM chamber.

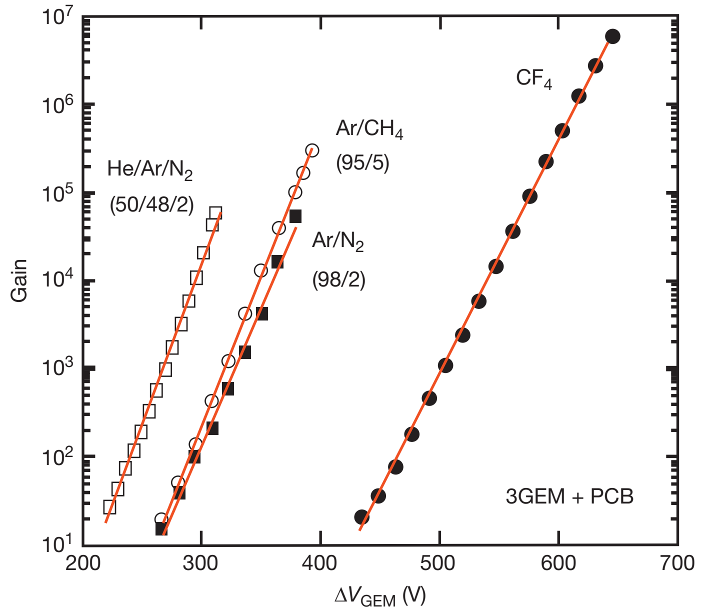

Figure 25 Gain as a function of voltage measured with a TGEM in several gas mixtures.

et al., 1999). **Figure 27** is a compilation of measurements in various mixtures with noble gases (Buzulutskov et al., 2000).

Although in most applications the detectors are at atmospheric pressure, low-pressure operation has been demonstrated (Bondar et al., 1998); gains of several thousand could be reached with a single GEM in methane and isobutane at pressures between 10 and 40 torr (Chechik et al., 1998).

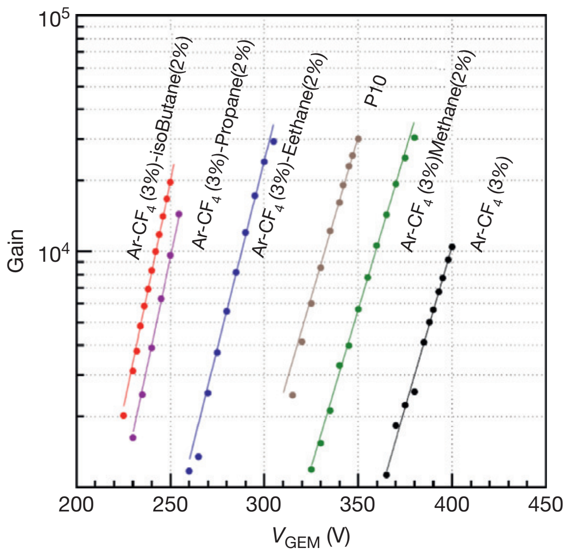

Figure 26 TGEM gain as a function of voltage in CF_4-containing mixtures.

The operation at high pressures has also been extensively studied, particularly with xenon-based mixtures, in view of applications for the detection of high-energy photons or neutrons (Amaro et al., 2004; Bondar et al., 2002a; Li et al., 2001; Orthen et al., 2003; van Vuure et al., 2001). For pure noble gases, the maximum gain decreases considerably with the increase of pressure, except for neon and helium (**Figure 28**) (Bondar et al., 2002b); a similar trend is observed also in xenon mixtures, as shown in **Figure 29** (Orthen et al., 2003); the reasons for such behavior are not well understood.

8.22.5 Signal Formation and Detection

A unique feature of GEM devices is that the signals detected in the last electrode are solely induced by the motion and collection of electrons: due to the screening effect of the foils and the avalanche confinement in the holes, the positive ion signal, the so-called ion tail present in most gaseous counters, is not observed. Signals are, therefore, intrinsically very fast and permit the resolution of tracks closely spaced in time, as shown by the examples in **Figure 30** (Ziegler, 2002).

The time evolution of the signals on closely spaced strips on the anode clearly shows the difference between charge induction and collection. From the same reference, **Figure 31** (left) shows the signals detected on four strips, 500 μm apart, on a ^{55}Fe x-ray event centered on strip 3; the signal induced on strip 1, negative during the drift of electrons toward the anode, changes sign when the charge is collected by the central strips, resulting in a zero total charge as seen from the integrated charge (right).

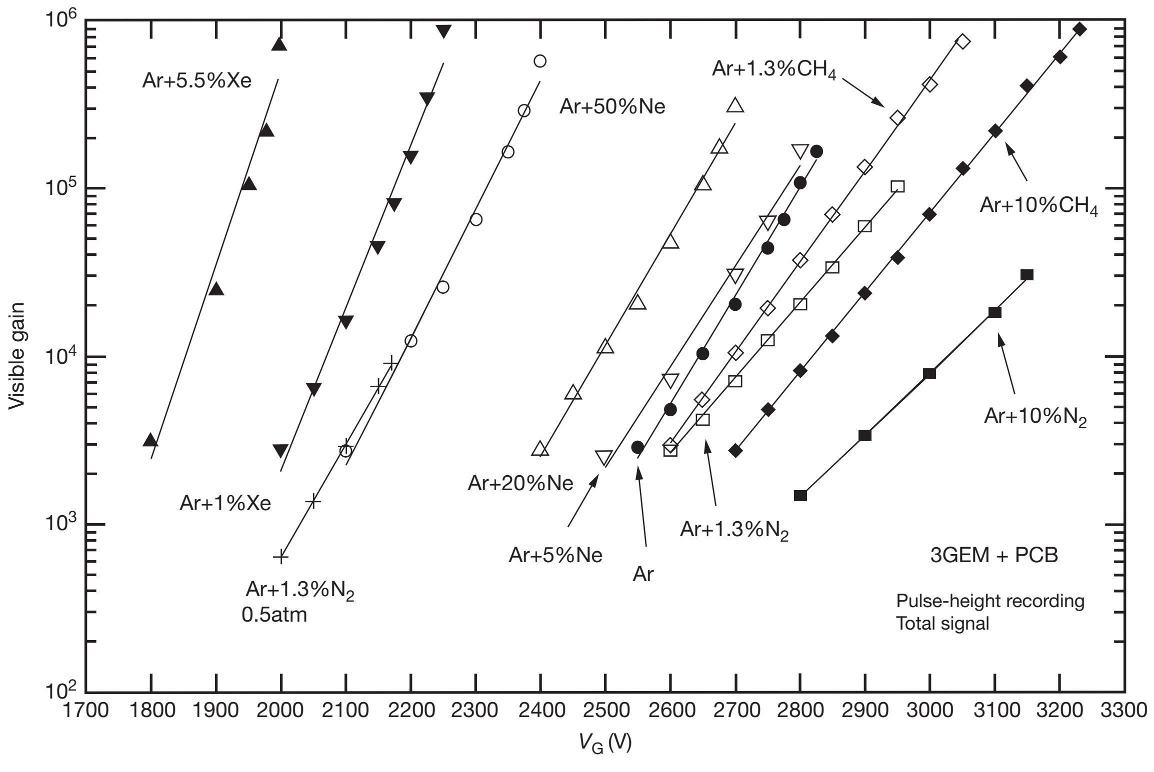

Figure 27 Triple GEM gain measured in mixtures of noble gases at atmospheric pressure.

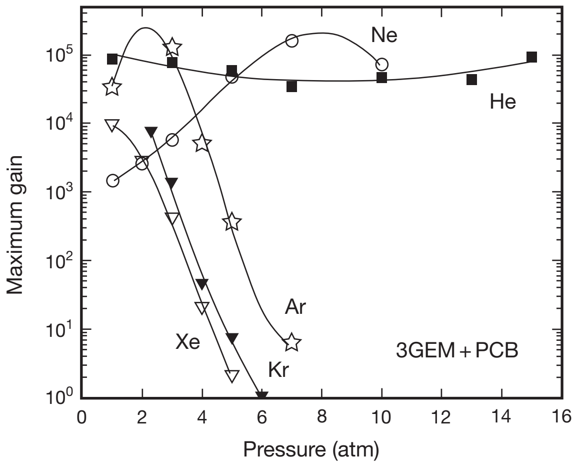

Figure 28 Maximum gain of a triple-GEM detector with noble gas fillings as a function of pressure.

The width of the charge cloud collected on the anode for localized ionization events, or cluster size, depends on the detector geometry, gas filling, fields in the transfer regions, and time constants of the amplifiers. When using front-end amplifiers with time constants around 50 ns, as is the case for most detectors, only signals with negative total charge are detected (**Figure 32**; Bressan et al., 1999a); the charge cluster, recorded with a single GEM for a 5.9-keV x-ray event on 200 μm pitch strips, has a FWHM of 400 μm.

For multiple structures, diffusion in the transfer gaps increases the charge cloud size; as indicated in the previous chapter, this plays a fundamental role in the reduction of the discharge probability. When exploiting the charge sharing between strips, it allows also achieving high localization accuracies with wider strips. **Figure 33** gives an example of cluster size distribution measured with a TGEM detector for fast charged particles perpendicular to the chamber; FWHM and width over threshold of the clusters are given,

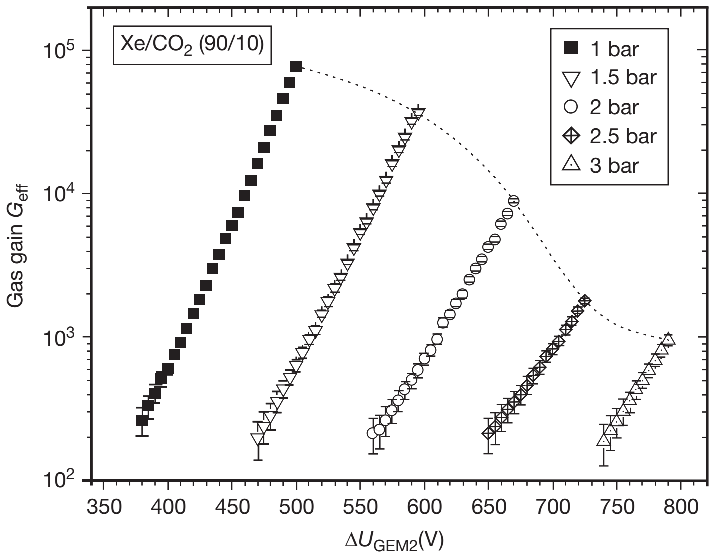

Figure 29 Gain measured with a TGEM in Xe–CO_2 at increasing pressures.

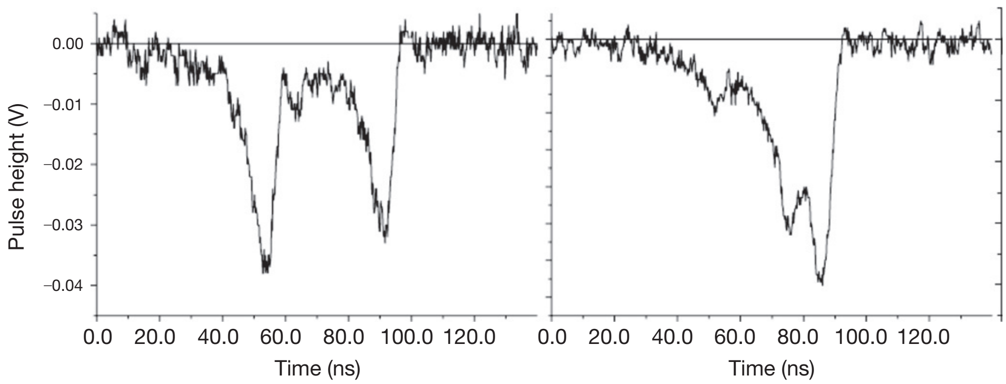

Figure 30 Fast electron signals detected on the anode of a multi-GEM; two tracks at 40 ns are well resolved (left), and still recognizable when only 10 ns apart (right).

the last quantity depending, of course, on the threshold value (∼10% of the most probable pulse height for this case) (Altunbas et al., 2002). For this geometry, a choice of 400 μm for the strip pitch is close to the optimum, as for most events the detected charge is shared between two or more strips permitting localization through the calculation of the center of gravity of the signals.

The choice of the signal readout pattern is dictated by the experimental requirements and availability of high-density electronics. A simple printed circuit board with parallel lines provides one-dimensional (1D) projections; 2D localization is obtained with two sets of parallel strips at an angle. More complicated patterns can be realized with interconnected pads, as for example the so-called hexaboard providing three projections at 120° and used to resolve ambiguities in multiple events (Bressan et al., 1999b).

A 2D readout board is realized, etching the strip patterns on both sides of a thin copper-clad polymer foil, of the type used for GEM manufacturing. The foil is glued on a thin support board, and the polymer in the space between the upper layer strips is removed by immersion in a solvent; the collected electron charge is then shared between the two projections and recorded. A close-up view of the 2D readout board used for the COMPASS TGEM detectors is shown in **Figure 34** (Altunbas et al., 2002); due to the screening effect of the first layer, with a strip pitch of 400 μm equal charge sharing between the two projections is obtained with the top and bottom strips 80 and 350 μm wide, respectively.

More complicated patterns can be realized using a multilayer technology, with suitably shaped collecting electrodes connected to readout lines routing the signals on the edges of the detectors; the semicircular TOTEM TGEM chambers have one coordinate provided by circular concentric strips and the second by radial pad rows (Bagliesi et al., 2010).

To cope with the high beam intensity in the central region of the detector, the COMPASS tracker group has developed an upgraded detector with a readout board having a matrix of 32×32, 1 mm^2 pixels individually readout, the remaining

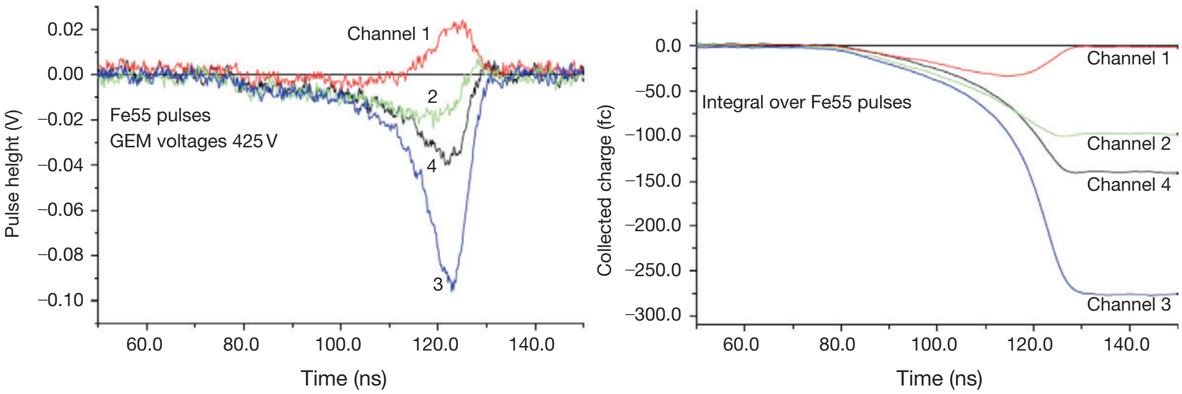

Figure 31 Fast signals detected on four adjacent strips, 500 μm apart (left) and their integral over time (right).

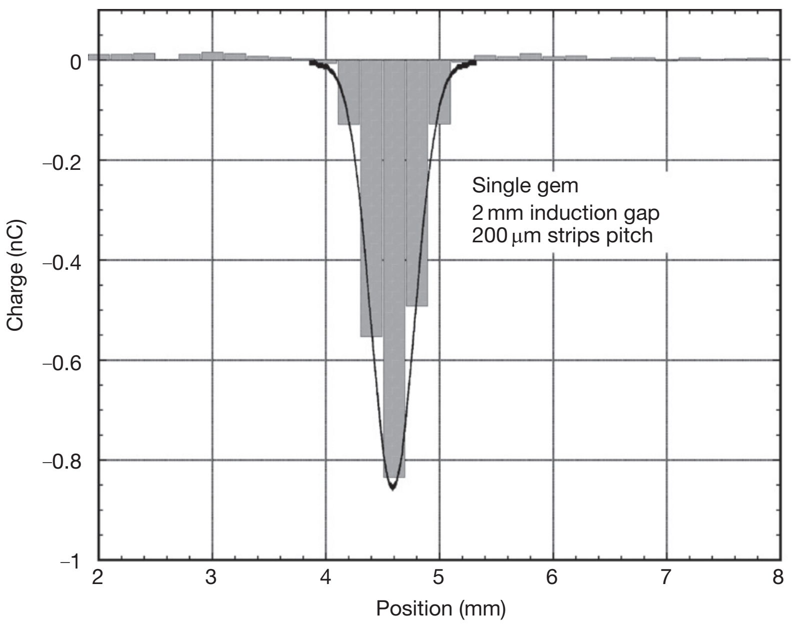

Figure 32 Cluster charge distribution for a 5.9-keV event recorded on a single GEM with readout strips 200 μm apart; it has an FWHM of 400 μm.

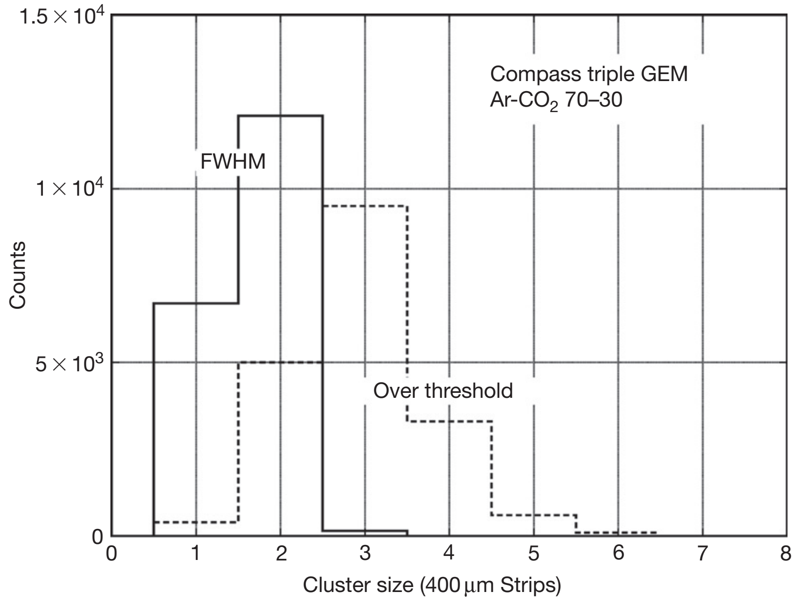

Figure 33 Cluster size distribution (FWHM and over threshold) for fast particles perpendicular to a triple-GEM detector.

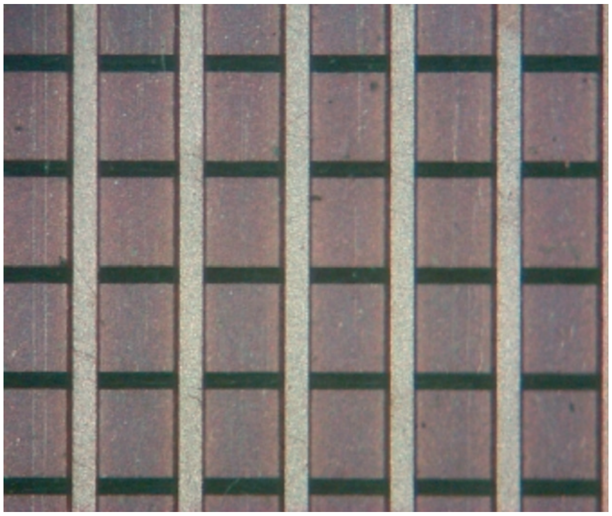

Figure 34 The 400-μm pitch 2D readout pattern used for the COMPASS chambers. The width of the strips is adjusted for equal charge sharing between the coordinates.

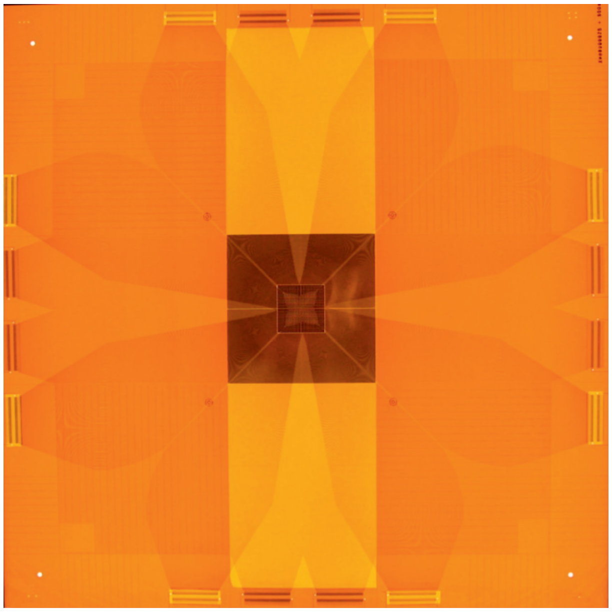

Figure 35 The readout board of the COMPASS upgrade GEM chambers. The central region has a matrix of 32×32, 1 mm^2 pixels, individually readout; the remaining area is covered by projective X- and Y- strips at 400 μm pitch.

area being covered by conventional perpendicular projective strips (Figure 35; Krämer et al., 2008).

8.22.6 GEM Chambers Construction

A variety of mechanical assemblies for GEM detector structures have been developed, suited to the experimental requirements; only few examples will be given here.

A general-purpose system, appropriately named 'GEM-in-the-box' developed at CERN by the Detectors Development Group (GDD), exploits parts used for previous work with microstrip chambers. A printed circuit board with the readout pattern, usually perpendicular projective strips, is glued to a fiberglass frame having the gas inlet and outlet; the PCB has also several solder pads to make the high-voltage connections to the internal structure (Figure 36; Bressan et al., 1999a). One or more GEM foils, of the standard design shown in Figure 8, are stretched and glued to thin insulating frames, that can be assembled in the box on insulating pillars fixed on the four corner holes visible in the figure; when needed, spacers are inserted between the frames to provide the desired gaps. A drift electrode, usually made with a framed, thin metal-coated polymer foil completes the detector. HV connections to the various electrodes are made with insulated wires soldered between the GEM lids and the pads on the base PCB. A framed thin window, bolted to the main box and with rubber joints, ensures the gas tightness. Needless to say, all the construction has to be done in controlled clean room conditions.

While for small-size detectors the GEM electrodes are monolithic, larger areas have to be sectored in order to reduce the stored energy in the case of a discharge; systematic studies have indicated in $\sim 100\ \mathrm{cm}^2$ the safe limit to avoid permanent damages. Larger foils are divided in sectors on one side, with individual high-value protection resistors connecting to the high voltage; in the case of discharge in one sector, the potential of the lower electrode, facing another GEM, is only slightly increased, preventing propagation of the discharge through the whole structure.

The described assembly has the advantage to be flexible in the choice of components and permits the replacements of damaged parts; it is, however, rather expensive and bulky, and has been mostly used for laboratory developments or beam measurements. As an alternative, an all-glued light assembly has been developed for the COMPASS GEM tracker (Altunbas et al., 2002); used to build the chambers used in the spectrometer, it has been adopted for the GEM-based detectors in other experimental setups, namely TOTEM (Bagliesi et al., 2010) and LHCb (Alfonsi et al., 2004; Bencivenni et al., 2002c).

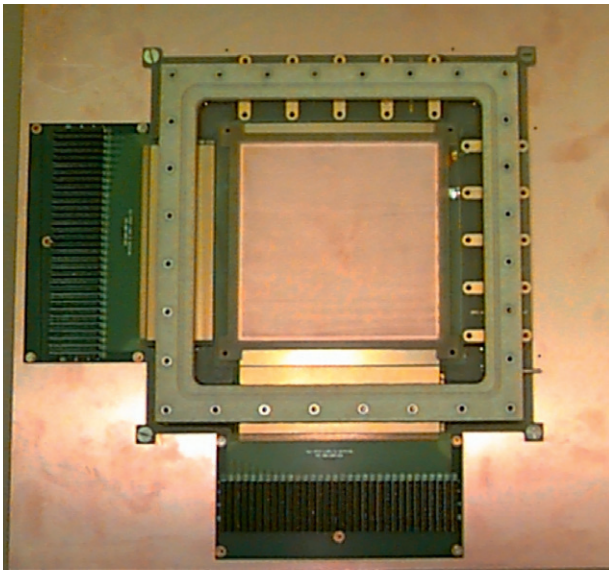

Figure 36 The general-purpose GEM-in-the-box assembly.

In the COMPASS chambers, a circular sector in the central region can be down-powered to inhibit the local sensitivity (the so-called beam killer). While the same function could be obtained with a simpler mechanical obstruction, the possibility to restore efficiency by an external control allows alignment runs on low-intensity beams. As mentioned before, the chambers have an active area of $30 \times 30\ \mathrm{cm}^2$, 2D projective readout with strips at 400 μm pitch; the drift gap of 3 mm is a compromise between time resolution and ionization losses for fast particles, and the 2-mm transfer and induction gaps provide a moderate spread of the multiplying charge while relaxing the mechanical tolerance requirements that would be needed for less dispersive thinner gaps.

The assembly makes use of light honeycomb or expanded polyurethane plates as supports of the active structures, framed and glued in sequence on the base plate; **Figure 37** shows schematically the detector structure. The GEM foils are sequentially stretched and glued to thin spacer frames (**Figure 38**); machined in the 2-mm-thick high-quality fiberglass, they have thin ribs to ensure the gap value over the area, thus relaxing the requirements on the mechanical tension on the GEM foil and compensate the electrostatic forces (metal–polymer composites, GEM foils have rather poor elasticity); the circular spacer corresponding to the voltage-controlled beam killer sector is visible in the center (Altunbas et al., 2002).

The chamber construction begins pasting the drift electrode to the top honeycomb plate; then, a 3-mm fiberglass frame defining the drift gap is glued to the plate. The first GEM foil is stretched and glued to the composite; a spacer frame is then added, and the assembly proceeds, in clean room conditions, sequentially gluing the various electrodes. As last step, the larger honeycomb plate holding the readout circuit completes the detector; gas inlet and outlet are provided through miniature tubes on the frame edges.

Essential during the construction is a verification of the HV insulation of the various electrodes: at each step, the structure is tested in a special gas box that permits a connection to the various electrodes (**Figure 39**). After completing the mechanical construction, the high-voltage distribution and readout electronics are added.

More than 20 TGEM chambers having an active area of $30 \times 30\ \mathrm{cm}^2$ with 2D projective readout have been produced and successfully operated for many years (Abbon et al., 2007); **Figure 40** shows Leszek Ropelewski with the first prototype of the detector.

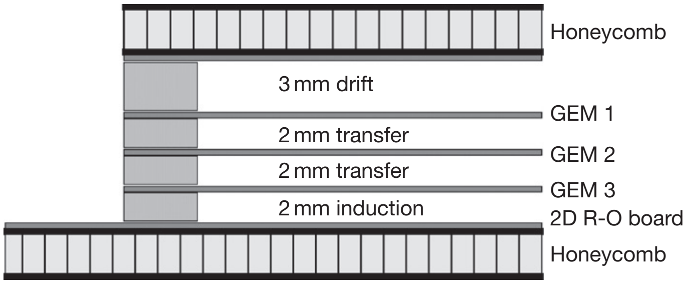

Figure 37 COMPASS triple-GEM schematics.

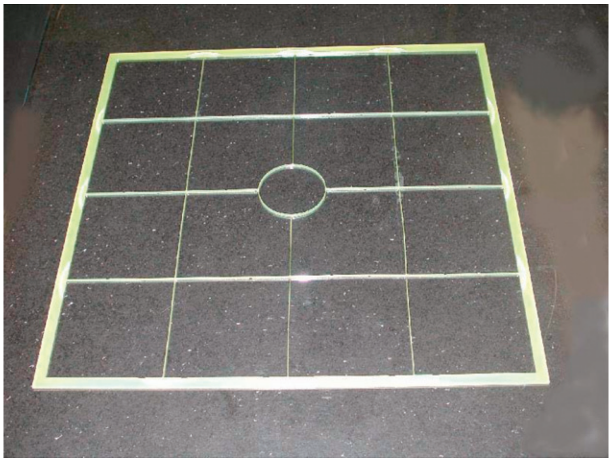

Figure 38 A thin fiberglass frame with internal ribs serving as GEM supports and spacers. The central round spacer corresponds to the beam killer diameter.

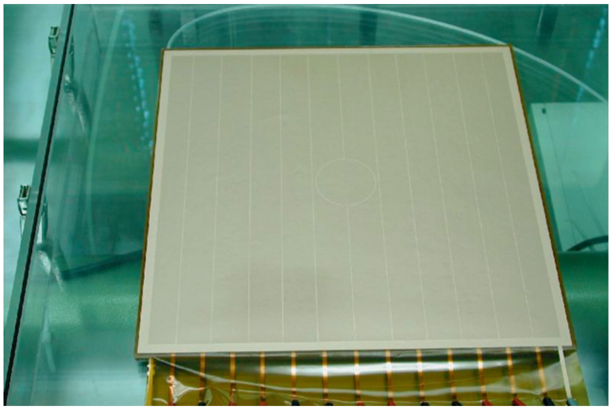

Figure 39 A framed GEM during assembly in the clean box. The individual lines providing the voltage to the sectors and to the beam killer central pad are visible.

The TOTEM T2 tracker at CERN has been built with a similar procedure; installed in the forward arms of the CMS experiment, the detector has, on each arm, two sets of semicircular TGEM chambers with a shape suited for installation very close to the collider vacuum tubes (Figure 41) (Bagliesi et al., 2010). The geometry of the GEM electrodes used was shown in Figure 11.

The flexibility of the thin GEM foils and the confinement of the amplification in the holes permit the realization of nonplanar detectors. Figure 42 shows several self-supporting GEM electrodes assembled and glued to a circular-shaped frame with the help of a removable mandrel (unpublished work of the GDD group at CERN). Using similar technologies, a radial TPC has been built and operated for the BoNus experiment at the Jefferson Laboratory aimed at studying the neutron structure from electron–neutron interactions. The device has a cylindrical gas volume with radial electric field surrounding a long, thin gas target, and a set of semicylindrical TGEM detecting the ionized trails drifting radially (Figure 43; Fenker et al., 2008).

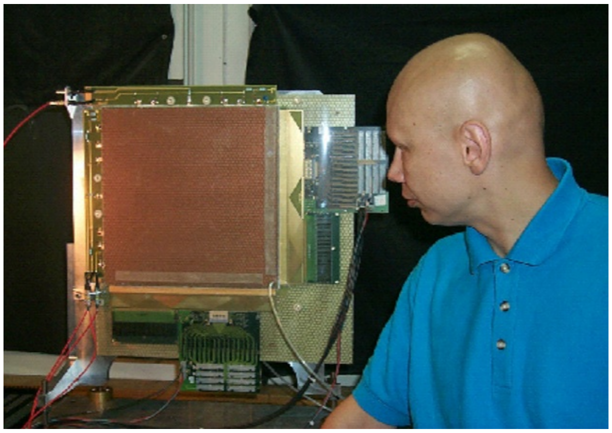

Figure 40 Leszek Ropelewski with a COMPASS triple-GEM prototype (picture by the author at CERN).

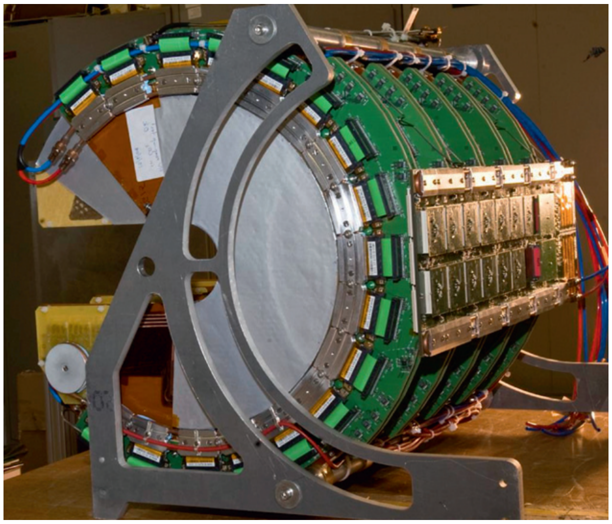

Figure 41 A set of semicircular GEM chambers before their installation in the TOTEM experiment; a second symmetric set closes around the beam tube from the left side.

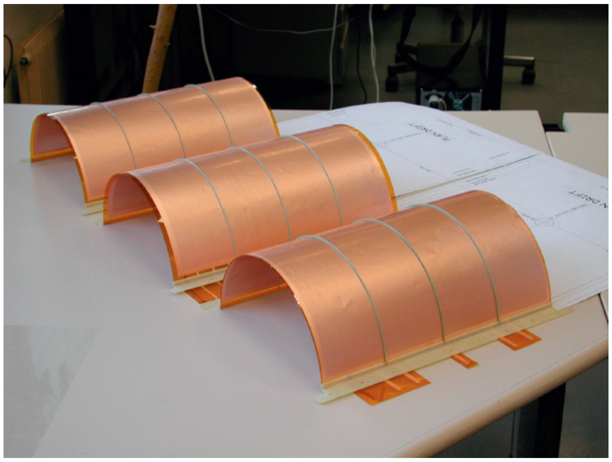

Figure 42 A set of cylindrical self-supporting GEM electrodes (picture by the author at CERN).

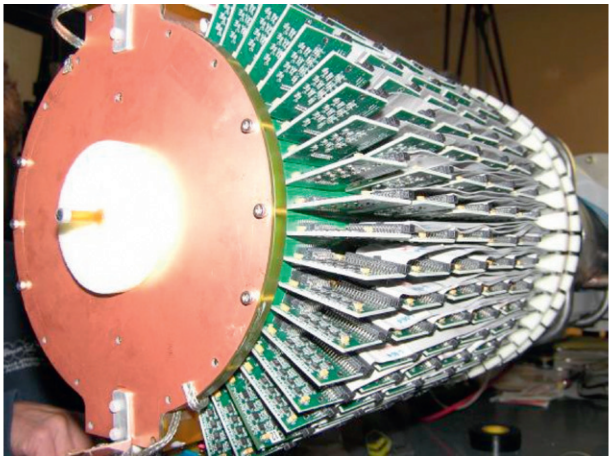

Figure 43 The BoNus radial GEM-TPC.

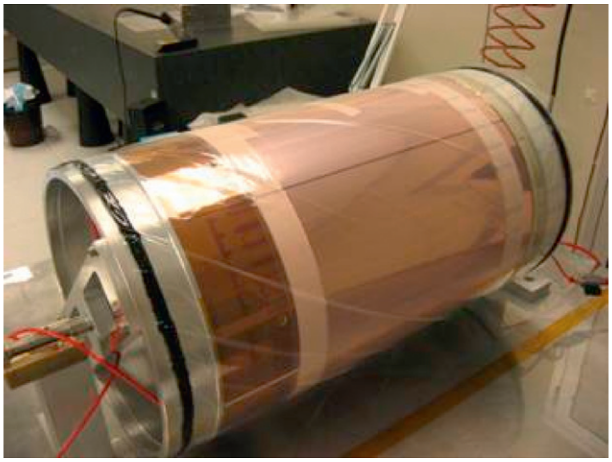

Figure 44 Cylindrical triple-GEM prototype for the KLOE-2 inner tracker.

Light cylindrical GEM detectors have been built and tested for the KLOE-2 inner tracker upgrade (Bencivenni and Domenici, 2007); a prototype is shown in **Figure 44**. Systematic measurements of efficiency and localization accuracy in magnetic fields confirm that the detector meets the experimental requirements (Balla et al., 2011).

8.22.7 GEM Detectors' Operation and Performances: Charged Particles

8.22.7.1 Fast Tracking and Triggering Systems

GEM devices have been used in a wide range of conditions, gas fillings and pressures, depending on the application and on the most critical experimental requirements: efficiency, energy resolution, space accuracy, and time resolution. For detectors used for high-intensity beam tracking in particle physics, additional requirements are possible rate dependence of efficiency, long-term operating stability, and, perhaps most critical of all, radiation resistance or aging properties.

The summary of performances presented here is based on the results obtained in the laboratory and in operating conditions with the COMPASS TGEM chambers. As operating gas, a 70–30 mixture of argon and carbon dioxide ensures full efficiency and stability of operation, and satisfies the nonflammability requirements met in most experimental setups.

The response of the detector depends critically on the performance of the readout electronics; the results described here have been obtained with the 128-channel amplifier-shaper ASIC APV25-S0, originally designed and widely used for the readout of silicon microstrip detectors (French et al., 2001). For the use with gaseous devices, a front-end external diode protection has been added (Noschis et al., 2007). While a detailed description of the circuit is outside the scope of this note, a short functional summary is provided here as reference to the results. The input signals from each strip are amplified and shaped with a 50-ns peaking time; the amplifier output is sampled at 40 MHz and stored in a 128-deep analogue pipeline. On an external request, generated by the fast trigger selection of the experiment, the analogue content for three adjacent cells in the time sequence corresponding to the trigger delay is read sequentially and digitized. The recorded information for each event corresponds then to the charge measured, in coincidence with the trigger, over the full detector area in three consecutive time intervals, 25 ns apart.

Due to the large strip capacitance, around 50 pF, the circuit has a noise of around 1500 electrons when connected to the detector. For minimum ionizing tracks, releasing $\sim$30 ion pairs in the drift gap, at gains around 4000 per coordinate and for an avalanche shared between three readout strips, the signal/noise ratio is about 15.

Use of the circuit, that does not provide a fast signal output, requires an external trigger for starting the readout and is therefore suited to the detection of charged particles. A simple method permits the recording of neutral events can, however, be used: the overall signal on the last GEM electrode is sensed with a separate fast amplifier, and after discrimination used as trigger with suitable timing. The method can be used for x-ray imaging, as well as for detector calibration (Bressan et al., 1999b).

The event reconstruction program finds the signal clusters, defined as the groups of adjacent strips with recorded charge above a preset threshold value, and determines the total charge of the cluster, its center (weighted average) and width. Although the time of the tracks is not directly measured, it can be deduced from a fit on the triple charge sample.

With reference to **Figure 37**, **Table 1** provides a summary of typical values of voltage applied to the various electrodes in the structure and of the corresponding effective incremental gains. As indicated before, a single power supply is used, with a resistive divider, to provide all voltages; the asymmetric gain configuration is the one that gives the highest immunity to discharges induced by heavily ionizing tracks. When reading out the space coordinates on two sets of strips, the effective charge gain for each projection is, of course, about half of the total.

In what follows, the most relevant operating performances of the COMPASS detectors, measured in high-energy charged particle beams, are described (Altunbas et al., 2002; Bachmann et al., 2001). **Figure 45** shows the total cluster charge measured on one coordinate for MIP perpendicular to the chamber; the smaller peak corresponds to the noise, measured with random off-beam

Table 1 Typical applied voltages and fields on the various electrodes of a TGEM chamber, operated in A-CO_2 70–30 at atmospheric pressure

Electrode	*Voltage (V)*	*Field (kV cm^{-1})*	*ΔV_{GEM} (V)*	*Effective gain*
Drift	4100	2.49		
GEM1 Top	3353		410	50
GEM1 Bot	2943	3.73		
GEM2 Top	2196		374	23
GEM2 Bot	1822	3.73		
GEM3 Top	1075		328	8.5
GEM3 Bot	747	3.73		
Readout	0			TOT 9775

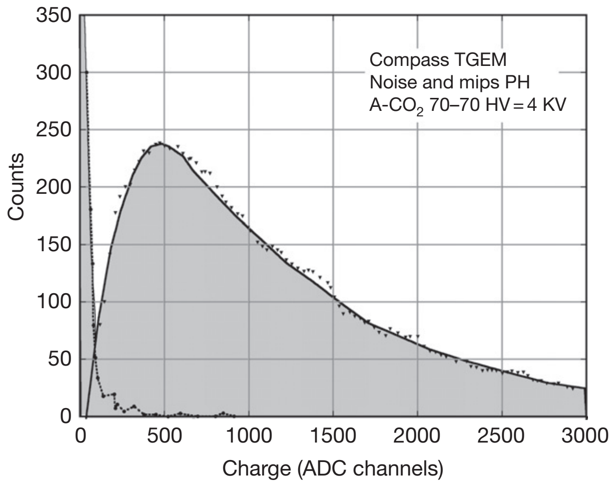

Figure 45 Noise and MIPS pulse height spectra measured with the COMPASS triple-GEM at standard operating conditions.

triggers. Figure 46 provides, for one coordinate, the detection efficiency and signal-to-noise ratio as a function of voltage; full efficiency is reached at −4100 V, corresponding to a total effective charge gain of around 9000 (see Table 1). (With the described equal sharing of charge between the two projections, the effective gain for each coordinate is 4500.) Similar results are obtained for the other coordinate; the linear correlation between cluster charges in the two projections (Figure 47) can be exploited to resolve ambiguities in the case of multiple tracks.

The uniformity of efficiency over the detector area in data-taking conditions is apparent in Figure 48, showing also the suppression of counting in the central region (the beam killer); the small local efficiency reduction due to the spacer's ribs is also visible.

The development of TGEM chambers with pixel readout, mentioned in Section 8.22.5 (Figure 35), permits the detection of high-intensity beams in the central region of the spectrometer; full efficiency has been obtained in muon beam runs at a flux up to 1.2×10^5 mm^{-2} s^{-1} (Krämer et al., 2008). To reduce multiple scattering, the detector construction is very light in the sensitive area, accounting for about 0.2% of radiation length.

The position accuracy that can be achieved with GEM trackers is a convolution of various dispersive effects: initial ionization, drift diffusion, and avalanche spread. For charged particles and analogue strip readout, the space coordinates of

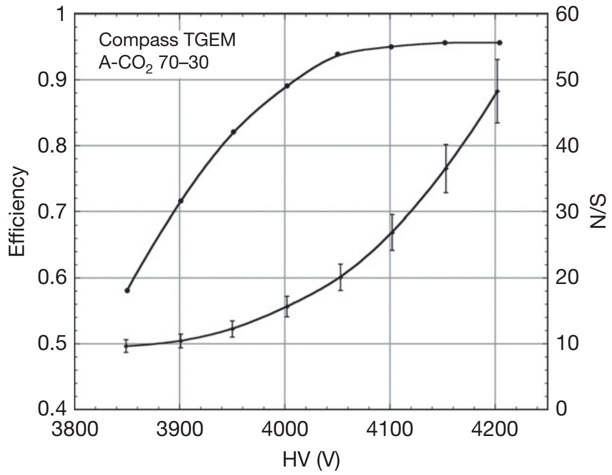

Figure 46 Efficiency and signal/noise on one coordinate for MIP as a function of applied voltage.

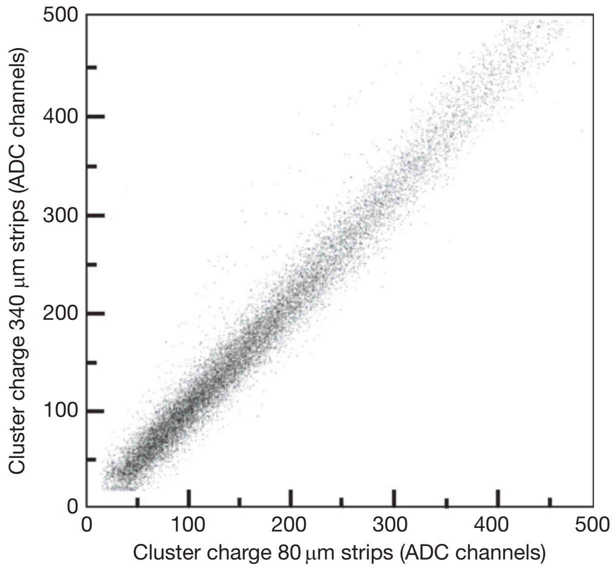

Figure 47 Cluster charge correlation for fast particles between the two coordinates.

tracks are obtained as weighted center of gravity over the cluster charge distribution, after pedestal subtraction and gain corrections. A position accuracy around 80 μm rms is obtained in both projections for fast particles perpendicular to the chambers, as shown in Figure 49 (Ketzer et al., 2004).

In their development of the x-ray polarimeter, to be described later, using a narrow pitch GEM and a dedicated solid-state pixel readout, Bellazzini et al. (2007b) have demonstrated an intrinsic position accuracy better than 50 μm.

The time resolution of the chambers, deduced from a fit to the charge measured in three consecutive time bins, is around 12 ns rms. In view of the use of GEM detectors for a fast trigger selection, systematic studies aimed at improving the intrinsic time resolution have been made, comparing the results obtained in a range of detectors' geometry and gas filling (Alfonsi et al., 2004; Bencivenni et al., 2002c). As expected, the best resolutions are obtained with thin transfer gaps and fast gases, reducing the

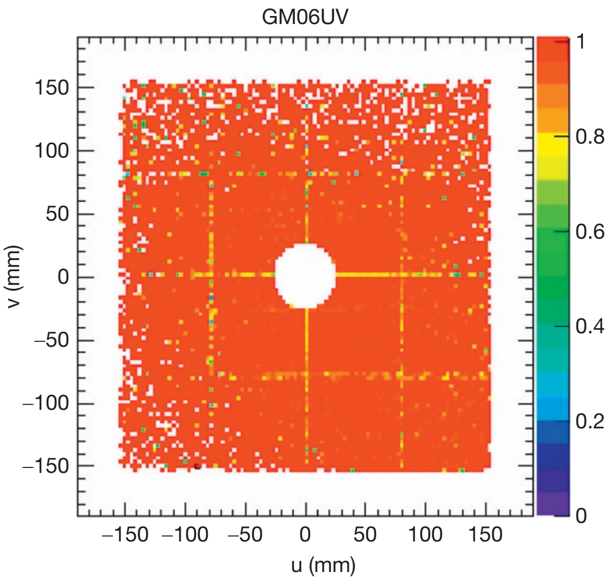

Figure 48 Efficiency measured over the detector area. The central region corresponds to the voltage-controlled beam killer; small losses around the spacers are visible.

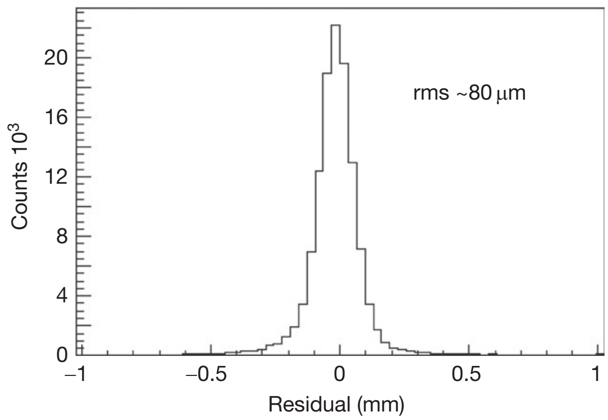

Figure 49 Position accuracy distribution for one coordinate measured for fast particles.

electrons dispersions in the drift and the avalanche propagation: for a mixture containing carbon tetrafluoride, the rms of the resolution is 4.5 ns, a factor of two better than with a standard argon–carbon dioxide mixture (**Figure 50**). Full efficiency can then be reached within a 25-ns time window, corresponding to the beam crossing separation of the LHC.

8.22.7.2 End-Cap Readout for TPC

Use of the new technologies to instrument the end-cap detector in TPC has been considered by many groups. Compared to conventional MWPC readouts, MPGDs have several potential advantages: a simpler and more reliable mechanical construction, better single- and multitrack resolution, absence of magnetic field-induced track distortions due to the nonparallel field geometry close to the anode wires (the so-called ExB effect), and substantial reduction of the field-distorting effects of positive ions.

Initially motivated by the ongoing development of detectors for the International Linear Collider, the GEM-TPC concept has been adopted in other fields of particle and nuclear physics. Thorough experimental and simulations works aim at optimizing the operating conditions of a GEM-TPC to achieve the best performances (Carnegie et al., 2005; Kappler et al., 2004; Killenberg et al., 2004; Ledermann et al., 2007; Yu et al., 2003). **Figure 51** shows a large-size TPC prototype with three GEM readout modules being inserted in a magnet for resolution studies (Schade and Kaminski, 2011).

Particular attention has been given to the study of shape, geometry, and size of the readout pads, in view of reducing the number of readout electronics channels needed to instrument large detectors; examples of patterns analyzed both theoretically and experimentally are shown in **Figure 52** (Kaminski et al., 2006; Ledermann et al., 2007). Despite some advantages of the chevron-like patterns, particularly for inclined tracks, preference is given usually to the simpler parallel pad geometry; staggered rows permit to improve localization, partly obliterating the quantization error due to the discrete pad sizes (Carnegie et al., 2005; Karlen et al., 2005; Oda et al., 2006; Schade and Kaminski, 2011). **Figure 53** shows an example study of the effect on resolution of the pad size (Kaminski et al., 2006).

A way to preserve and even improve the localization properties of detectors while reducing the number of readout pads has been devised, introducing a high resistivity foil between the active part of the device and the signal pickup electrodes (Dixit et al., 2004). With proper balance of the foil resistivity and local capacitance, the induced signal is spread over a larger area, thus reducing the required number of pads or strips for readout. In **Figure 54**, a comparison of transverse resolution measured with a GEM-TPC prototype with and without a resistive foil shows the advantage of the resistive dispersion approach (Boudjemline et al., 2007). Possible drawbacks of the method are the difficulty to achieve a uniform response over large areas and reduced rate and multitrack resolution, due to the longer integration time of signals.

For large TPC detectors, the most suitable choice is a gas with low electron diffusion in magnetic field and high drift velocity at moderate values of field. Because of the very large volumes, a major constraint is the use of nonflammable gas filling; performances in mixtures of argon, carbon dioxide, methane (below 5%), and carbon tetrafluoride have been extensively compared. A good compromise is found in the so-called TDR (TESLA Technical Design Report) gas ($Ar–CH_4–CO_2$ 93–5–2); in **Figure 55**, measurements of transverse resolution as a function of drift length are given for several values of the magnetic field and two pad rows geometries (Janssen et al., 2006). Mixtures containing CF_4 are a good option, because of the reduced electron diffusion (Kobayashi et al., 2011); as shown in **Figure 56**, a transverse resolution below 100 µm rms is achieved at 1 T with an $Ar–CF_4–iC_4H_{10}$ 95–3–2 mixture.

Due to its extremely low electron diffusion, particularly in high magnetic fields, use of pure CF_4 provides the best localization accuracy, both in the transverse and in the longitudinal drift direction. As noted before (**Figure 25**), the operation requires, however, GEM potentials almost double compared to other mixtures. A GEM-TPC detector has been tested in pure CF_4, demonstrating its superior performances as compared to other gases (**Figure 57**): without magnetic field, the transverse

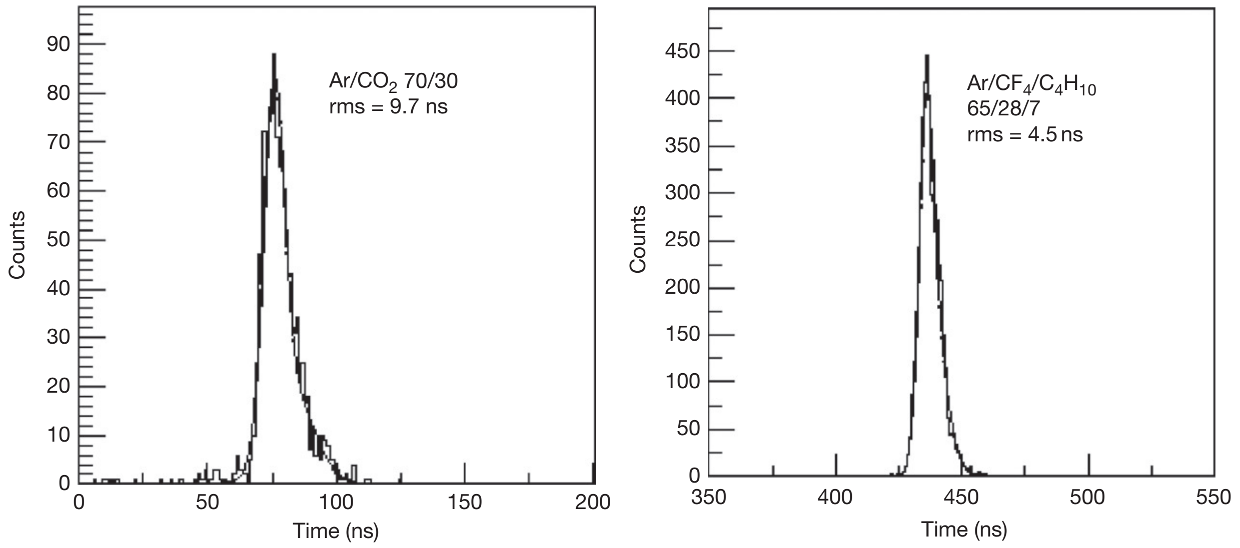

Figure 50 Time resolution for fast particles measured with the LHCb chambers in Ar–CO_2 (a) and Ar–CF_4–C_4H_{10} mixtures (b).

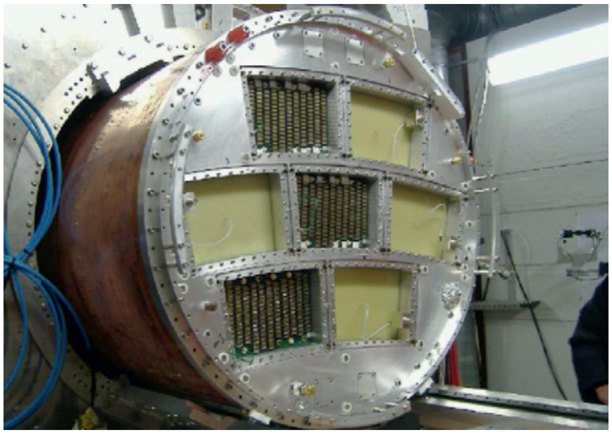

Figure 51 A prototype large-size TPC with modular GEM readout for International Linear Collider.

resolution obtained with CF_4 is comparable to those measured with other gases at high values of the magnetic field (Oda et al., 2006).

GEM-based TPC of various designs are in operation or under development for application in nuclear physics. Figure 58 shows an event recorded with the BoNus radial TPC, described previously (Fenker et al., 2008). Other examples are the GEM-TPC for LEGS, the Laser Electron Gamma Source at BNL (Yu et al., 2005), the PANDA detector at the Facility for Antiproton and Ion Research at Darmastadt (Fabbietti et al., 2011), AMADEUS at DAΦNE in Frascati (Poli Lener et al., 2010), and the detector aiming at the observation of two-proton radioactive decays (Blank et al., 2010). Figure 59, from the last reference, shows an example of reconstructed two-proton tracks in the decay of an ^{45}Fe ion stopping in the sensitive gas volume.

Using TIMEPIX, an ASIC chip originally designed for reading solid-state pixel detectors (Llopart et al., 2007), the single cluster imaging properties of a small volume TPC have been demonstrated; Figure 60 shows an ionizing particle crossing the sensitive volume and ejecting a long-range delta electron (Bamberger et al., 2007). Along the same lines, and manufacturing a MICROMEGAS-like gaseous amplifier directly over the electronics chip, a large effort is under way to implement micro-TPC with single-electron detection capability and very high granularity (Campbell et al., 2005; van der Graaf, 2009; van der Graaf et al., 2006). Since the active chip can be easily damaged by a discharge, several methods of protection making use of resistive layers have been developed (Bilevych et al., 2011).

8.22.7.3 Positive-Ion Feedback

As mentioned, only electrons are collected on the readout electrode; positive ions, produced in the avalanche process, recede along the field lines and are collected by the various electrodes, in proportions that depend on geometry and fields. For a single GEM, at the values of drift field used for detection of ionizing tracks, the upper GEM and the drift electrodes almost equally share the collection of positive charge. In multi-GEM structures, as most of the ions are produced in the last stage, the fractional ion backflow reaching the drift gap is substantially reduced. Measured with a double-GEM detector, Figure 61 (Bachmann et al., 1999) shows the electron transparency of the first GEM and the fractional ion current reaching into the drift gap as a function of drift field, for an operation that favors the gain in the second multiplier. (The fractional ion feedback is defined as ratio of positive current on the drift electrode to the (negative) current collected at the anode.) At a drift field around 500 V cm^{-1}, ensuring full collection of the primary ionization, the fractional ion feedback is ~5%.

Systematic studies have attempted to reduce this value, particularly relevant in large-volume TPC as it might affect the drift fields with the consequent track distortions. (The perturbation induced by the accumulation of positive ions in TPC depends on the detected particles flux. An often quoted 'rule of thumb' says that, as far as the fractional feedback is lower than the inverse gain of the detector, the effect is comparable to the one produced anyhow by the primary ionization.) Figure 62 (Bondar et al., 2003) gives the gain

Figure 52 Examples of pad row patterns used for the readout of time projection chambers: parallel with offset (left) and chevron (right).

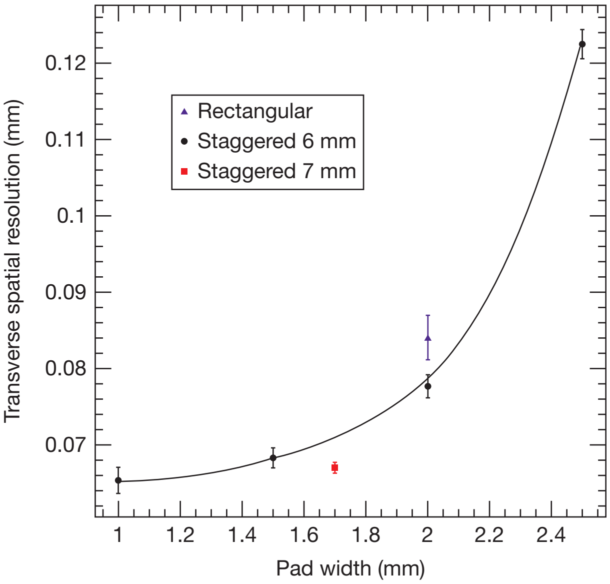

Figure 53 Transverse resolution for tracks perpendicular to the pad rows as a function of pad width and shape.

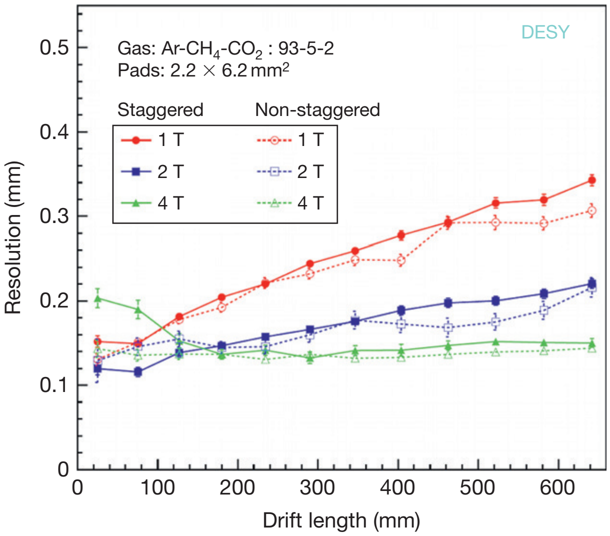

Figure 55 Transverse resolution measured with the International Linear Collider GEM-TPC prototype as a function of magnetic field and pad geometry (TRD gas).

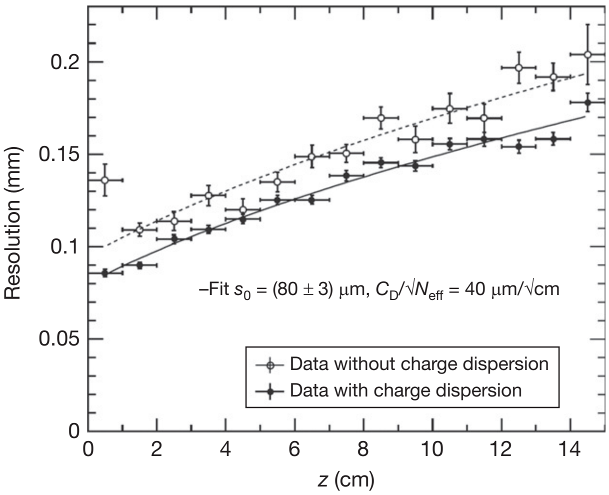

Figure 54 Comparison of transverse localization accuracy measured with a GEM-TPC detector without and with resistive charge dispersion on the readout.

dependence of the fractional ion feedback measured with a TGEM in various conditions; at a gain of 10^4, an upper limit for TPC operation, the feedback is below 1% for low drift fields.

The operation of a GEM-TPC in a strong magnetic field, parallel to the electric drift field, reduces the fractional ion backflow, probably as a result of the increase in electron transparency due to the reduction of transverse diffusion; an example is given in Figure 63 (Killenberg et al., 2004).

Ways to reduce the ion feedback exploiting the difference in diffusion of electrons and ions have been investigated, requiring the construction of multi-GEM detectors with an offset in the facing holes, achievable with THGEM electrodes (Sauli et al., 2006).

In photosensitive GEM detectors, ions reaching the photocathode may result in permanent degradation of the quantum efficiency; special ion-gating structures capable of reducing this problem have been studied in the development of sealed devices sensitive to visible light, and will be discussed in Section 8.22.8.2.

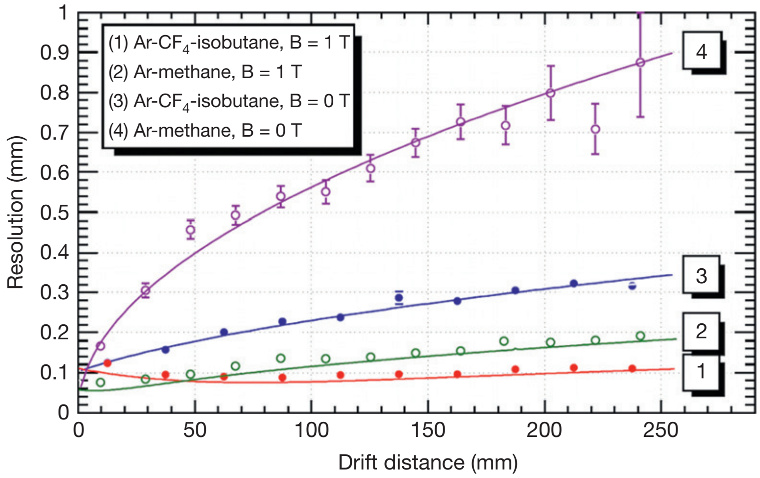

Figure 56 GEM-TPC resolution measured in several gas mixtures.

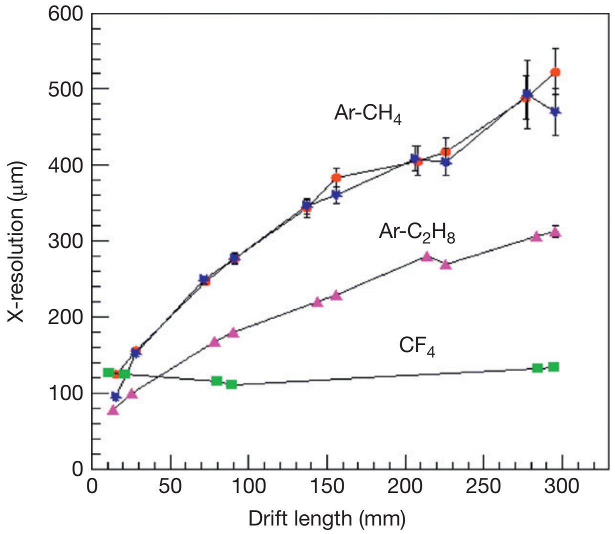

Figure 57 Transverse resolution as a function of drift length measured with a GEM-TPC in several gases (without magnetic field).

8.22.7.4 Rate Capability and Radiation Resistance

In wire-based proportional counters and chambers, the buildup of space charge due to slow positive ions, with the ensuing electric field modifications, determines a quick drop of gain, and therefore detection efficiency, at high radiation fluxes. Independent from the detector gain and the source of ionization, the gain drop begins at charge production rates of around 10^9 electrons per second per millimeter of wire (Walenta, 1981); in normal operating conditions, this corresponds to an MIP flux around $10^4\ s^{-1}\ mm^{-2}$ (Breskin et al., 1974). Despite decades of research, this is still a limit in modern wire detectors (Alexa et al., 2002); only the introduction of the new families of MPGD has allowed one to improve the rate capability of gaseous devices by several orders of magnitude (Sauli, 1998).

In GEM detectors, the increased rate capability is a consequence of two factors: the short, high field transfer gaps resulting in a fast clearing of the ions, and the screening effect from external fields due to the holes' narrow geometry. Moreover, since the multiplying charge is spread over several holes, due to the avalanche confinement effect each hole acts independently; the gain, measured with a soft x-ray (**Figure 64**) (Benlloch et al., 1998a), is unaffected up to a flux above $10^6\ s^{-1}\ mm^{-2}$, two orders of magnitude higher than for MWPCs. To avoid errors due to occupancy, the measurement is done in a pulse mode only up to rates of $\sim 10^5\ s^{-1}\ mm^{-2}$, and in the current mode above. Due to their coarser geometry or current-limiting electrodes, tick-GEM and resistive-GEM structures have a more limited rate capability (Peskov et al., 2012b).

Prolonged exposure to radiation is known to cause progressive degradation of performances in gaseous counters, in a process commonly named aging, due to the dissociation and successive aggregation of organic molecules, either constituent of the gas mixture or present as residual contaminants. The formation of deposits on electrodes affects permanently the electric field, and therefore the gain, a process particularly effective in thin wire chambers and even more in MSGCs (Capeáns, 2003; Hohlmann et al., 2002). Thanks to their conception, GEM devices are less affected by the presence of deposits on electrodes, and are therefore more tolerant to the presence of pollutants in the gas. In accelerated aging tests, realized with continuous exposure to high-rate soft x-rays, no degradation of performances has been observed up to an accumulated charge of several tens of mC per mm^2 with argon–CO_2 gas fillings (Altunbas et al., 2003; Guirl et al., 2002).

The addition of carbon tetrafluoride to the gas mixture, thanks to its etching properties, has been demonstrated to prevent and even cure the most insidious kind of aging in wire chambers, due to the deposit of silicon compounds (Openshaw et al., 1991). Use of CF_4 in gaseous detectors requires, however, special care, due to the strong reactivity of fluorine released in the avalanches; combining with water, it can produce hydrofluoridric acid, very aggressive for many materials (Akesson et al., 2002).

Gas mixtures containing CF_4 have been used to improve the time resolution of GEM detectors, as discussed before; exposures to high radiation levels, to study the tolerance of the detectors, have clearly shown damages to the structures at low gas flows (Alfonsi et al., 2005). With suitable control of materials

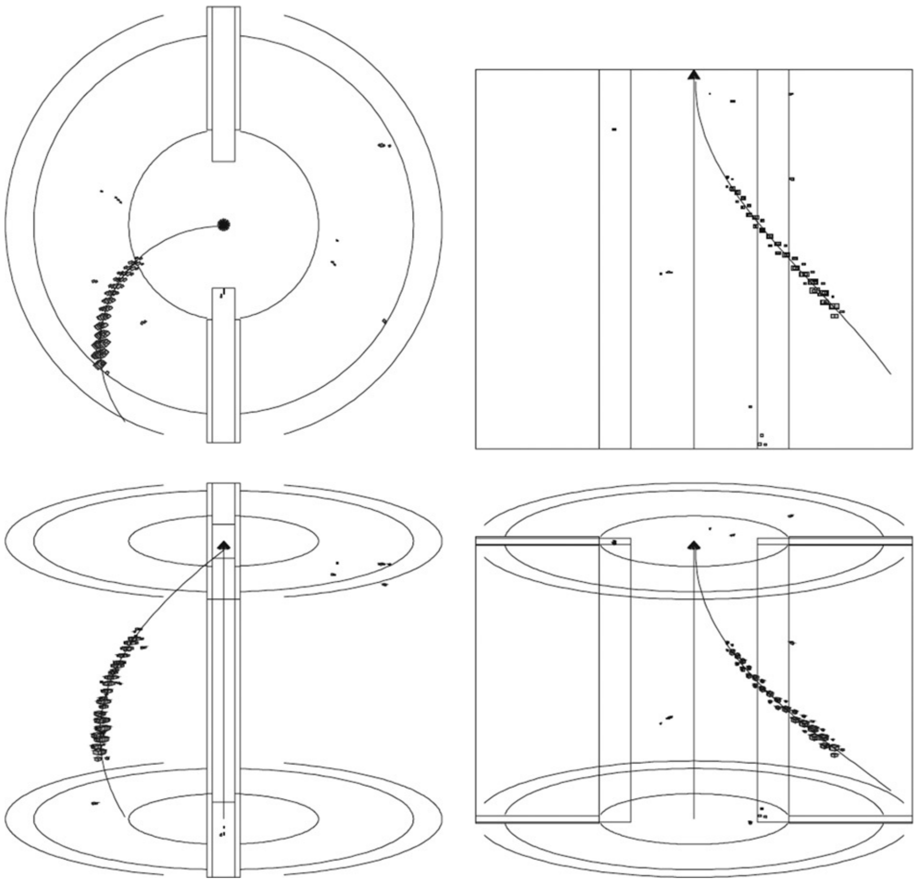

Figure 58 Three-dimensional reconstruction of a spectator proton produced by e–n interactions in the BoNus radial TPC.

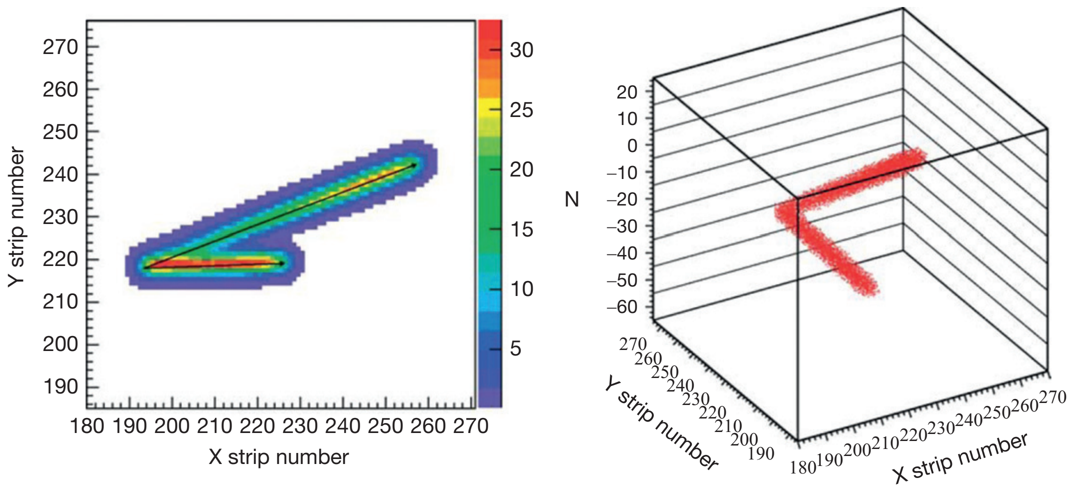

Figure 59 A two-proton decay from a stopping ^{45}Fe ion.

and gas flow, however, the detector lifetime under irradiation mixture has been demonstrated to exceed the experimental requirements. In Figure 65, the normalized gain of a TGEM detector under continuous irradiation is given as a function of collected charge (Alfonsi et al., 2004); there is no sign of change up to $20\,\mathrm{C\,cm^{-2}}$. For a typical detector gain of a few thousand, this corresponds to an integral MIP flux around $4 \times 10^{14}\,\mathrm{cm^{-2}}$.

It should be noted that accelerated aging tests are only indicative, and often optimistic, due to the delicate balance between etching and polymer formation in the dense charge plasma generated at high radiation fluxes; confirmation

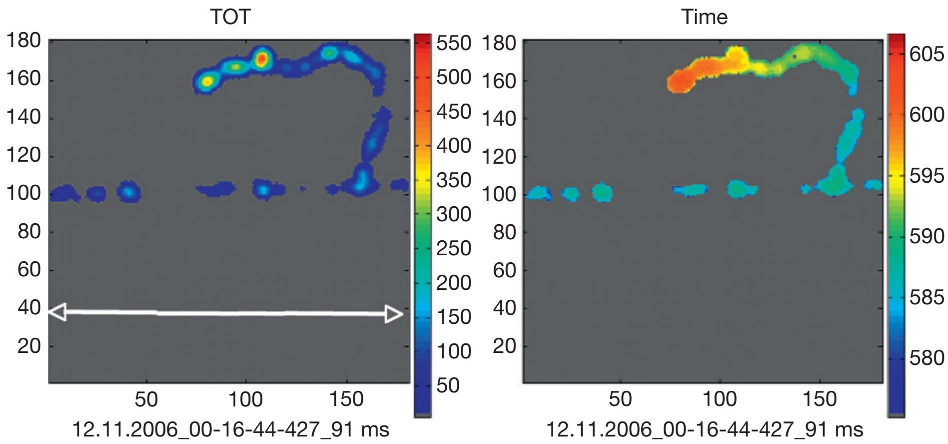

Figure 60 Fast particle track with a delta ray recorded with the TIMEPIX-GEM. Shades represent recorded charge on the left and time on the right.

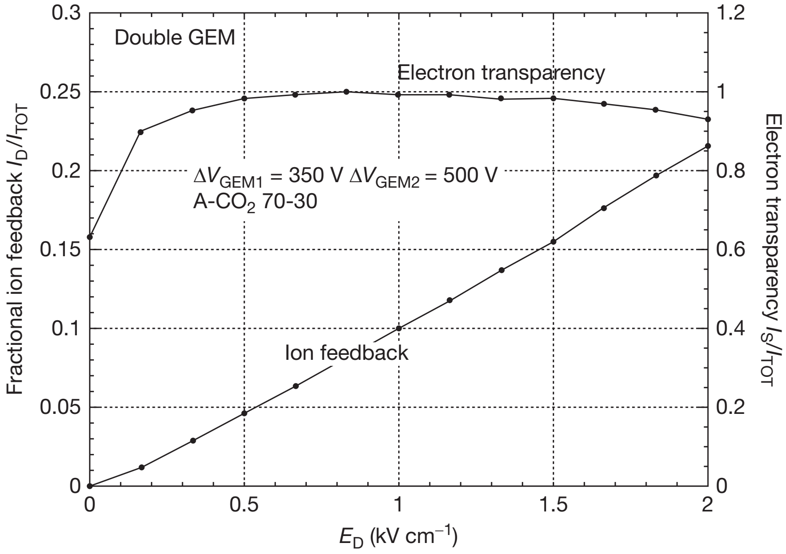

Figure 61 Drift electron transparency and fractional ion feedback as a function of drift field for a DGEM.

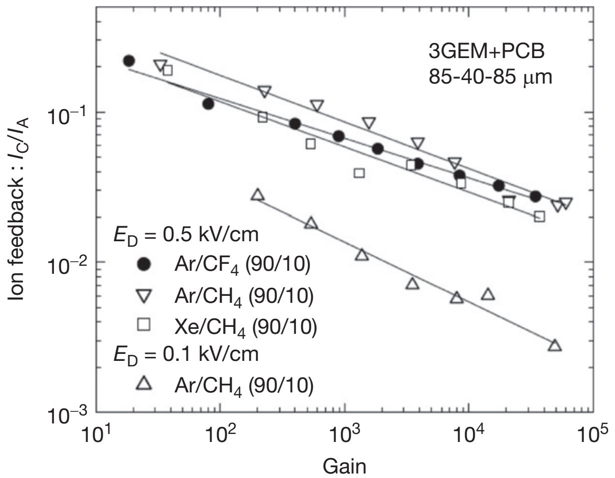

Figure 62 Fractional ion feedback as a function of gain in a TGEM.

can only come from long-term use in real experimental conditions.

8.22.8 Detection of Neutral Radiation

8.22.8.1 Ultraviolet Photons and RICH Applications

The high gains that can be attained in multi-GEM devices make them suitable for the detection and localization of single electrons produced by ionization of a photosensitive compound added to the gas mixture, as demonstrated in the early developments of the technology (Va'vra and Sharma, 2002; Va'vra et al., 1999). Following the progress in the development of Cherenkov ring imaging (RICH) detectors, a more promising approach is the use of internal cesium iodide (CsI) photosensitive layers, either semitransparent, deposited on the entrance window, or reflective, on the first GEM in a cascade. The second geometry is particularly favorable, since the screening

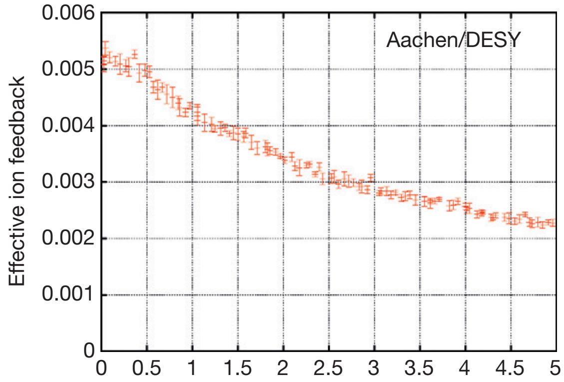

Figure 63 Reduction of the positive-ion fractional feedback with magnetic field.

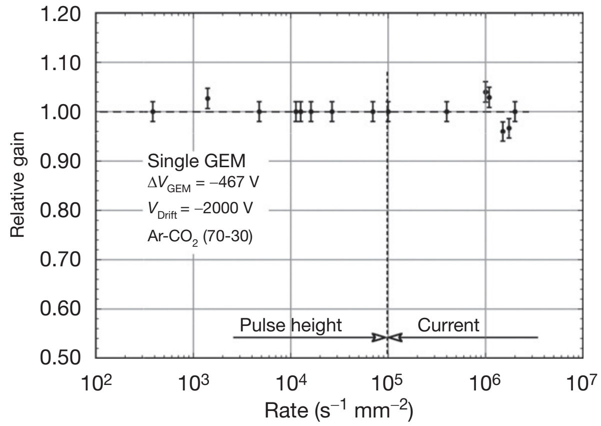

Figure 64 Normalized gain as a function of flux (5.9 keV x-rays).

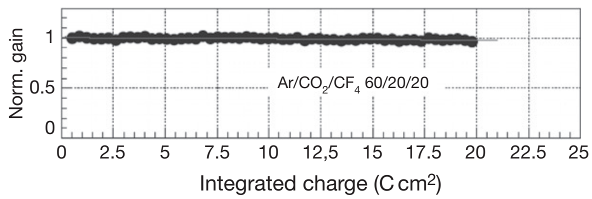

Figure 65 Normalized gain as a function of collected charge. The total charge of 20 C cm^{-2} corresponds to an integral fast particle flux around 4×10^{14} cm^{-2}.

effect of the electrodes obscures feedback processes induced by secondary photons emitted by the avalanches in the multiplication; the reduction of efficiency resulting from the optical transparency of the GEM electrode is compensated by the intrinsic larger efficiency of reflective photocathodes. (Reflective photocathodes are also easier to manufacture, since they do not need a rigorous thickness control.) As seen in Figure 66, with an appropriate choice of the geometry and voltages, all electron drift lines generated from the upper GEM surface enter the holes, where the first step of amplification occurs: further electrodes in a cascade then allow to one attain the gain needed for detection (Meinschad et al., 2004).

Efficiency, transmission, and localization properties of the multi-GEM detector with photosensitive CsI deposits have been extensively studied. Many parameters affect the detection efficiency, starting with the photoelectron extraction probability, that depends on the field on the photocathode surface and on the filling gas; **Figure 67** is a compilation of measured extraction efficiency, relative to vacuum, as a function of field for semitransparent CsI photocathodes in several gases at atmospheric pressure (Breskin et al., 2002a). Due to their large backscattering cross section, high fields are required to reach efficiency in mixtures containing noble gases, while in methane and carbon tetrafluoride full extraction is achieved at lower fields (Cohelo et al., 2007). More recent measurements (**Figure 68**; Alexeev et al., 2010b) show that quantum efficiency close to the one of pure methane can be reached with argon–methane mixtures.

The choice of the gas filling is particularly crucial using reflective photocathodes, since the voltage applied to the GEM electrode sets a limit to the surface field that can be reached. Systematic investigations of surface field, collection efficiency, and gain have been made, for both standard and THGEM detectors. **Figure 69** is an example of measured photoelectron collection efficiency as a function of voltage for several GEM geometries (Mörmann et al., 2004); the curve labeled dc140 corresponds to the standard GEM geometry (50 μm polymer, 70 μm holes diameter at 140 μm pitch). Not surprisingly, a larger pitch (200 μm for the curve dc200) results in a reduced efficiency.

A similar optimization work has been done for THGEM geometries; **Figure 70** is a comparison of measured electron collection efficiency for a 0.4-mm-thick, 0.3-mm-hole-diameter detector in argon–methane and carbon tetrafluoride (Chechik et al., 2005). As expected, the operation in CF_4 requires higher voltages, but similar efficiencies are obtained at lower TGEM gains.

The hadron blind detector (HBD) is the first large-scale application of photon-sensitive GEM devices; it consists of a Cherenkov radiator operated in pure CF_4 directly coupled in a windowless configuration to a TGEM detector with a CsI photocathode and pad readout (Aidala et al., 2003; Fraenkel et al., 2005). The detector has two identical arms of semi-cylindrical shape, each with a 50-cm-thick radiator; photons emitted by the Cherenkov effect in the radiator are detected by an array of CsI-coated photosensitive GEMs (**Figure 71**; Anderson et al., 2011). A reverse field applied to the radiator volume ensures that no ionization electron charge is directly collected. Successfully operating in the PHENIX experiment at RHIC, the detector has reached the design goal for hadron rejection.

A major motivation for the development of photosensitive GEMs is their use as sensors for Cherenkov ring imagers. Compared to the well-established multiwire chambers, the GEM approach has several distinctive advantages: a reduction of the sensitivity to direct ionization by charged particles, thanks to the reverse field configuration in the gap between window and photocathode; and high gains ensuring single photoelectron detection and higher rate capability. To this, one should add a better intrinsic localization accuracy and two-photon resolution. Exposing a TGEM with reflective CsI photocathode to a collimated UV photon source, position accuracies and

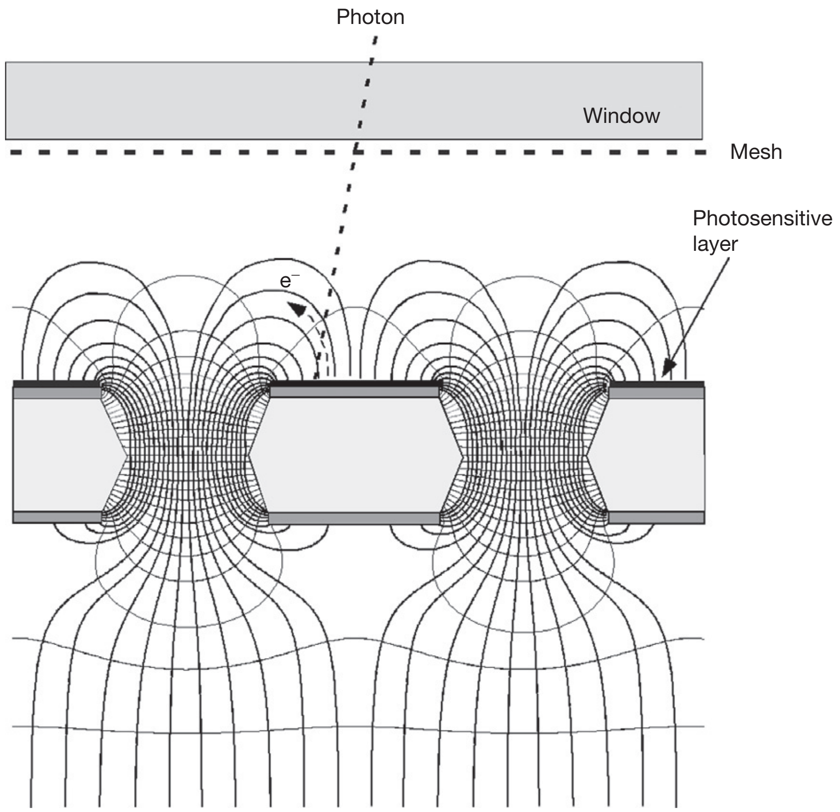

Figure 66 Equipotentials and field lines in a GEM optimized for detection of electrons ejected from the upper photosensitive surface.

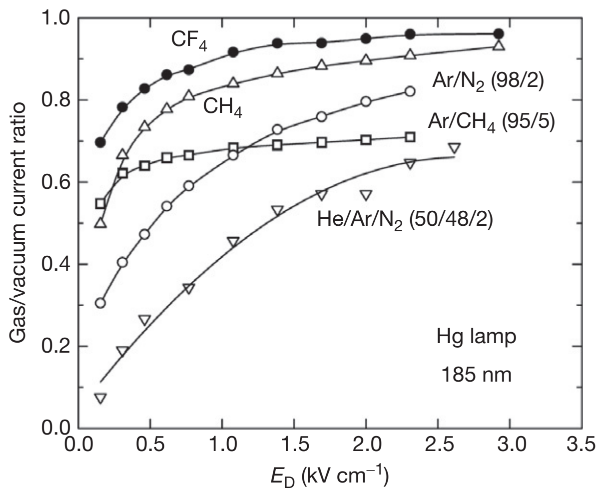

Figure 67 Quantum efficiency relative to vacuum of a semitransparent CsI photocathode as a function of field in several gases at atmospheric pressure.

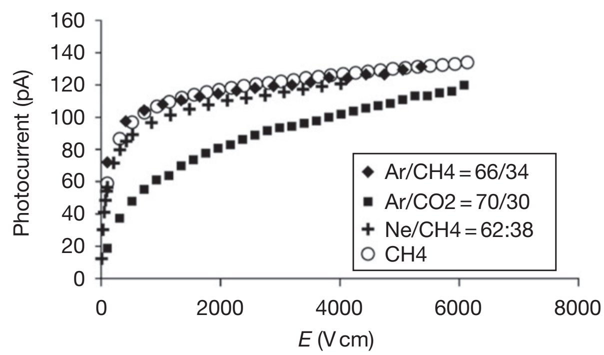

Figure 68 Relative quantum efficiency of CsI photocathodes as a function of field in several gases at atmospheric pressure.

two-photon resolutions around 200 μm have been achieved as shown in Figure 72 (Meinschad et al., 2004).

For large systems, preference is given to the THGEM, mechanically sturdier and easier to handle, particularly in the delicate phase of the CsI deposition; this is the solution adopted for the development of the COMPASS RICH upgrade. Systematic studies aim at achieving the large gains required for the efficient detection of single photoelectrons (Alexeev et al., 2010a, 2011). A still open issue concerns the reliability of such devices in realistic operating conditions, particularly in the presence of ionizing background; although high gains can be attained with single-THGEM electrodes, multi-THGEM detectors ensure a more stable operation.

A small-size Csi-THGEM detector, prototype for the ALICE RICH upgrade, has been successfully tested in a beam; use of neon-rich mixtures seems to permit reaching higher single-electron gains (Martinengo et al., 2011). Figure 73 shows integrated Cherenkov ring events from a liquid C_6F_{14} radiator, recorded with a composite triple-THGEM prototype with pad readout operated in neon + 10% methane (Peskov et al.,

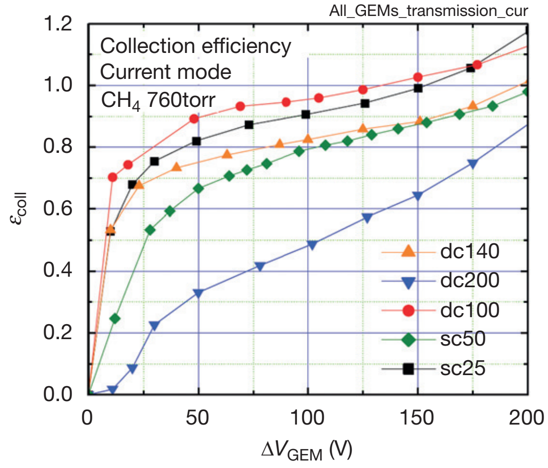

Figure 69 Photoelectron collection efficiency of CsI-coated thin GEM electrodes of different geometry.

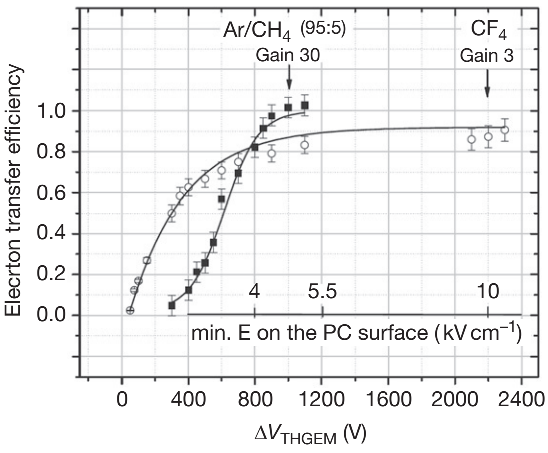

Figure 70 Electron collection efficiency for a CsI-coated THGEM as a function of voltage in argon–methane and carbon tetrafluoride.

2012a); the central area corresponds to the direct detection of the beam.

8.22.8.2 Sealed Detectors of UV and Visible Light

In view of possible scientific and commercial applications, several attempts have been made to manufacture sealed photosensitive gaseous detectors, including one or more GEM electrodes. To avoid damages to the photocathode, thorough cleaning and outgassing procedures have to be followed; this has been rather successful using CsI semitransparent or reflective sensitive layers and three or four standard small-size GEMs in cascade with the small-size prototype shown in Figure 74; high gains and quantum efficiencies close to vacuum could be attained (Breskin et al., 2001). Similar results have been described by Tokanay et al. (2011). In the medium term however, due to both residual contamination and ion feedback damages, the quantum efficiency deteriorates with exposure to light (Breskin et al., 2002b).

To try and solve the ion damage problem, particularly in view of the development of visible light detectors with bialkali photocathodes, several structures aiming at reducing the ion feedback have been devised; some of these patterns were shown in Figure 16. In the MHSP GEM, insertion of thin independently powered strips on the back side of the first GEM in a cascade permits to reduce the ion backflow by an order of magnitude compared to a standard geometry (Maia et al., 2004); with more complicated structures, medium-term stable operation with bialkali K–Cs–Sb has been demonstrated at gains up to 10^5 (Breskin et al., 2010; Lyashenko et al., 2009). Figure 75, from the last reference, compares the gain obtained with different structures having semitransparent CsI and bialkali photocathodes. The onset of a gain divergence due to feedback is seen for the standard double-GEM device at a voltage exceeding 270 V.

8.22.8.3 Detection and Imaging of Soft x-Rays

Soft x-ray sources are commonly used in the development of detectors. As for other gaseous counters, the energy resolution is limited by the avalanche statistics; local gain variations due to the tolerance in hole diameters and to charging-up processes add up to the dispersion. Figure 76 shows an example of ^{55}Fe 5.9 keV spectrum measured with a small single-GEM detector at a gain of 5×10^3 (Bressan et al., 1999b); the FWHM of the main peak is about 20%. While not exceptional, this resolution is generally good enough for many applications, in particular medical imaging. Systematic resolution studies have been reported in a range of gas mixture, gain, drift, and transfers fields, and also in combination with other MPGD structures (Mir et al., 2007).

The self-triggering capability of the detectors, obtained exploiting the positive-induced signal on the last GEM electrode, and the sub-mm position accuracy make them interesting for medical imaging; the detection efficiency can be enhanced using thick drift gaps and/or heavier gas fillings. Figure 77 shows a soft x-ray absorption radiography of a small mammal (Sauli, 2001). While of limited interest due to the low energy, the measurement illustrates the imaging properties of the detector.

A GEM-based one-coordinate soft x-rays detector for wide angular scattering experiments is shown in Figure 78 (Aulchenko et al., 2007, 2009). It consists in a radial conversion and drift volume, with an arc-shaped TGEM detector; radial readout strips provide the scattering angle. This geometry permits to use thick conversion volumes without parallax errors caused by the photon conversion depth.

The very high-rate capability of GEM devices has been exploited for fast 2D imaging of the VUV and soft x-ray emissions in magnetic fusion plasmas (Pacella et al., 2001). The images, consisting in a small-size pinhole camera with 128, 2 mm^2 pixels readout, have been demonstrated to have a linear response up to rates of 4 MHz per pixel, and provide time-resolved 2D images of the plasma activity at sampling frequencies up to 20 kHz. With thin input windows and helium or vacuum separation from the source, the imager efficiently detects photons from few hundred eV to several keV (Figure 79; Pacella et al., 2003); the field of view can be changed adjusting the detector–plasma distance. Figure 80 shows an example of time-resolved image of x-ray plasma activity recorded at the Italian National Spherical Tokamak Experiment. Other

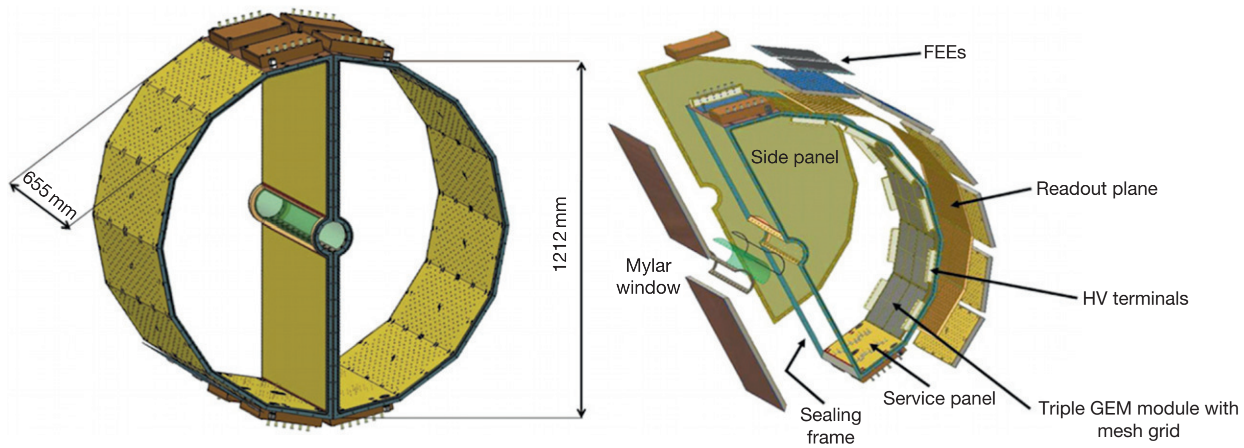

Figure 71 Schematics of the hadron-blind detector at RHIC.

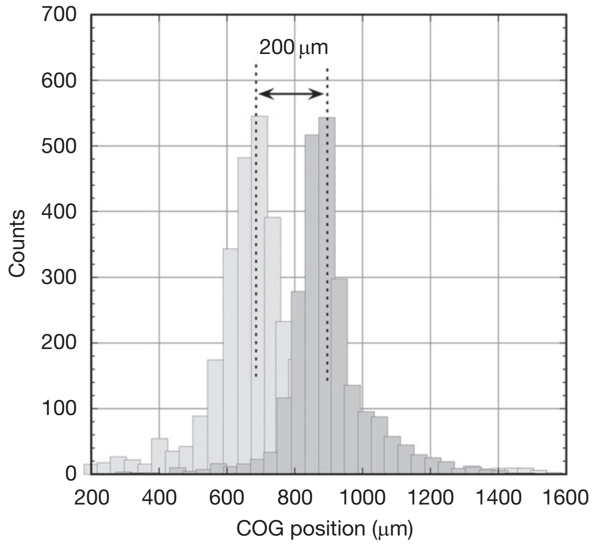

Figure 72 Center of gravity distributions for two positions of the collimated UV photons source, measured with a standard TGEM with reflective CsI photocathode.

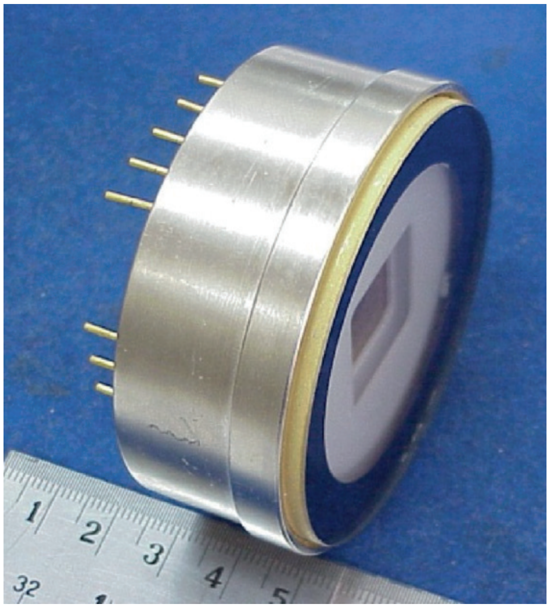

Figure 74 Small-size sealed GEM gaseous photomultiplier.

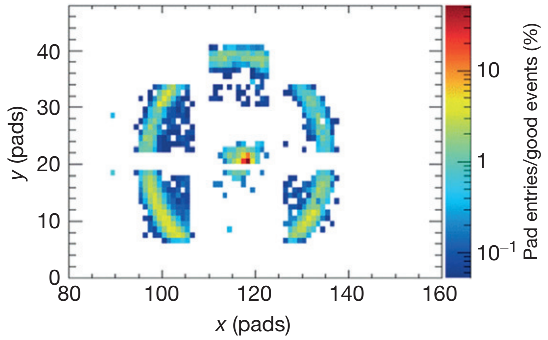

Figure 73 Integrated Cherenkov rings recorded with a CsI-coated triple-THGEM with pads readout.

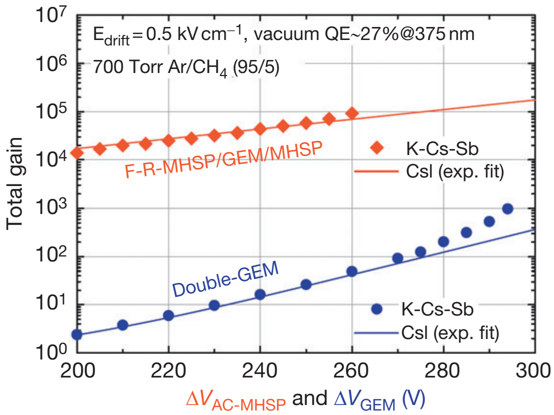

Figure 75 Single photon gain of sealed multi-GEM detectors with semitransparent CsI and bialkali phtocathodes: standard (lower curve) and with ion-blocking structures.

applications of fast GEM x-ray imagers include time-resolved structure research at synchrotron light sources (Orthen et al., 2004; Wagner et al., 2004).

Coupled to a high-resolution pixel readout, GEM detectors allow one to image the path of photoelectrons produced in the

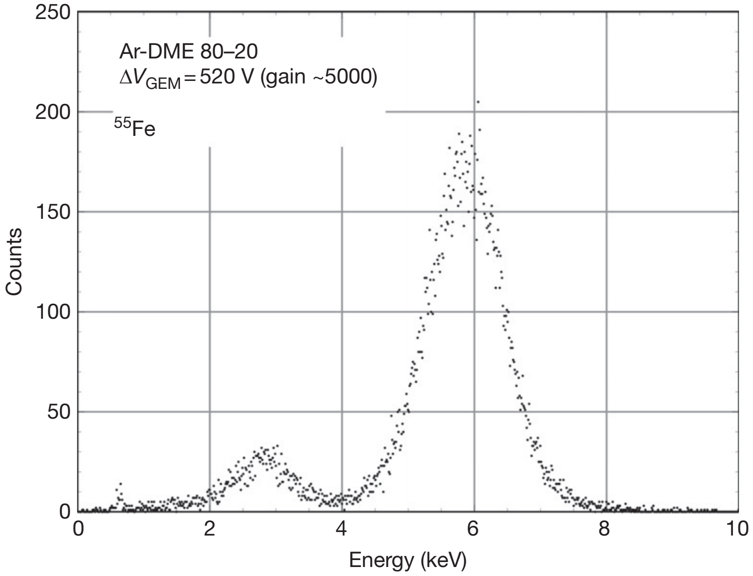

Figure 76 Single GEM pulse height spectrum for 5.9 keV x-rays.

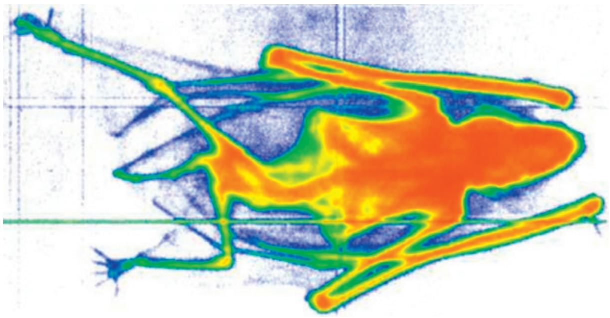

Figure 77 Soft x-ray transmission radiography of a small mammal; the image size is about 60 × 20 mm.

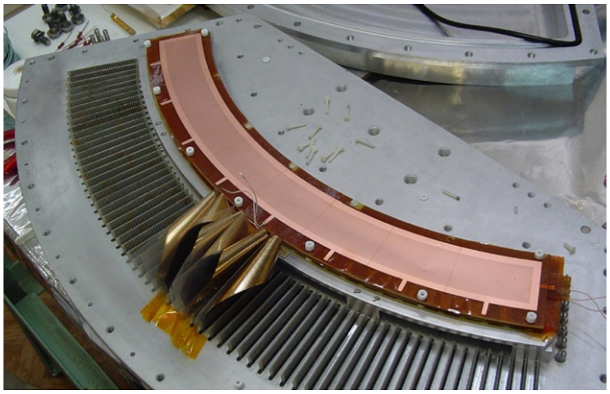

Figure 78 A TGEM wide-angle x-ray scattering detector.

gas by soft x-rays; as the photoelectron is ejected in the gas preferentially in the direction of the photon electric field, an accurate measurement of its trajectory gives information on the polarization of the source, a promising tool in astrophysics for the study of black holes and neutron stars emissions (Bellazzini et al., 2003; Costa et al., 2001). Originally making use of discrete electronics for the readout of the pixels, the x-ray polarimeter has been improved with the development of active solid-state pixel ASIC used as direct charge collecting anode and the use of GEM electrodes with small pitch and holes' size (Bellazzini et al., 2004; Black et al., 2003). **Figure 81** shows an open instrument, separated in the active and sensing parts, and **Figure 82** shows an example of photoelectron track recorded with the polarimeter (Bellazzini et al., 2007a). The detector opens up a new window in the astronomical observation of x-ray sources (Bellazzini and Muleri, 2010).

8.22.8.4 Hard x-Rays and Gamma Rays

As for all gaseous detectors, the efficiency of GEM devices decreases very steeply for photon energies above few tens of keV; xenon fillings and high pressures help, but as indicated in **Section 8.22.4**, the gains that can be achieved decrease with pressure. The use of internal converters extends the region of sensitivity, at the cost of an increased complexity of the detector. To exploit a multi-GEM geometry, the converters have to be partly transparent to electrons; the GEM electrodes themselves can be used as converters.

The gamma detection efficiency of the GEM foils can be enhanced adding a layer of high-Z metal on the electrodes. With 3 μm of gold electroplated on both sides of a standard GEM, efficiencies approaching 1% have been measures in the 100-keV energy range (**Figure 83**; Koike et al., 2011).

The high-rate capability and radiation hardness of GEM-based detectors find promising applications in portal imaging, the diagnostic tool used to monitor the treatment plans and doses during cancer therapy with hard x-ray (Iacobaeus et al., 2000). A scheme of the detector is shown in **Figure 84**. For high-energy photons, ionization released by electrons ejected in the gas from the converters by photoelectric or Compton effect drift through the multiple structure and multiply when entering a GEM electrode. For calibration purposes, an upper drift region can be added to detect soft radiation. Proper

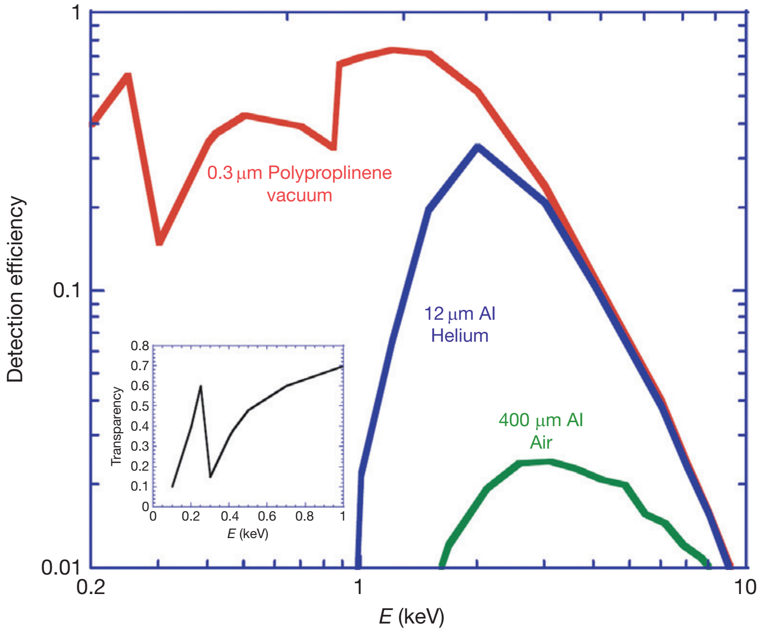

Figure 79 Detection efficiency as a function of x-ray energy of the plasma diagnostics camera for various windows and containment bags.

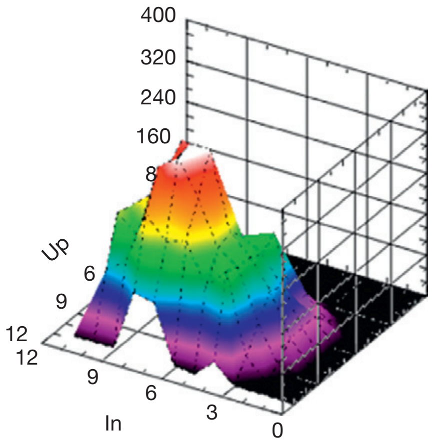

Figure 80 Time-resolved 2D x-ray emission from a plasma.

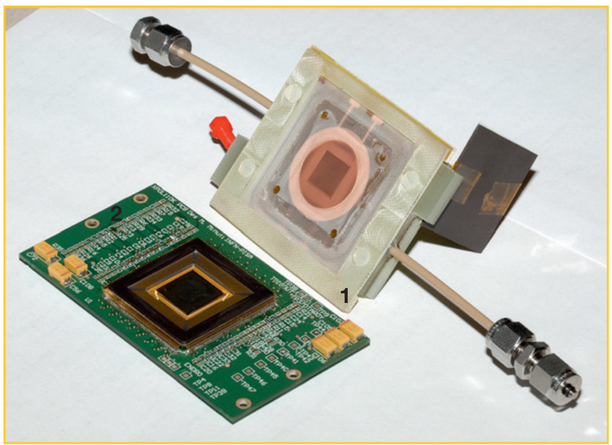

Figure 81 Open view of a GEM soft x-ray polarimeter.

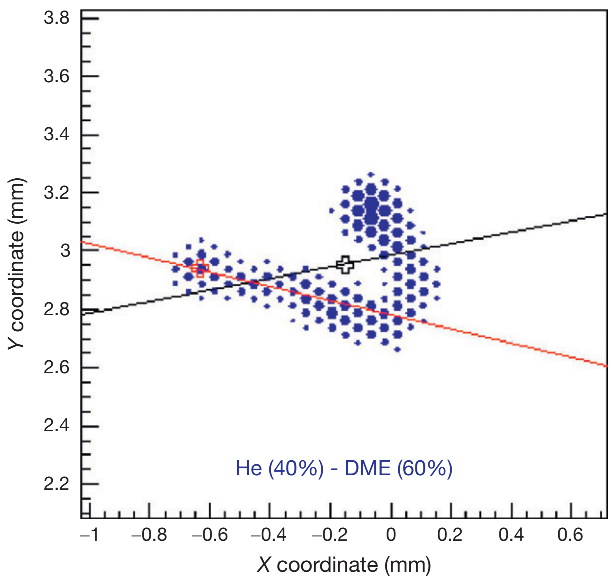

Figure 82 Photoelectron track emitted by a 5.4-keV x-ray; the hexagonal-active pixels have 50 μm pitch, and the content corresponds to the recorded charge on each pixel.

operation of the detector requires a thorough understanding and optimization of the charge gain and transfer through the layers; ideally, to avoid discharges or electronics saturation, the total collected charge for an event should not depend on the conversion depth. Detailed studies of the charge collection properties and linearity of response of the structure are given in Östling et al. (2003). Essential for this application, the readout electronics has to withstand the high stray radiation levels; the system developed for portal imaging at the Karolinska Institutet, mounted on the outer edges of the detector, has a

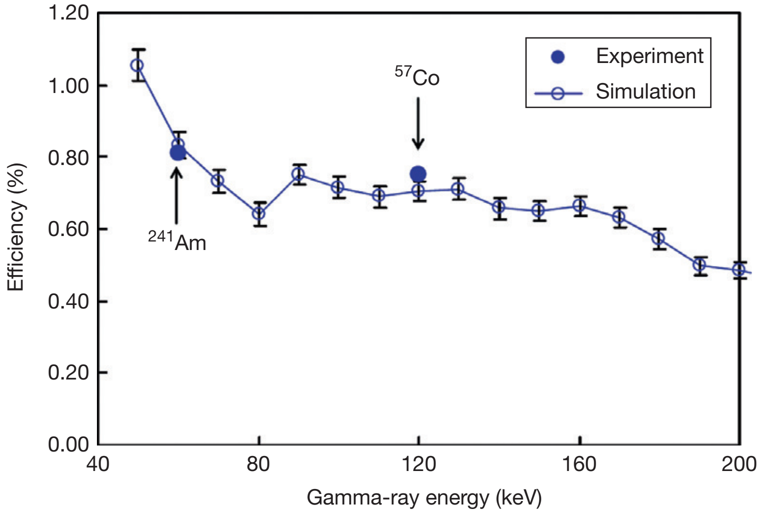

Figure 83 Computed and measured detection efficiencies of a gold-plated GEM as a function of photon energy.

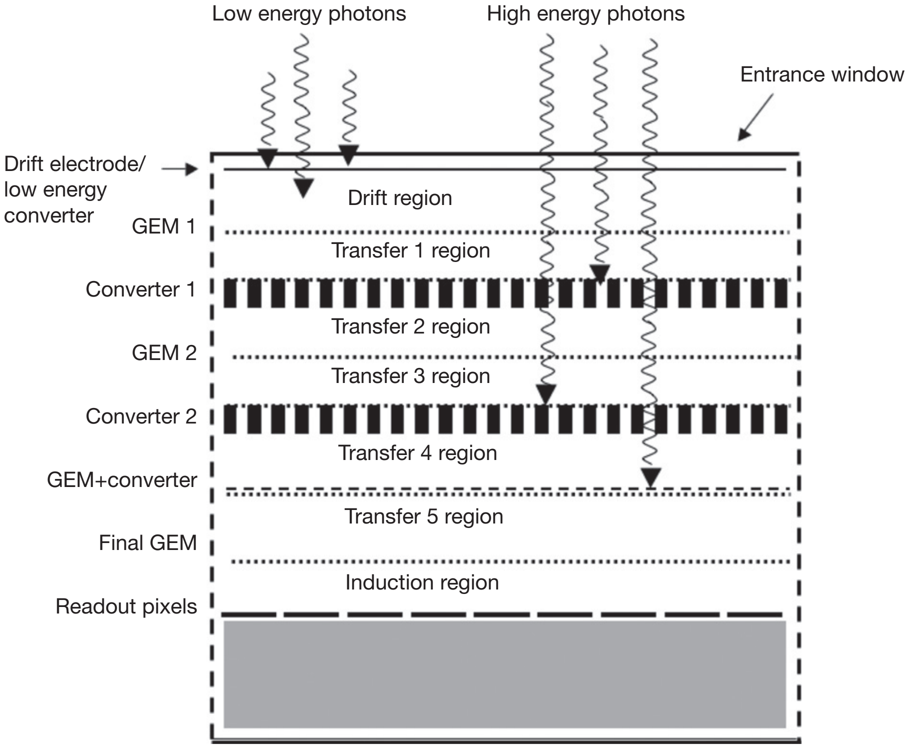

Figure 84 A multi-GEM and converters stack for detection of soft and hard x-rays.

dedicated ASIC readout of 1000 pixels in the sensitive area and has been extensively tested under continuous irradiation (Östling et al., 2004).

The time-resolved imaging properties of the device are demonstrated using an oscillating system of steel spheres (Newton pendulum); **Figure 85** shows consecutive images of the pendulum at a frame rate of 70 Hz for 40 keV x-rays (Östling, 2006). The device has evolved into a commercial instrument for portal imaging (Mitterlechner et al., 2011).

The low efficiency of an individual converter can be increased using multiple GEM structures, as described. This approach has, however, the inconvenience of resulting in a poor time resolution, due to the variable collection time; for nonparallel photon beams as in PET imaging, it suffers also from an increasing error due to parallax. A way to improve on both points is to determine the depth of the conversion in multilayer devices, detecting the signal on the electrode nearest to the conversion. The principle of the device is to

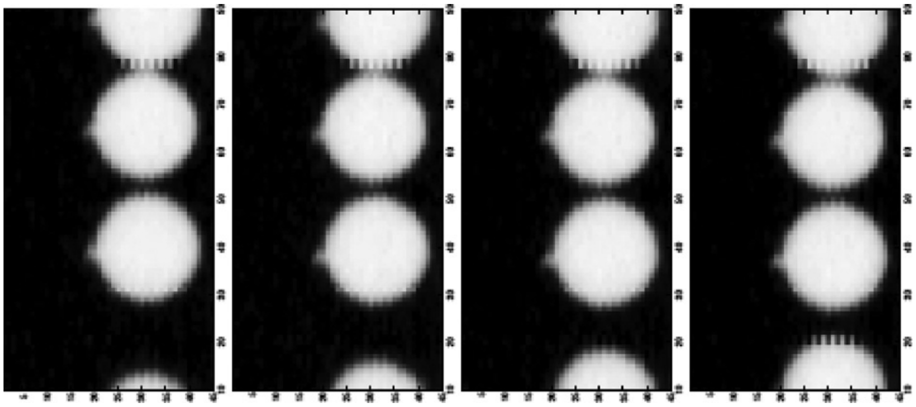

Figure 85 Seventy-Hertz time-resolved 40 keV x-ray images of a Newton pendulum.

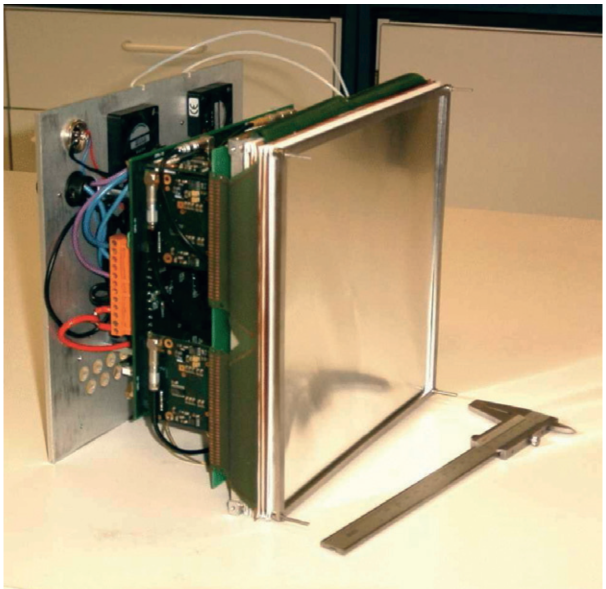

Figure 86 The CASCADE neutron detector and imager.

alternate active GEM electrodes with metallic meshes serving as both converters and controllers of electron transparency; voltages applied on each cell impart a large enough gain to permit direct detection of the charge released by the conversion, and to transfer only a fraction of the electrons to the next cell so that the effective gain is close to unity. Recording the pulses on the GEM electrode in each cell permits to determine the depth of conversion, while localization is performed on strips or pads on the last collecting electrode (Croci et al., 2007).

8.22.8.5 Detection and Imaging of Neutrons

Detection of thermal and cold neutrons in gaseous counters can be achieved exploiting the large neutron cross section of ^{3}He used as gas filling, through the reaction ${}^3_2\mathrm{He}+n \rightarrow {}^3_1\mathrm{H}+p$. This approach, however, suffers from several limitations: low efficiency, unless operated at high pressures, low-rate capability due to the slow electron drift in helium mixtures, and availability of the helium isotope itself. The use of internal converters solves the above-mentioned problems. ^{6}Li, ^{10}Be have very large neutron capture cross sections releasing heavily ionizing alpha particles; ^{157}Gd and ^{155}Gd generate a γ cascade and low energy conversion electrons that can be easily detected. Comparative performances of ^{3}He and converter-based gaseous detectors are discussed by Gebauer (2004).

CASCADE is a neutron detector and imager made with several ^{10}B-coated GEM electrodes in a stack and bidimensional projective localization. First described in a PhD work (Klein, 2000), the device has evolved in a fully operational system capable of detecting neutron fluxes at rates up to 10 MHz cm^{-2} (Klein and Schmidt, 2011). **Figure 86** shows the assembled detector with 20×20 cm^2 active area and the readout electronics. With 128 strips readout on both coordinates, the detector has a resolution of ~2.6 mm FWHM; **Figure 87** shows a cold neutron radiography of several office objects. The efficiency as a function of neutron wavelength has been measured for three and eight ^{10}B converter layers, and extrapolated to a 20-layer device (**Figure 88**).

A high-rate neutron detector with a boron converter deposited on the drift electrode and followed by a double GEM with 2D readout has been developed for beam monitoring at the Japan Proton Accelerator J-PARC (Ohshita et al., 2010, 2012).

8.22.9 Cryogenic and Dual-Phase Detectors

Motivated by perspective applications in dark matter searches and neutrino astrophysics, the operation of GEM-based detectors at cryogenic temperatures has been thoroughly investigated. In pure noble gases, the voltage dependence of gain onn a TGEM detector is only slightly affected by temperature, once the gas density is taken into account, as seen in **Figure 89** for helium, argon, and krypton (Bondar et al., 2004); owing to the avalanche confinement mechanism, discussed in **Section 8.22.4**, high gains can be attained in the pure gases.

In a cryogenic vessel with controlled temperature and pressure, the search has been extended to dual-phase systems, in which the ionization electrons released in the liquid are

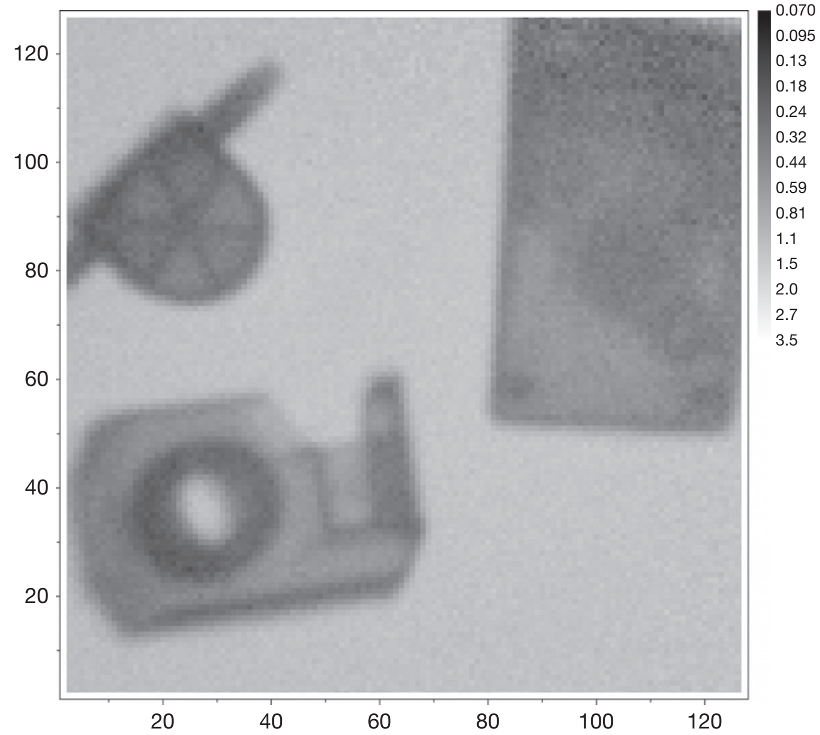

Figure 87 Neutron radiography of common office objects.

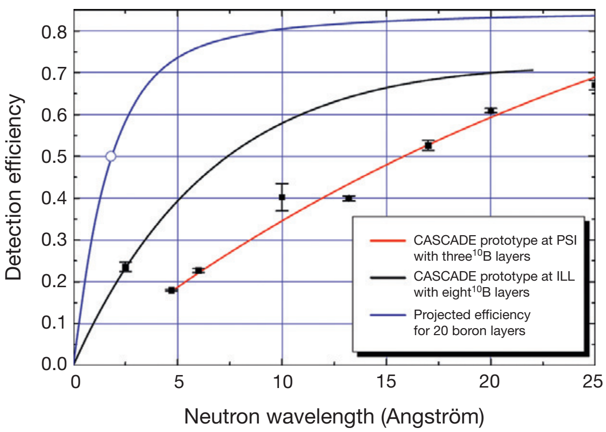

Figure 88 Neutron detection efficiency as a function of wavelength of the CASCADE prototype, measured with three and eight boron converter layers (points with error bars), and estimated for 20 layers.

extracted, multiplied, and detected within an overlaying gaseous layer. **Figure 90** (Bondar et al., 2006b) gives examples of gain measured in various gases and conditions; even in the worst case (for xenon), gains above a few hundred can be reached, sufficient to ensure detection of ionization trails deposited in the liquid. In a two-phase argon detector, gains are large enough to detect single electrons (Bondar et al., 2007).

In TPC-like detectors designed for dark matter searches, the primary scintillation in the liquid, providing the time of the event, can be detected with photomultipliers or internal photosensitive CsI layers; in both cases, the UV photon emission in the gas-phase multiplication can be very disturbing. The addition of a small percentage of methane to xenon acts as quencher in the gas phase, still with a sufficient scintillation yield in the liquid (Lightfoot et al., 2005).

A $10 \times 10\ cm^2$ active area, 21-cm drift double-phase argon TPC with an LEM in the gas phase has been successfully tested, providing stable gains around 30, sufficient to obtain good-quality images on cosmic rays (**Figures 91** and **92**; Badertscher et al., 2010, 2011). The primary scintillation in the liquid, detected by a photomultiplier, provides the trigger and time reference for the drift time measurement; an additional grid in the gas, just above the liquid surface, is used to help the extraction of electrons.

8.22.10 Light Emission and Optical Detection of Tracks

Electron–molecule collisions at high electric fields result in the creation of excited states with the consequent emission of photons. The amount and spectral distribution of the secondary photons depend on gas and applied fields, and can be copious even before the onset of charge multiplication, a process exploited in high-resolution proportional counters.

Photon emission in GEM structures with a semitransparent anode was first reported by Fraga et al. (2002). With a xenon–CO_2 gas filling, and using a high-resolution solid-state camera, 2D imaging of soft x-rays with $\sim 100\ \mu m$ resolution was demonstrated with single- and double-GEM detectors (Fraga et al., 1999).

The emission spectrum of $^3He–CF_4$ mixtures is centered around 600 nm, matching the spectral response of

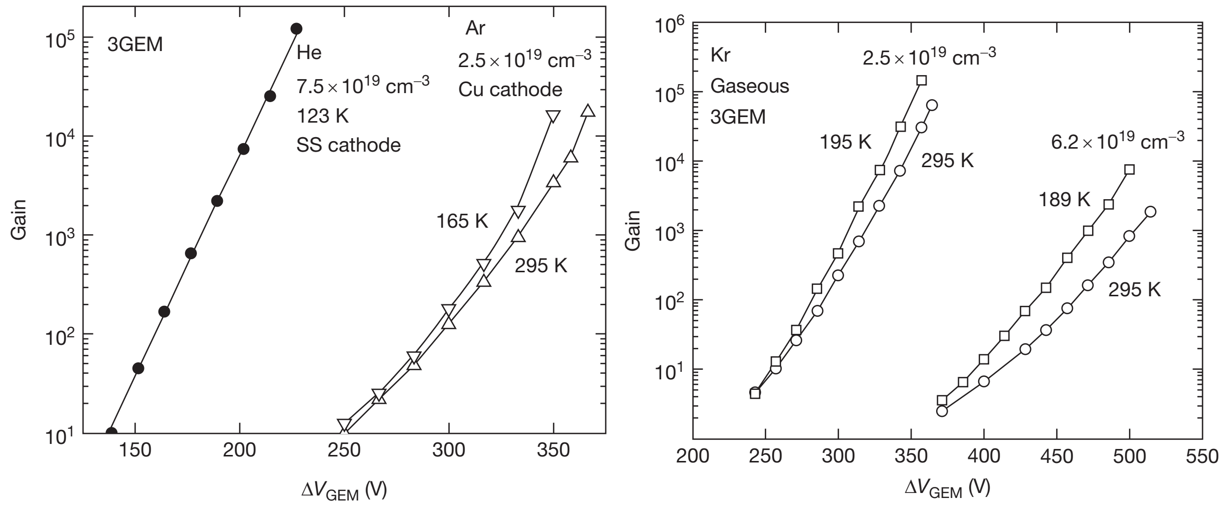

Figure 89 TGEM gain as a function of voltage in noble gases for several values of temperature. In helium, data at low and room temperature coincide.

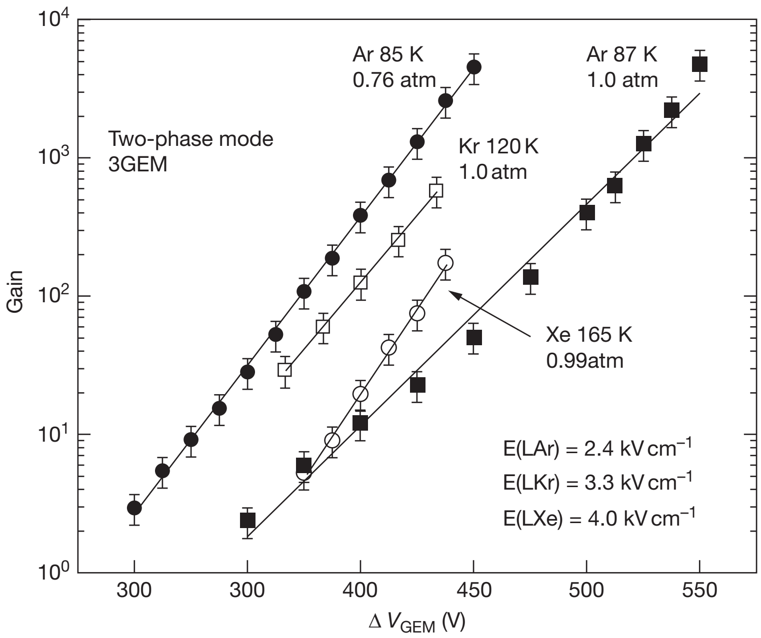

Figure 90 TGEM gain-voltage dependence for two-phase argon and xenon detectors.

commercial CCD systems. Figure 93 shows the optical recording of neutron interactions on helium-releasing proton–triton pairs, for 1 s exposure; the vertex of the interaction is clearly identified, and integration of the scintillation light provides information on the energy of tracks (Fraga et al., 2002). Systematic measurements of charge gain and light yield for He–CF_4, Ar–CF_4, Ar–TEA, Ar–TMAE, and Xe–TMAE mixtures (TEA: triethylamine $(C_2H_5)_3N$ and TMAE: tetrakis-dimethyl amino ethylene $((CH_3)_2N)_2C$ are photosensitive vapors used in Cherenkov ring imaging and copious photon emitters in the near ultraviolet and in the visible, respectively) are reported by Fraga et al. (2001, 2003). The addition of a wavelength shifter layer, deposited either on the window or directly on the GEM electrodes, extends the use of the technology to gases having most of the scintillation in the ultraviolet, as is the case for pure noble gases and their mixtures (Fraga et al., 2004).

The timing characteristics of the scintillation light have been analyzed, coupling the optical GEM devices to photomultipliers (Margato et al., 2003); simultaneous detection of the fast scintillation and of the optical images opens the way to the development of GEM-based optical readout TPC (Margato et al., 2003). To overcome the recording rate limitations of commercial CCD imagers, systems using arrays of photomultipliers or multianode PM have been developed with promising results (Fetal et al., 2007).

A gas scintillation detector using two cascaded GEMs for charge multiplication has been developed for dose monitoring

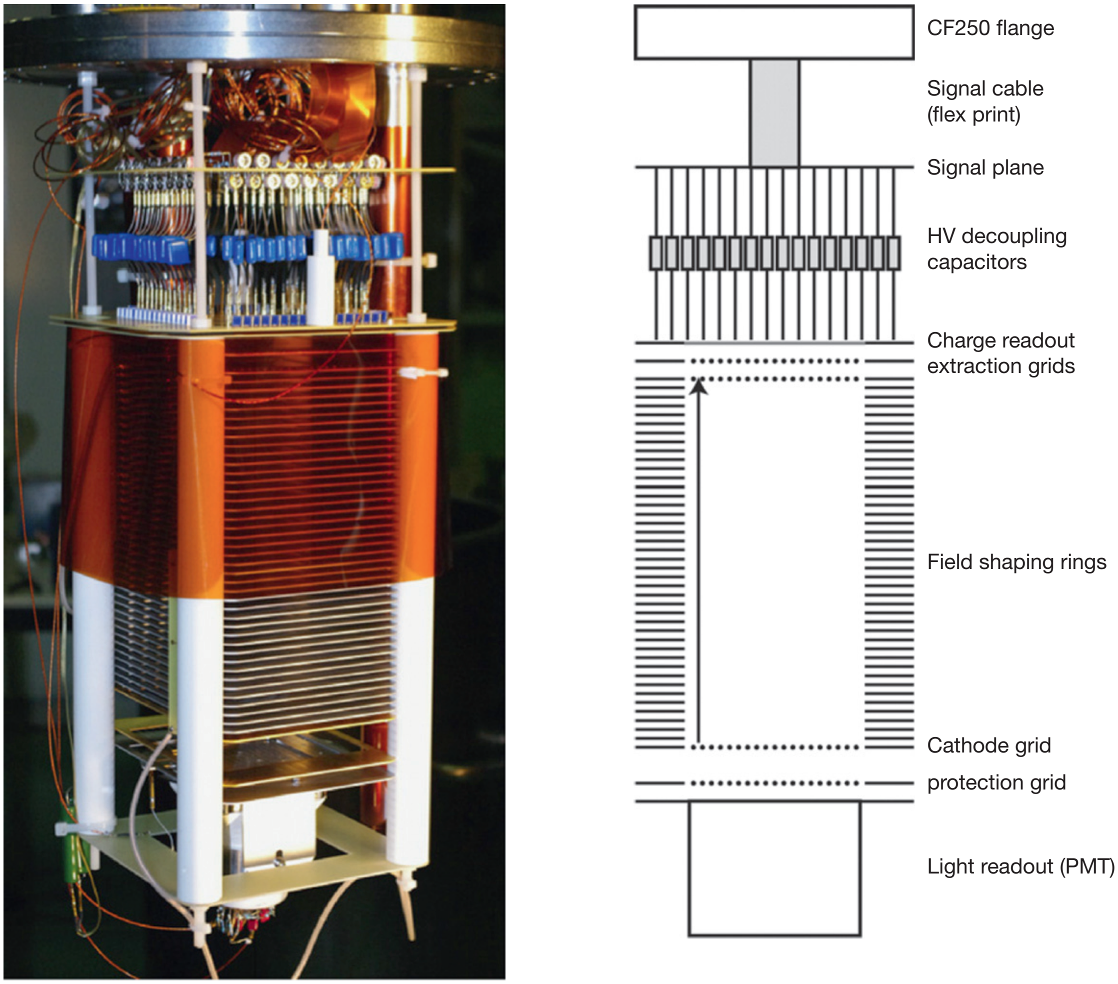

Figure 91 The dual-phase argon LEM-TPC.

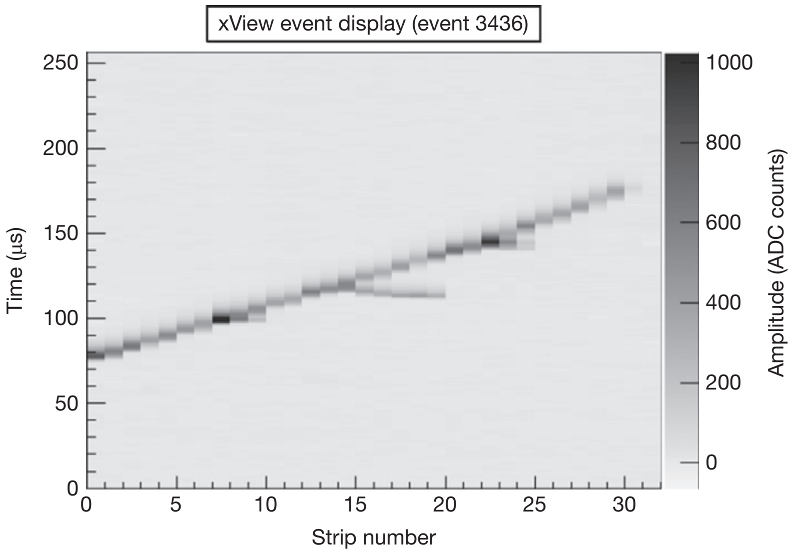

Figure 92 A cosmic-ray track detected with the LEM-TPC.

Figure 93 Proton–triton pairs produced by thermal neutrons in ^{3}He, imaged with the optical GEM.

in clinical ion beams. Since the CCD imager cannot be exposed to the beam, the image is reflected by a mirror and focused on the solid-state sensor by suitable optics; measurements show the good proportionality between the detected scintillation light and the beam intensity, and compare favorably to standard scintillation screen (Fetal et al., 2003; Klyachko et al., 2011; Seravalli et al., 2008, 2009; Timmer et al., 2002).

References

Abbon P, Albrecht E, Alexakhin VY, et al. (2007) The COMPASS experiment at CERN. *Nuclear Instruments and Methods A* 577: 455.

Agócs AG, di Mauro A, Ben David A, et al. (2008) Study of GEM-like detectors with resistive electrodes for RICH applications. *Nuclear Instruments and Methods A* 595: 128.

Aidala C, Azmoun B, Fraenkel Z, et al. (2003) A hadron-blind detector for PHENIX. *Nuclear Instruments and Methods A* 502: 200.

Akesson T, Barberio E, Bondarenko V, et al. (2002) Aging studies for the ATLAS transition radiation tracker (TRT). *Nuclear Instruments and Methods A* 515: 166.

Alexa M, Fabjan CWR, and Riegler W (2002) Limits to drift chamber performance at LHC luminosities. *Nuclear Instruments and Methods A* 478: 135.

Alexeev M, Alfonsi M, Birsa R, et al. (2010a) Development of THGEM-based photon detectors for Cherenkov imaging counters. *Journal of Instrumentation* 5: P03009.

Alexeev M, Birsa R, Bradamante F, et al. (2008) Micropattern gaseous photon detectors for Cherenkov imaging counters. *IEEE Nuclear Science Symposium Conference Record 1335*.

Alexeev M, Birsa R, Bradamante F, et al. (2010b) Micropattern gaseous photon detectors for Cherenkov imaging counters. *Nuclear Instruments and Methods A* 623: 129.

Alexeev M, Birsa R, Bradamante F, et al. (2011) Progress towards a TGEM-based detector of single photons. *Nuclear Instruments and Methods A* 639: 130.

Alfonsi M, Baccaro S, Bencivenni G, et al. (2005) Studies of etching effects on Triple-GEM detectors operated with CF4-based gas mixtures. *IEEE Transactions on Nuclear Science* NS-52: 2872.

Alfonsi M, Bencivenni G, Bonivento W, et al. (2004) High-rate particle triggering with triple-GEM detector. *Nuclear Instruments and Methods A* 518: 106.

Alfonsi M, Bencivenni G, Brock I, et al. (2010) Activity of CERN and LNF groups on large area GEM detectors. *Nuclear Instruments and Methods A* 617: 151.

Alfonsi M, Croci G, Duarte Pinto S, et al. (2012) Simulation of the dielectric charging-up effect in a GEM detector. *Nuclear Instruments and Methods A* 671: 6.

Altunbas C, Capéans M, Dehmelt K, et al. (2002) Construction, test and commissioning of the Triple-GEM tracking detector for COMPASS. *Nuclear Instruments and Methods A* 490: 177.

Altunbas C, Dehmelt K, Kappler S, et al. (2003) Aging measurements with the gas electron multiplier (GEM). *Nuclear Instruments and Methods A* 515: 249.

Amaro F, Veloso JFCA, Maia JM, et al. (2004) Noble-gas operation of micro-hole and strip plate electron multipliers at atmospheric-to-high pressures. *Nuclear Instruments and Methods A* 535: 341.

Anderson W, Azmoun B, Cherlin A, et al. (2011) Design, construction, operation and performance of a Hadron Blind Detector for the PHENIX experiment. *Nuclear Instruments and Methods A* 646: 35.

Aulchenko VM, Bukin MA, Grebenkin SS, et al. (2007) A new one-coordinate gaseous detector for WAXS experiments (OD4). *Nuclear Instruments and Methods A* 575: 251.

Aulchenko VM, Papushev PA, Sharafutinov MR, et al. (2009) Progress with one-coordinate detector for WAXS. *Nuclear Instruments and Methods A* 603: 69.

Bachmann S, Bressan A, Capeàns M, et al. (2002) Discharge studies and prevention in the gas electron multiplier. *Nuclear Instruments and Methods A* 479: 294.

Bachmann S, Bressan A, Ketzer B, et al. (2001) Performance of GEM detectors in high intensity particle beams. *Nuclear Instruments and Methods A* 470: 548.

Bachmann S, Bressan L, Ropelewski L, et al. (1999) Charge amplification and transfer processes in the gas electron multiplier. *Nuclear Instruments and Methods A* 438: 376.

Badertscher A, Curioni A, Knecht L, et al. (2011) First operation of a double phase LAr large electron multiplier time projetion chamber with a 2D projective readout anode. *Nuclear Instruments and Methods A* 641: 48.

Badertscher A, Knecht L, Laffranchi M, et al. (2010) Operation of a double-phase pure argon large electron multiplier time projection chamber: Comparison of single and double phase operation. *Nuclear Instruments and Methods A* 617: 188.

Bagaturia Y, Baruth O, Dreis HB, et al. (2002) Studies of aging and HV breakdown problems during development and operation of MSGC and GEM detectors for the inner tracking system of HERA-B. *Nuclear Instruments and Methods A* 490: 223.

Bagliesi MG, Berretti M, Brucken E, et al. (2010) The TOTEM T2 telescope based on triple-GEM chambers. *Nuclear Instruments and Methods A* 617: 134.

Balla A, Bencivenni G, Cerioni S, et al. (2011) Status of the cylindrical-GEM project for the KLOE-2 inner tracker. *Nuclear Instruments and Methods A* 628: 194.

Bamberger A, Desch K, Renz U, et al. (2007) Resolution studies on 5 GeV electron tracks observed with triple-GEM and MediPix/TimePix readout. *Nuclear Instruments and Methods A* 581: 274.

Barbeau PS, Collar J, Miyamoto J, and Shipsey I (2004) Electron transparency, ion transparency and ion feedback of a 3M GEM. *Nuclear Instruments and Methods A* 525: 33.

Barr A, Bachmann S, Boimska B, et al. (1998) Construction, test and operation in a high intensity beam of a small system of micro-strip gas chambers. *Nuclear Instruments and Methods A* 403: 31.

Bartol F, Bordessoule M, Chaplier G, et al. (1996) The C.A.T. pixel proportional gas counter detector. *Journal of Physics III France* 6: 337.

Beirle S, Werthenbach U, Zech G, and Zeuner T (1999) Carbon coated gas electron multipliers. *Nuclear Instruments and Methods A* 423: 297.

Bellazzini R, Angelini F, Baldini L, et al. (2004) Reading a GEM with a VLSI pixel ASIC used as direct charge collecting anode. *Nuclear Instruments and Methods A* 535: 477.

Bellazzini R, Baldini L, Brez A, et al. (2003) A photoelectric polarimeter based on a micropattern gas detector for x-ray astronomy. *Nuclear Instruments and Methods A* 510: 176.

Bellazzini R, Baldini L, Brez A, et al. (2007a) Gas pixel detectors. *Nuclear Instruments and Methods A* 572: 160.

Bellazzini R, Brez A, Gariano G, et al. (1998) What is the real gas gain of a standard GEM? *Nuclear Instruments and Methods A* 419: 429.

Bellazzini R and Muleri F (2010) X-ray polarimetry: A new window on the high energy sky. *Nuclear Instruments and Methods A* 623: 766.

Bellazzini R, Spandre G, Brez A, et al. (2007b) Imaging with the invisible light. *Nuclear Instruments and Methods A* 581: 246.

Bencivenni G, Bonivento W, Bosio C, et al. (2002a) A fast triple-GEM detector for high-rate charged-particle triggering. *Nuclear Instruments and Methods A* 478: 245.

Bencivenni G, Bonivento W, Cardini A, et al. (2002b) Performance of a triple-GEM detector for high rate charged particle triggering. *Nuclear Instruments and Methods A* 494: 156.

Bencivenni G and Domenici D (2007) An ultra-light cylindrical detector as inner tracker at KLOE-2. *Nuclear Instruments and Methods A* 581: 221.

Bencivenni G, Felici G, Murtas F, et al. (2002c) A triple GEM detector with pad readout for high rate charged particle triggering. *Nuclear Instruments and Methods A* 488: 493.

Benlloch J, Bressan A, Büttner C, et al. (1998a) Development of the gas electron multiplier (GEM). *IEEE Transactions on Nuclear Science* NS-45: 234.

Benlloch J, Bressan A, Capeáns M, et al. (1998b) Further developments and beam tests of the gas electron multiplier (GEM). *Nuclear Instruments and Methods A* 419: 410.

Bilevych Y, Blanco Carballo VM, Chefdeville M, et al. (2011) Spark protection layers for CMOS pixel anode chips in MPGDs. *Nuclear Instruments and Methods A* 629: 66.

Black JK, Deines-Jones P, Ready SE, and Street RA (2003) X-ray polarimeter with an active-matrix pixel proportional counter. *Nuclear Instruments and Methods A* 513: 639.

Blank B, Hay L, Huikari J, et al. (2010) A time projection chamber for the three-dimensional reconstruction of two-proton radioactivity events. *Nuclear Instruments and Methods A* 613: 65.

Bondar A, Buzulutskov A, de Oliveira R, et al. (2006a) Light multi-GEM detector for high-resolution tracking systems. *Nuclear Instruments and Methods A* 556: 495.

Bondar A, Buzulutskov A, Grbieux A, et al. (2007) A two-phase argon avalanche detector operated in a single electron counting mode. *Nuclear Instruments and Methods A* 574: 493.

Bondar A, Buzulutskov S, Grebenuk A, et al. (2006b) Two-phase argon and xenon avalanche detectors based on gas electron multiplier. *Nuclear Instruments and Methods A* 556: 273.

Bondar A, Buzulutskov A, Sauli F, and Shekhtman L (1998) High and low pressure operation of the gas electron multiplier. *Nuclear Instruments and Methods A* 419: 418.

Bondar A, Buzulutskov A, and Shekhtman L (2002a) High pressure operation of the triple-GEM detector in pure Ne, Ar and Xe. *Nuclear Instruments and Methods A* 481: 200.

Bondar A, Buzulutskov A, Shekhtman L, and Vasiljev A (2003) Study of ion feedback in multi-GEM structures. *Nuclear Instruments and Methods A* 496: 325.

Bondar A, Buzulutskov A, Shekhtman L, et al. (2002b) Triple GEM operation in compressed He and Kr. *Nuclear Instruments and Methods A* 493: 8.

Bondar A, Buzulutskov A, Shekhtman L, et al. (2004) Cryogenic avalanche detectors bases on gas electron multipliers. *Nuclear Instruments and Methods A* 524: 130.

Bonivento W, Cardini A, Bencivenni G, et al. (2002) A complete simulation of a triple-GEM detector. *IEEE Transactions on Nuclear Science* 49: 1638.

Bouclier R, Capeáns M, Garabatos C, et al. (1995) On some factors affecting the discharge conditions in micro-strip gas chambers. *Nuclear Instruments and Methods A* 365: 65.

Bouclier R, Dominik W, Hoch M, et al. (1997) New observations with the gas electron multiplier (GEM). *Nuclear Instruments and Methods A* 396: 50.

Boudjemline K, Dixit MS, Martin J-P, and Sachs K (2007) Spatial resolution of a GEM readout TPC using the charge dispersion signal. *Nuclear Instruments and Methods A* 574: 22.

Bouianov O, Bouianov M, Orava R, and Tikhonov V (2001) Foil geometry effects on GEM characteristics. *Nuclear Instruments and Methods A* 458: 698.

Bouianov O, Bouianov M, Orava R, et al. (2000) Progress in GEM simulation. *Nuclear Instruments and Methods A* 450: 227.

Breskin A, Alon R, Cortesi M, et al. (2009) A concise review of THGEM detectors. *Nuclear Instruments and Methods A* 598: 107.

Breskin A, Buzulutskov A, and Chechik R (2002a) GEM photomultiplier operation in CF4. *Nuclear Instruments and Methods A* 483: 670.

Breskin A, Buzulutskov A, Chechik R, et al. (2001) Sealed gas UV-photon detector with a multi-GEM multiplier. *IEEE Transactions on Nuclear Science* NS-48: 417.

Breskin A, Buzulutskov A, Chechik R, et al. (2002b) Sealed GEM photomultiplier with a CsI photocathode: Ion feedback and ageing. *Nuclear Instruments and Methods A* 478: 225.

Breskin A, Charpak G, Sauli F, et al. (1974) Recent observations and measurements with high-accuracy drift chambers. *Nuclear Instruments and Methods A* 124: 189.

Breskin A, Lyashenko A, Chechik R, et al. (2010) Progress in gaseous photomultipliers for the visible spectral range. *Nuclear Instruments and Methods A* 623: 318.

Bressan A, Labbé JC, Pagano P, et al. (1999a) Beam tests of the gas electron multiplier. *Nuclear Instruments and Methods A* 425: 262.

Bressan A, Ropelewski L, Sauli F, et al. (1999b) Two-dimensional readout in GEM detectors. *Nuclear Instruments and Methods A* 425: 254.

Büttner C, Capeáns M, Dominik W, et al. (1998) Progress with the gas electron multiplier. *Nuclear Instruments and Methods A* 409: 79.

Buzulutskov A, Breskin A, Chechik R, et al. (2000) The GEM photomultiplier operated with noble gas mixtures. *Nuclear Instruments and Methods A* 443: 164.

Buzulutskov A, Shekhtman L, Bressan A, et al. (1999) GEM operation in pure noble gases and the avalanche confinement. *Nuclear Instruments and Methods A* 433: 471.

Campbell M, Chefdeville M, Colas P, et al. (2005) Detection of single electrons by means of a Micromegas-covered MediPix2 pixel CMOS readout circuit. *Nuclear Instruments and Methods A* 540: 295.

Capeáns M (2003) Aging and materials: Lessons for detectors and gas systems. *Nuclear Instruments and Methods A* 515: 73.

Carnegie RK, Dixit MS, Dubeau J, et al. (2005) Resolution studies of cosmic-ray tracks in a TPC with GEM readout. *Nuclear Instruments and Methods A* 538: 372.

Charpak G, Bouclier R, Bressani T, et al. (1968) The use of multiwire proportional counters to select and localize charged particles. *Nuclear Instruments and Methods A* 62: 262–268.

Charpak G and Sauli F (1978) The multistep avalanche chamber: A new high rate, high accuracy gaseous detector. *Physics Letters* 78 B: 523–528.

Charpak G and Sauli F (1984) High-resolution electronic particle detectors. *Annual Review of Nuclear and Particle Science* 34: 285.

Chechik R, Breskin A, Garty G, et al. (1998) First results on the GEM operated at low gas pressures. *Nuclear Instruments and Methods A* 419: 423.

Chechik R, Breskin A, and Shalem C (2005) Thick GEM-like multipliers – A simple solution for large area UV-RICH detectors. *Nuclear Instruments and Methods A* 553: 35.

Chechik R, Breskin A, Shalem C, and Mörmann D (2004) Thick GEM-like hole multipliers: Properties and possible applications. *Nuclear Instruments and Methods A* 535: 303.

Cohelo LCC, Ferreira HMNBL, Lopes JAM, et al. (2007) Measurement of the photoelectron-collection efficiency in noble gases and methane. *Nuclear Instruments and Methods A* 581: 190.

Corradi G, Murtas F, and Tagnani D (2007) A novel high voltage system for a triple GEM detector. *Nuclear Instruments and Methods A* 572: 96.

Costa E, Soffitta P, Bellazzini R, et al. (2001) An efficient photoelectric X-ray polarimeter for the syudy of black holes and neutron stars. *Nature* 411: 662.

Croci G, Ropelewski L, Sauli F, and Solevi P (2007) Depth of interaction determination in GEM-based multi-layer PET deetctors. *Nuclear Instruments and Methods A* 582: 693.

Di Mauro A, Lund-Jensen B, Martinengo P, et al. (2007) Development of innovative micro-pattern gaseouus detectors with resistive electrodes and first results of their application. *Nuclear Instruments and Methods A* 581: 225.

Dixit MS, Dubeau J, and Johns PC (2004) Position sensing from charge dispersion in micro-pattern gas detectors with a resistive anode. *Nuclear Instruments and Methods A* 518: 721.

Duarte Pinto S (2009) RD51, an R&D collaboration for micropattern gaseous detectors. arXiv:0907.2673.

Duarte Pinto S, Alfonsi M, Brock I, et al. (2008) A large area GEM detector. *IEEE Nuclear Science Symposium Conference Record*. Dresden.

Fabbietti L, Angerer H, Arora R, et al. (2011) The PANDA GEM-based TPC prototype. *Nuclear Instruments and Methods A* 628: 204.

Fenker H, Baillie N, Bradshaw P, et al. (2008) BoNus: Development and use of a radial TPC using cylindrical GEMs. *Nuclear Instruments and Methods A* 592: 273.

Fetal STG, Fraga FAF, Margato LMS, et al. (2007) Towards a PMT based optical readout GEM TPC-first results. *Nuclear Instruments and Methods A* 581: 202.

Fetal S, van Eijk CWE, Fraga F, et al. (2003) Dose imaging in radiotherapy with an Ar–CF_4 filled scintillating GEM. *Nuclear Instruments and Methods A* 513: 42.

Fraenkel Z, Kozlov A, Naglis M, et al. (2005) A hadron blind detector for the PHENIX experiment at RHIC. *Nuclear Instruments and Methods A* 546: 466.

Fraga FAF, Fetal STG, Fraga MMFR, et al. (2004) The scintillation of GEMs coated with wavelength shifters. *Nuclear Instruments and Methods A* 525: 57.

Fraga FAF, Fetal STG, Margato LMS, et al. (1999) Imaging detectors based on the gas electron multiplier scintillation light. *IEEE Nuclear Science Symposium Conference Record* 2: 829.

Fraga FAF, Fetal STG, Marques RF, and Policarpo AJPL (2000) Quality control of GEM detectors using scintillation techniques. *Nuclear Instruments and Methods A* 422: 417.

Fraga MMFR, Fraga FAF, Fetal STG, et al. (2003) The GEM scintillation in He–CF_4, Ar–CF_4, Ar–TEA and Xe–TEA mixtures. *Nuclear Instruments and Methods A* 504: 88.

Fraga FAF, Margato LMS, Fetal STG, et al. (2001) Performance of a tracking device based on the GEM scintillation. *IEEE Transactions on Nuclear Science* 49: 281.

Fraga FAF, Margato LMS, Fetal STG, et al. (2002) CCD readout of GEM-based neutron detectors. *Nuclear Instruments and Methods A* 478: 357.

French MJ, Jones LL, Morrissey Q, et al. (2001) Design and results from the APV25, a deep sub-micron CMOS front-end chip for the CMS tracker. *Nuclear Instruments and Methods A* 466: 359.

Gebauer B (2004) Towards detectors for next generation spallation neutron sources. *Nuclear Instruments and Methods A* 535: 65.

Giomataris I, Rebourgeaud P, Robert JP, and Charpak G (1996) Micromegas: A high-granularity, position-sensitive gaseous detector for high particle flux environments. *Nuclear Instruments and Methods A* 376: 29–35.

Guedes G, Breskin A, Chechik R, and Mörmann D (2002) Effects of the induction-gap parameters on the signal in a double-GEM detector. *Nuclear Instruments and Methods A* 497: 305.

Guirl L, Kane S, May J, et al. (2002) An aging study of triple GEMs in Ar–CO_2. *Nuclear Instruments and Methods A* 478: 263.

Hohlmann M, Padilla C, Tesch N, and Titov M (2002) Aging phenomena in gaseous detectors-perspectives from the 2001 workshop. *Nuclear Instruments and Methods A* 494: 179.

Iacobaeus C, Brahme A, Danielsson M, et al. (2000) A novel portal imaging device for advanced radiation therapy. *IEEE Transactions on Nuclear Science* NS-48: 1496.

Inuzuka M, Hamagaki H, Ozawa K, et al. (2004) Gas electron multiplier produced with the plasma etching method. *Nuclear Instruments and Methods A* 525: 529.

Janssen ME, Ball M, Behnke T, et al. (2006) R&D studies ongoing at DESY on a time projection chamber for a detector at the international linear collider. *Nuclear Instruments and Methods A* 566: 75.

Kalliokoski M, Hilden T, Garcia F, et al. (2012) Optical scanning system for quality control of GEM foils. *Nuclear Instruments and Methods A* 664: 223.

Kaminski J, Kappler S, Ledermann B, et al. (2006) GEM TPC anode pad shape studies. *TPC Application Workshop*, Berkeley CA, USA.

Kappler S, Kaminski J, Ledermann B, et al. (2004) Design and construction of a GEM-TPC prototype for R&D purposes. *IEEE Transactions on Nuclear Science* NS-51: 1524.

Karlen D, Poffenberger P, and Rosembaum G (2005) TPC performance in magnetic fields with GEM readout. *Nuclear Instruments and Methods A* 555: 80.

Ketzer B, Altunbas C, Dehmelt K, et al. (2002) Triple GEM tracking detectors for COMPASS. *IEEE Transactions on Nuclear Science* 49: 2403.

Ketzer B, Weitzel Q, Paul S, et al. (2004) Performance of triple GEM tracking detectors in the COMPASS experiment. *Nuclear Instruments and Methods A* 535: 314.

Killenberg M, Lotze S, Mnich J, et al. (2004) Charge transfer and charge broadening of GEM structures in high magnetic fields. *Nuclear Instruments and Methods A* 530: 251.

Klein M (2000) *Experimente zur Quantenmechanik mit ultrakalten Neutronen und Entwicklung eines neuen Detektors*. Thesis, Heidelberg University.

Klein M and Schmidt CJ (2011) CASCADE, neutron detectors for highest count rates in combination with ASIC/FPGA based readout electronics. *Nuclear Instruments and Methods A* 628: 9.

Klyachko AV, Friesel DL, Kline C, et al. (2011) Dose imaging detectors for radiotherapy based on gas electron multipliers. *Nuclear Instruments and Methods A* 628: 434.

Kobayashi M, Yonamine R, Tomioka T, et al. (2011) Cosmic ray test of a GEM-based TPC prototype operated in Ar–CF_4–isobutane gas mixtures. *Nuclear Instruments and Methods A* 641: 37.

Koike T, Uno S, Uchida T, et al. (2011) A new gamma-ray detector with gold-plated gas electron multiplier. *Nuclear Instruments and Methods A* 648: 180.

Krämer M, Angerer H, Austregesilo A, et al. (2008) First results of the PixelGEM central tracking system for COMPASS. *IEEE Nuclear Science Symposium Conference Record* 2920.

Lami S, Latino G, Olivieri E, et al. (2006) A triple-GEM telescope for the TOTEM experiment. arXiv:physics/0611178v1.

Ledermann B, Kaminski J, Kappler S, and Müller T (2007) Development studies for the ILC: Measurements and simulations for a time projection chamber with GEM technology. *Nuclear Instruments and Methods A* 581: 232.

Li M, Dixit M, Dubeau J, and Johns PJ (2001) Photon-counting digital radiography using high-pressure xenon filled detectors. *Nuclear Instruments and Methods A* 471: 215.

Lightfoot PK, Hollingworth R, Spooner NJC, and Tovey T (2005) Developmet of a double-phase Xenon cell using micromegas charge readout for applications in dark matter physics. *Nuclear Instruments and Methods A* 554: 266.

Llopart X, Ballabriga R, Campbell M, et al. (2007) Timepix, a 65k programmable pixel readout chip for arrival time, energy and/or photon counting measurements. *Nuclear Instruments and Methods A* 581: 485.

Loeb LB (1961) *Basic Processes of Gaseous Electronics*. Berkeley: University of California Press.

Lyashenko A, Breskin A, Chechik R, et al. (2009) Efficient ion blocking gaseous detectors and its applications to gas-avalanche photomultipliers sensitive in the visible-light range. *Nuclear Instruments and Methods A* 598: 116.

Maia JM, Mörmann D, Breskin A, et al. (2004) Avalanche-ion back-flow reduction in gaseous electron multipliers based on GEM/MHSP. *Nuclear Instruments and Methods A* 523: 334.

Maia JM, Veloso JFCA, dos Santos JMF, et al. (2003) Advances in the micro-hole & strip plate gaseous detector. *Nuclear Instruments and Methods A A* 504: 364.

Margato LMS, Fraga FAF, Fetal STG, et al. (2003) Time analysis of the light pulses on gaseous active scintillators using GEMs with He/CF4. *Nuclear Instruments and Methods A* 504: 374.

Martinengo P, Nappi E, de Oliveira R, et al. (2009) A new generation of GEM detectors and their applications. *Nuclear Instruments and Methods A* 604: 8.

Martinengo P, Peskov V, Breskin A, et al. (2011) R&D results on a CsI-coated triple thick GEM-based photodetector. *Nuclear Instruments and Methods A* 639: 126.

McCarty R, Adams M, Brown C, et al. (1986) Identification of large transverse momentum hadrons using a Ring-Imaging Cherenkov Counter. *Nuclear Instruments and Methods A* 248: 69.

Meinschad T, Ropelewski L, and Sauli F (2004) GEM-based photon detector for RICH applications. *Nuclear Instruments and Methods A* 535: 324.

Mir JA, Stephenson R, Rhodes NJ, et al. (2007) Further studies on the gain properties of a gas electron multiplier with a micro-induction gap amplifying structure (GEM-MIGAS) aimed at low-energy X-ray detection. *Nuclear Instruments and Methods A* 580: 1372.

Mitterlechner B, Huber S, Mooslechner M, et al. (2011) Gas electron multiplier (GEM) detector-a novel radiotherapy imaging device: GEM versus amorphous silicon panels. *Radiotherapy and Onchology* 99: S361.

Mörmann D, Breskin A, Chechik R, and Shalem C (2004) Operation principles and properties of the multi-GEM gaseous photomultipliers with reflective photocathode. *Nuclear Instruments and Methods A* 530: 258.

Noschis E, Anelli G, Cervelli G, et al. (2007) Protection circuit for the T2 readout electronics of the TOTEM experiment. *Nuclear Instruments and Methods A* 572: 378.

Oda SX, Hamagaki H, Ozawa K, et al. (2006) Development of a time projection chamber using gas electron multipliers (GEM–TPC). *Nuclear Instruments and Methods A* 566: 312.

Oed A (1988) Position-sensitive detector with micro-strip anode for electron multiplication with gases. *Nuclear Instruments and Methods A* 263: 351.

Ohshita H, Otomo T, Uno S, et al. (2012) Stability of neutron beam monitor for high intensity total diffractometer at J-PARC. *Nuclear Instruments and Methods A* 672: 75.

Ohshita H, Uno S, Otomo T, et al. (2010) Development of a neutron detector wth a GEM. *Nuclear Instruments and Methods A* 623: 126.

Openshaw R, Henderson R, Faszer W, and Salomon M (1991) Etching of anode wire deposits with CF4/isobutane (80:20) avalanches. *Nuclear Instruments and Methods A* 307: 298.

Orthen A, Wagner H, Besch HJ, et al. (2003) Gas gain and signal length measurements with a triple-GEM at different pressures of Ar-, Kr- and Xe-based gas mixtures. *Nuclear Instruments and Methods A* 512: 476.

Orthen A, Wagner H, Martoiu S, et al. (2004) Development of a two-dimensional virtual pixel X-ray imaging detector for time-resolved structure research. *Journal of Synchrotron Radiation* 59: 177.

Östling J (2006) *New Efficient Detector for Radiation Therapy Imaging using Gas Electron Multipliers*. Stokholm: Thesis at Karolinska Institutet.

Östling J, Brahme A, Danielsson M, et al. (2003) Study of hole-type gas multiplication structures for portal imaging and other high counting rate applications. *IEEE Transactions on Nuclear Science* NS-50: 809.

Östling J, Brahme A, Danielsson M, et al. (2004) A radiation-tolerant electronic readout system for portal imaging. *Nuclear Instruments and Methods A* 525: 308.

Pacella D, Bellazzini R, Brez A, et al. (2003) X-VUV spectroscopic imaging with a micropatern gas detector. *Nuclear Instruments and Methods A* 508: 414.

Pacella D, Pizzicaroli G, Gabellieri L, et al. (2001) Ultrafast soft X ray 2D plasma imaging system based on gas electron multiplier detector with pixel read-out. *The Review of Scientific Instruments* 72: 1372.

Periale L, Peskov V, Carlson P, et al. (2002) Detection of the primary scintillation light from dense Ar, Kr and Xe with novel photosensitive gaseous detectors. *Nuclear Instruments and Methods A* 478: 377.

Peskov V, Bencze G, Di Mauro A, et al. (2012a) First observation of Cherenkov rings with a large area CsI-TGEM-based RICH prototype. *Nuclear Instruments and Methods A*. 695: 154.

Peskov V, Fonte P, Martinengo P, et al. (2012b) Advances in the development of micropattern gaseous detectors with resistive electrodes. *Nuclear Instruments and Methods A* 661: S153.

Poli Lener M, Corradi C, Curceneau C, et al. (2010) Performances of a GEM-based TPC prototype for new high-rate particle experiments. *Nuclear Instruments and Methods A* 617: 183.

Procureur S, Aune S, Ball J, et al. (2011) Discharge studies in micromegas detectors in a 150 GeV/c pion beam. *Nuclear Instruments and Methods A* 659: 91.

Rice-Evans P (1974) *Spark, Streamer, Proportional and Drift Chambers*. London: Richelieu.
Richter C, Breskin A, Chechik R, et al. (2000) Absolute electron transfer efficiency of GEM. *Nuclear Instruments and Methods A* 461: 38.
Richter C, Breskin A, Chechik R, et al. (2002) On the efficient electron transfer through GEM. *Nuclear Instruments and Methods A* 478: 538.
Rutherford E and Geiger H (1908) An electrical method of counting the number of α-particles from radio-active substances. *Proceedings of the Royal Society A* 81: 141.
Sauli F (1997) GEM: A new concept for electron amplification in gas detectors. *Nuclear Instruments and Methods A* 386: 531.
Sauli F (1998) Development of high rate MSGCs: Overview of results from RD-28. *Nuclear Physics* 61B: 236.
Sauli F (2001) Gas detectors: Achievements and trends. *Nuclear Instruments and Methods A* 461: 47.
Sauli F, Ropelewski L, and Everaerts P (2006) Ion feedback suppression in time projection chambers. *Nuclear Instruments and Methods A* 560: 269.
Sauli F and Sharma A (1999) Micro-pattern gaseous detectors. *Annual Review of Nuclear and Particle Science* 49: 341.
Schade P and Kaminski J (2011) A large TPC prototype for a linear collider detector. *Nuclear Instruments and Methods A* 628: 128.
Seravalli E, de Boer M, Geurink F, et al. (2008) A scintillating gas detector for 2D dose measurements in clinical carbon beams. *Physics in Medicine and Biology* 53: 4651.
Seravalli E, de Boer MR, Geurink F, et al. (2009) 2D dosimetry in a proton beam with a scintillating GEM detector. *Physics in Medicine and Biology* 54: 3755.
Sharma A (2000) 3D simulation of charge transfer in a gas electron multiplier (GEM) and comparison to experiment. *Nuclear Instruments and Methods A* 454: 267.
Sharma A (2012) Muon tracking and triggering with gaseous detectors and some applications. *Nuclear Instruments and Methods A* 666: 98.
Simon F, Azmoun B, Becker U, et al. (2007) Development of tracking detectors with industrially produced GEM foils. *IEEE Transactions on Nuclear Science* 54: 2646.
Simon F, Kelsey J, Kohl M, et al. (2009) Beam performance of tracking detectors with industrially produced GEM foils. *Nuclear Instruments and Methods A* 598: 432.
Surrow B, Burns L, Simon F, et al. (2007) Developmet of tracking detectors with industrially produced GEM foils. *Nuclear Instruments and Methods A* 572: 201.
Tamagawa T, Hayato A, Asami F, et al. (2009) Development of thick-foil and fine-pitch GEMs with a laser etching technique. *Nuclear Instruments and Methods A* 608: 390.
Tamagawa T, Tsunoda N, Hayato A, et al. (2006) Development of gas electron multiplier foils with a laser etching technique. *Nuclear Instruments and Methods A* 560: 418.
Tikhonov V and Veenhof R (2002) GEM simulation methods development. *Nuclear Instruments and Methods A* 478: 452.
Timmer JH, van Vuure TL, Bom V, et al. (2002) A scintillating GEM for 2-D dosimetry in radiation therapy. *Nuclear Instruments and Methods A* 478: 98.
Titov M (2007) New developments and future perspectives of gaseous detectors. *Nuclear Instruments and Methods A* 581: 25.
Tokanay F, Sumiyoshi T, Sugiyama H, et al. (2011) Sealed gaseous photomultpliers with CsI photocathode. *Nuclear Instruments and Methods A* 628: 190.
van der Graaf H (2009) New developments in gaseous tracking detectors. *Nuclear Instruments and Methods A* 607: 78.
van der Graaf H, Aarts AA, Chefdeville M, and van der Putten S (2006) Recent GridPix results: An integrated micromegas grid and an ageing test of a micromegas chamber. *Nuclear Instruments and Methods A* 566: 62.
van Vuure TL, van Eijk CWE, Fraga F, and Hollander RW (2001) High presure GEM operation aiming at thermal neutron detection. *IEEE Transactions on Nuclear Science* NS-48: 1092.
Va'vra J, Manzin G, McCulloch M, et al. (1999) Fast drift CRID with GEM. *Nuclear Instruments and Methods A* 433: 527.
Va'vra J and Sharma A (2002) Single electron detection in quadruple-GEM detector with pad readout. *Nuclear Instruments and Methods A* 478: 235.
Veenhof R (1998) GARFIELD, recent developments. *Nuclear Instruments and Methods A* 419: 726.
Veloso JFCA, Santos CA, Pereira F, et al. (2011) THCOBRA: Ion back flow reduction in patterned THGEM cascades. *Nuclear Instruments and Methods A* 639: 134.
Villa M, Duarte Pinto S, Alfonsi M, et al. (2011) Progress on large area GEMs. *Nuclear Instruments and Methods A* 628: 182.
Wagner H, Orthen A, Besch HJ, et al. (2004) On image reconstruction with the two-dimensional interpolating resistive readout structure of the virtual-pixel detector. *Nuclear Instruments and Methods A* 523: 287.
Walenta AH (1981) Performance and development of dE/dx counters. *Physica Scripta* 23: 354.
Walz C (2010) *Optimization and Characterization of Gas Electron Multipliers*. Thesis, Hochschule Offenburg.
Yu B, De Geronimo G, Fried J, et al. (2005) A GEM based TPC for the LEGS experiment. *IEEE Nuclear Science Symposium Conference Record 924*.
Yu B, Radeka V, Smith GC, et al. (2003) Study of GEM Characteristics for Applications in a Micro TPC. *IEEE Transactions on Nuclear Science* NS-50: 836.
Zeuner T (2000) The MSGC-GEM inner tracker for HERA-B. *Nuclear Instruments and Methods A* 446: 324.
Ziegler M (2002) *Development of a Triple GEM Detector for the LHCb Experiment*. Thesis, University of Zürich.
Ziegler M, Sievers P, and Straumann U (2000) A triple GEM detector with two dimensional readout. *Nuclear Instruments and Methods A* 471: 260.

Relevant Websites

http://gdd.web.cern.ch – Detectors.
http://fabio.home.cern.ch – Personal.
http://project-aqua.web.cern.ch – Projects.